

# Towards quantitative brain connectomics: microstructure informed tractography via convex optimization

**Thèse N° 7397**

Présentée le 22 novembre 2019

à la Faculté des sciences et techniques de l'ingénieur  
Laboratoire de traitement des signaux 5  
Programme doctoral en génie électrique

pour l'obtention du grade de Docteur ès Sciences

par

**Muhamed BARAKOVIC**

Acceptée sur proposition du jury

Dr J.-M. Vesin, président du jury  
Prof. J.-Ph. Thiran, Prof. A. Daducci, directeurs de thèse  
Prof. D. K. Jones, rapporteur  
Prof. M. Descoteaux, rapporteur  
Dr M. G. Preti, rapporteuse

2019



Dedicated to the memory of my father...



# Acknowledgements

My Ph.D. thesis has been a collaborative effort, and I want to thank all the people that have contributed to this work.

Firstly, I would like to thank my supervisor, Prof. Jean-Philippe Thiran, for allowing me to be part of the LTS5 group. Thank you for your guidance and support through each stage of the thesis. Thanks for all the freedom you always guaranteed me to follow my ideas and take my own decisions.

Secondly, I would like to thank my co-supervisor, Prof. Alessandro Daducci, for having believed in me from the beginning of my thesis and for having always proposed exciting scientific projects.

Then, I would like to thank rest of my jury member: the president of the jury Dr. Jean-Marc Vesin, the external experts, Prof. Derek K. Jones and Prof. Maxime Descoteaux, and the internal expert Dr. Maria Giulia Preti.

A special thanks go to my supervisor during my two internships in Cardiff University and Stanford University, (re-call) Prof. Derek K. Jones and Prof. Jennifer McNab. Thanks for allowing me to be part of your research groups, presenting me new collaborators, proposing new exciting ideas to explore, suggesting further research topics and especially helping in writing our publications.

Thanks to Prof. Giorgio M. Innocenti, (re-call) Prof. Maxime Descoteaux, Dr. Gabriel Girard, Dr. Erick Jorge Canales-Rodriguez, Dr. Chantal Tax and Dr. Christoph Leuze, the senior core team which supported my work during this last 4 years. They all contributed significantly to this thesis and to improvements of my skills as a research. Nevertheless, they are the people that made possible the achievement of the excellent results which you will find in this thesis.

An immense thanks go inevitably to all the LTS5 members, starting with David Romascano, who began his study and ended his experience in the lab, approximately in the same period. We have shared all different kind of moments, from very difficult to very funny, it has been 45 extremely highly enjoyable academic years of my life, and I am glad to have spent most of my research time discussing with you. Then, I re-call Gab, since he was part of the senior people that contributed to this thesis, but he is also a perfect friend that sees only the positive part of the story and fundamental in showing me how to handle difficult situations. Next, Jonathan Rafael Patino Lopez. We are born on the same day, differently from me, he is a complicated

## Acknowledgements

---

guy. When we try to collaborate together, 95% of the times we are not able to agree on almost anything. However, if you end up in that 5%, you go from forming the ideas and perform the experiments to writing the manuscript and submit, in less then one week. Another person that changed a bit my perspective of life is Thomas Yu; thanks for being positive all the time and coming and asking all kind of questions and proposing suggestions; you are a great person, and good friend and I really hope you will reach all your life goals. Thanks also to Baran Gozcu, who supported me in awkward moments. It is easy to describe Baran, he is the guy that is ready to help in any moments/situations/problems/times. Thanks also to Marco, Gaetan, Mariam, Francesco for the enjoyable time spent together. Thanks to all my other colleagues in Lausanne: Ileana, Lester, Elda, Merixtell, Adrien, Seyed, Dimitris, Saeed, Saleh, Christophe, Mattia, Helena; my colleagues during my first two years of Ph.D. which left Lausanne a couple of years ago: Pietro, Matteo F, Alia, Alessandra, Anna, Rafael, Murat, Anil, Marina, Vijay, Christoph E., Didrik, Sasan, Sybille, Damien, Christoph P, Gabriel C., Tom, Ricardo; the LTS5 secretaries: Anne and Rosie; thanks to my colleagues in Verona: Simona, Mario, Matteo; my colleagues in Cardiff: Umesh, Sila, Emre, Maxime, Giovanni, Valentina; and my colleagues in Stanford: Valentina, Marco, Supriya, Daniel and Gustavo.

And last but not least, I am deeply thankful to my family and all the people that constantly support me life's decisions. The biggest thank go to my lovely wife Aida. Thank you for you everyday love, for pushing me and proving me nothing is impossible, for making me a good person, for sharing your life and moments with me. An infinite thanks to you. A special thanks to my parents-in-law for the support and for showing me the essential things in life. Sincere thanks to my mother and my sisters, for being patient with me even when I decided to leave the country. Thanks to Ekrem, a cousin which is not anymore with us, a person that helped me in hundreds of situations, one of the few people which believed in my view of life more than anyone else. Thank you very much. And a final special thanks goes to my father, to whom this thesis is dedicated; you knew me more than anyone else, you believed in me more than anyone else, you may be the person that wanted me to see the end of my Ph.D. thesis more than anyone else, even if you knew that I will make it. Dedicate this thesis to your memory is the minimum that I can do. You are with us, you are in my heart.

*Lausanne, 30 September 2019*

M. B.

# Abstract

Tractography is the only non-invasive technique which is used to reconstruct the white matter structural connectivity of the human brain. It relies on a specific Magnetic Resonance Imaging (MRI) acquisition, called diffusion MRI, which is sensitive to the displacement of water protons to varying magnetic fields, generating a signal that can be used to indirectly estimate microscopic tissue characteristics, e.g., composition and geometry. More specifically, tractography relies on two essential aspects: 1) orientations which indicates the direction of the white matter fibers in a typical 3D grid, and 2) principles of how to connect the voxels to reconstruct the white matter connections. Tractography is a relatively young technique since it was proposed only twenty years ago; however, it is already used in specific clinical applications, e.g., partially in neurosurgery, and in research studies that involve reconstructions of well-known neuronal pathways.

Hundreds of different tractography techniques have been proposed in the past years. In order to evaluate their performance, we participated in several international challenges. The outcomes of the challenges showed the advantages and limitations of modern tractography methods. In particular, one issue that was highlighted is the lack of a gold standard. Diffusion MRI tractography typically is validated with postmortem material and a tedious concatenation of classical 2D histological slices. In this thesis, we propose one of the first studies that use a novel 3D histological technique, named CLARITY, to validate fiber orientation in a large portion of tissue.

At the typical spatial resolution of MRI, approximately 60-90% of voxels in the white matter contain multiple fiber populations. However, most of the microstructure imaging techniques proposed are not suitable to disentangle multiple populations in a voxel. In this thesis, we aimed to study the limitations of modern tractography approaches, and we proposed novel methods where tractography could play a crucial role. We propose to use microstructure informed tractography to regularize two important microstructural features, i.e., axon diameter and transversal relaxation time  $T_2$ , showing the clear advantages of the use of global approaches and opening a new perspective for connectivity analysis. However, the price to pay for increasing the complexity of existing models is an increase in computational burden. In the appendix of the thesis, we propose a preliminary study which uses neural network approaches to accelerate global fitting of complex models.

*Keywords: diffusion MRI, tractography, CONNECTOM scanner, microstructure informed tractography, CLARITY, tissue clearing, axon diameter,  $T_2$ , neural network*





# Riassunto

La trattografia è l'unica tecnica non invasiva utilizzata per ricostruire la connettività strutturale della materia bianca del cervello umano. Si basa su una specifica tecnica diagnostica per immagini chiamata risonanza magnetica (MRI) a diffusione, che è sensibile allo spostamento di protoni d'acqua a campi magnetici, generando un segnale che può essere utilizzato per stimare indirettamente le caratteristiche microscopiche del tessuto, come ad esempio la composizione e la geometria. In particolare, la trattografia si basa su due aspetti essenziali: 1) orientazioni che indicano la direzione delle fibre di materia bianca, in una tipica griglia 3D, e 2) principi di come collegare i voxel per ricostruire le connessioni della materia bianca. La trattografia è una tecnica relativamente giovane poiché è stata proposta solo vent'anni fa; tuttavia, è già utilizzata in applicazioni cliniche specifiche, ad esempio, in parte in neurochirurgia, e in studi di ricerca che coinvolgono ricostruzioni di ben noti percorsi neuronali.

Negli ultimi anni sono state proposte centinaia di diverse tecniche di trattografia. Al fine di valutare le loro prestazioni, abbiamo partecipato a diverse sfide internazionali. I risultati delle sfide hanno mostrato i vantaggi e i limiti dei moderni metodi di trattografia. In particolare, uno dei maggiori problemi che sono stati evidenziati è stata la mancanza di un gold standard. La trattografia a risonanza magnetica a diffusione è tipicamente convalidata con materiale post mortem e una concatenazione di classiche fette istologiche 2D. In questa tesi, proponiamo uno dei primi studi che utilizzano una nuova tecnica istologica 3D, denominata CLARITY, per convalidare l'orientamento delle fibre in un'ampia porzione di tessuto.

Alla risoluzione spaziale tipica della risonanza magnetica, circa il 60-90% dei voxel nella materia bianca contengono multiple popolazioni di fibre. Tuttavia, la maggior parte delle tecniche di imaging microstrutturale proposte non sono adatte a risolvere più popolazioni in un voxel. In questa tesi, abbiamo mirato a studiare i limiti dei moderni approcci, e abbiamo proposto metodi nuovi in cui la trattografia potrebbe giocare un ruolo cruciale. Proponiamo di utilizzare la microstruttura informata dalla trattografia per regolarizzare due importanti caratteristiche microstrutturali, cioè il diametro dell'assone e il  $T_2$ , mostrando gli evidenti vantaggi dell'uso di approcci globali e aprendo una nuova prospettiva per l'analisi della connettività. Tuttavia, il prezzo da pagare per aumentare la complessità dei modelli esistenti è un aumento dell'onere computazionale. Nell'appendice della tesi, proponiamo uno studio preliminare che utilizzo di approcci di reti neurali per accelerare il fitting globale di modelli complessi.



# Contents

<b>Acknowledgements</b>	<b>v</b>
<b>Abstract (English/Italiano)</b>	<b>vii</b>
<b>List of acronyms</b>	<b>xv</b>
<b>List of figures</b>	<b>xv</b>
<b>List of tables</b>	<b>xxii</b>
<b>Introduction</b>	<b>1</b>
Content of the thesis . . . . .	2
Relevant publications . . . . .	2
Other publications . . . . .	5
<b>1 Background</b>	<b>9</b>
1.1 Nervous system . . . . .	9
1.1.1 Neuron . . . . .	10
1.1.2 Brain organization . . . . .	10
1.1.3 Gray matter subdivision . . . . .	11
1.1.4 White matter subdivision . . . . .	11
1.1.5 Reconstructing the wiring of the brain . . . . .	13
1.2 Diffusion . . . . .	13
1.2.1 What is diffusion? . . . . .	13
1.2.2 When was diffusion observed for the first time? . . . . .	13
1.2.3 Fick's First Law . . . . .	14
1.2.4 Fick's Second Law . . . . .	15
1.2.5 Diffusion as a Random Walk . . . . .	15
1.2.6 Diffusion propagator . . . . .	17
1.3 Diffusion MRI . . . . .	18
1.3.1 Bloch and Bloch-Torrey equation . . . . .	18
1.3.2 Sensitizing the MRI signal to Diffusion . . . . .	19
1.3.3 Measuring the diffusion coefficient . . . . .	20
1.4 Microstructure Imaging . . . . .	20
1.4.1 Diffusion Tensor Imaging . . . . .	21

## Contents

---

1.4.2	Signal models . . . . .	23
1.4.3	Biophysical models . . . . .	23
1.5	Tractography . . . . .	25
1.5.1	Local approach . . . . .	25
1.5.2	Global approach . . . . .	28
1.6	Microstructure Informed Tractography . . . . .	29
1.6.1	Non linear methods . . . . .	29
1.6.2	Linear methods . . . . .	29
1.7	Thesis in a nutshell . . . . .	31
<b>2</b>	<b>International tractography challenges</b>	<b>33</b>
2.1	ISMRM 2015 Tractography . . . . .	33
2.1.1	Dataset and evaluation . . . . .	34
2.1.2	Results . . . . .	34
2.1.3	Discussion . . . . .	36
2.2	ISMRM 2017: Tractography-reproducibility with Empirical Data . . . . .	37
2.2.1	Dataset and evaluation . . . . .	38
2.2.2	Results . . . . .	39
2.2.3	Discussion . . . . .	40
2.3	ISBI 2018: 3-D Validation of Tractography with Experimental MRI . . . . .	41
2.3.1	Dataset and evaluation . . . . .	41
2.3.2	Results . . . . .	43
2.3.3	Discussion . . . . .	43
2.4	Conclusion and Discussion . . . . .	46
<b>3</b>	<b>Towards 3D histological validation of DW-MRI fiber orientation</b>	<b>47</b>
3.1	Introduction . . . . .	47
3.1.1	Estimating fiber orientation . . . . .	48
3.1.2	2D histology . . . . .	48
3.1.3	Tissue clearing and 3D histology . . . . .	48
3.2	Methods . . . . .	49
3.2.1	CLARITY-based tissue clearing acquisition . . . . .	49
3.2.2	MRI imaging acquisition . . . . .	50
3.2.3	Co-registration . . . . .	50
3.2.4	Structural tensor estimation . . . . .	52
3.2.5	Structural fiber orientation distribution estimation . . . . .	52
3.3	Results . . . . .	52
3.3.1	Localisation and co-registration . . . . .	52
3.3.2	Tensor comparison . . . . .	54
3.3.3	Orientation distribution function comparison . . . . .	56
3.4	Discussion . . . . .	59
3.4.1	Co-registration . . . . .	59
3.4.2	WM and GM fiber orientation comparisons . . . . .	60

3.4.3	CLARITY and microscopy imaging limitations . . . . .	60
3.5	Conclusion . . . . .	60
<b>4</b>	<b>Bundle-specific <math>T_2</math> mapping of cortical pathways</b>	<b>63</b>
4.1	Introduction . . . . .	63
4.1.1	$T_2$ Relaxation and supression extra-axonal signal . . . . .	64
4.1.2	Estimating $T_2$ in single population voxels . . . . .	64
4.1.3	Bundle-specific $T_2$ . . . . .	64
4.2	Methods . . . . .	65
4.2.1	Generative model . . . . .	65
4.2.2	Direction-averaged technique . . . . .	66
4.2.3	Voxel-wise formulation: AMICO- $T_2$ . . . . .	66
4.2.4	COMMIT- $T_2$ . . . . .	67
4.2.5	Protocol . . . . .	67
4.2.6	Numerical simulations . . . . .	68
4.2.7	In vivo data acquisition and preprocessing . . . . .	69
4.3	Results . . . . .	69
4.3.1	Numerical simulations . . . . .	69
4.3.2	Sensitivity analysis . . . . .	70
4.3.3	In vivo results . . . . .	72
4.4	Discussion . . . . .	75
4.5	Conclusion . . . . .	76
<b>5</b>	<b>Bundle-specific axon diameter mapping of cortical pathways</b>	<b>77</b>
5.1	Introduction . . . . .	77
5.2	Methods . . . . .	80
5.2.1	Axon diameter signatures . . . . .	80
5.2.2	Acquisition Protocol . . . . .	81
5.2.3	Numerical simulations: crossing configuration . . . . .	81
5.2.4	Numerical simulations: resolution limit . . . . .	82
5.2.5	Image processing . . . . .	83
5.2.6	Analysis of specific neuronal connections . . . . .	84
5.2.7	Histological preparation . . . . .	85
5.2.8	Histological analysis . . . . .	85
5.3	Results and Discussion . . . . .	86
5.3.1	<i>In-silico</i> analysis . . . . .	86
5.3.2	Bundles composition . . . . .	87
5.4	Conclusion . . . . .	91
<b>6</b>	<b>Conclusion</b>	<b>95</b>
6.1	Summary of the contributions . . . . .	95
6.2	Perspectives . . . . .	97

## Contents

---

<b>A Appendix: Learning global brain axon diameter index maps using trainable sparse encoders</b>	<b>101</b>
A.1 Introduction . . . . .	101
A.2 Methods . . . . .	102
A.2.1 Learned Sparse Encoding . . . . .	102
A.2.2 Dataset . . . . .	103
A.2.3 Neural Network Parameters . . . . .	104
A.3 Results . . . . .	104
A.4 Discussion . . . . .	106
A.5 Conclusion . . . . .	106
<b>Bibliography</b>	<b>107</b>
<b>Curriculum Vitae</b>	<b>137</b>







# List of Figures

1.1	Neuron structure. . . . .	10
1.2	The cerebral cortex is divided in four lobes: frontal lobe, parietal lobe, occipital lobe, and temporal lobe. . . . .	12
1.3	Illustration of Brownian motion. Left side free diffusion, right side restricted diffusion. From top to bottom the time increases. . . . .	16
1.4	Schematic representation of the Pulsed Gradient Spin Echo (PGSE) sequence. . . . .	19
1.5	Column one shows configurations of fibers that arise often in voxels (first column). Column two shows the diffusion pattern expected. The third column shows the Diffusion Tensor Imaging (DTI) fitting. The fourth column shows the principal direction of the DTI. In the last row, the DT is perfectly oblate so the principal direction is undefined. The fifth shows the Fiber Orientation Distribution (FOD) function. <i>The illustration is modified from [315].</i> . . . . .	22
1.6	Illustration of tractography. The goal of tractography is to reconstruct the White Matter (WM) bundles of the brain. In this illustration, we show streamlines of the Corpus Callosum (CC) connecting the left and right hemisphere of the brain. Streamlines can be colored according to a tissue property. Endpoints of the streamlines can be projected onto the cortex. . . . .	26
1.7	Example to illustrate the modeling of the Convex Optimization Modeling Microstructure Informed Tractography (COMMIT) framework. (a) The simulated Diffusion-Weighted Magnetic Resonance Imaging (DW-MRI) data, a tractography and a forward-model used to associate a signal contribution to each streamline. (b) The corresponding vector $y$ of DW-MRI measurements, the matrix $A$ encoding the signal contributions according to the forward-model of each streamline and the coefficients $x$ estimated by COMMIT. <i>The illustration is reproduced from [302].</i> . . . . .	30

## List of Figures

---

- 2.1 Top, row summarizes the overview of the numerical phantom generation. Bottom, 25 manually cleaned bundles by an expert radiologist; the bundles were segmented from a Human Connectome Project (HCP) data set whole-brain tractography. The bundles included in the study are the following: the CorticoSpinal Tract (CST), the Corpus Callosum (CC), Cingulum (CG), Optic Radiation (OR), Uncinate Fasciculus (UF), Superior Longitudinal Fasciculus (SLF), Inferior Longitudinal Fasciculus (ILF), Arcuate Fasciculus (AF), Posterior Commissure, Inferior Cerebellar Peduncle (ICP), Parieto-Occipital Pontine Tract (POPT), Superior Cerebellar Peduncle (SCP) and Fronto Pontine Tracts (FPT). In the middle is shown the connectivity plot of the phantom design. *Reprinted from [221], Copyright 2017, with permission from Springer Nature.* . . . . . 35
- 2.2 All the ground truth bundles are identified with the method proposed, however, the ratio of streamlines and their volume was not recovered correctly. (a) Averaged Volumetric OverLap (VOL) and the Volumetric OverReach (VOR) values of the submissions for the 25 bundles from the ground truth. Colors: blue - medium; green - hard; red - very hard. (b) Example of bundles for Diffusion Tensor Imaging (DTI) deterministic, High-Angular Resolution Diffusion Imaging (HARDI) deterministic, and HARDI probabilistic. The first column shows ground truth bundles. Volumetric OverLap (VOL) and Volumetric OverReach (VOR) scores are reported. *Reprinted from [221], Copyright 2017, with permission from Springer Nature.* . . . . . 36
- 2.3 Left side shows the overlay of all the submissions from all sessions. On the right an example of a single submission. More information of the name of the bundles can be found in the original manuscript [246]. *Reprinted from [246], Copyright 2019, with permission from International Society for Magnetic Resonance in Medicine.* . . . . . 38
- 2.4 Violin plots of intra-session submissions across both the scanners per tract. A) Dice similarity coefficients B) Intra-class correlation coefficients. The top row depicts the median of the top five intra-session submissions. More information of the name of the bundles can be found in the original manuscript [246]. *Reprinted from [246], Copyright 2019, with permission from International Society for Magnetic Resonance in Medicine.* . . . . . 39
- 2.5 Ground truth fiber pathways for the three sub-challenges. The figure shows different sections and visualizations for the three challenges. *Reprinted from [307], Copyright 2019, with permission from Elsevier Inc.* . . . . . 42
- 2.6 Example of diffusion tractography submitted to the challenge. Coronal and sagittal view. *Reprinted from [307], Copyright 2019, with permission from Elsevier Inc.* . . . . . 44

3.1	The photographs show the part of monkey brain tissue treated at Stanford University used for the Clear Lipid-exchanged Acrylamide- hybridized Rigid Imaging / In situ-hybridization-compatible / Immunostaining Tissue hYdrogel (CLARITY) clearing. (a.) Brain cut of the posterior lateral part of the left hemisphere (LLP). (b.) LLP4, the piece of tissue chosen for the analysis. (c.) LLP4 after clearing using the CLARITY protocol and lying inside a container. . . . .	49
3.2	Registration of the LLP4 monkey slab chosen for the analysis and acquired at Stanford University to the whole-brain b0 of a different monkey used in the work of Thomas et al.[335] From left to right: sagittal, coronal and axial view. . . . .	50
3.3	(a.) CLARITY two-photon microscopy images (b.) Registration of CLARITY two-photon microscopy images to the CLARITY overview 5x microscopy; registration helped by fluorescent bleaching. (c.) Registration of CLARITY overview 5x microscopy to structural MRI $T_1$ of slab LLP4. (d.) b-value=0 s mm <sup>-2</sup> of the Duke University MR monkey atlas used to annotate anatomical regions in visual cortex. (e.) b-value=0 s mm <sup>-2</sup> of NIMH monkey dataset used to co-register the CLARITY data (f.) Registration of structural MRI $T_1$ images of the slab LLP4 to the structural whole-brain $T_2$ MRI images. . . . .	51
3.4	Six different sections of the monkey brain corresponding to location for which CLARITY two-photon microscopy was acquired. The region corresponds roughly to the same section area. The investigation was performed by an expert anatomist.	53
3.5	2 dimensional (2D) histology of the section corresponding to the same location for which CLARITY two-photon microscopy images were acquired; the data correspond to the CCT4 monkey reported in the work [336]. (a) Overview image b) Zoomed image corresponding approximately to the CLARITY two-photon images. . . . .	54
3.6	2D histology of the section of white matter zoomed from the section in figure 3.5; data correspond to the CCT4 monkey reported in the work [336]. . . . .	55
3.7	Anatomical characterization of the LLP4 slab used for which CLARITY two-photon microscopy data were acquired. The Paxinos et al. [270] atlas was used to parcellate the visual cortical regions in V1, V2 and V3 ventral. . . . .	55
3.8	Tensor estimation on the region associated with CLARITY acquisition, and comparison. (a.) Structure tensor estimation; (b.) diffusion tensor estimation; (c.) angle of difference between the structure tensor and the diffusion tensor. Color code for figure (a.) (b.) are: red for right-left, blue for dorsal-ventral, and green for anterior-posterior. . . . .	56
3.9	Histogram of angle differences using the tensor analysis in (a.) Grey Matter (GM) (b.) White Matter (WM). . . . .	56

## List of Figures

---

3.10	Qualitative analysis of <i>ODFs</i> . Figure (a.) and (c.) show <i>FOD</i> estimated using constraint spherical deconvolution on NIMH macaque data [335]. Figure (b.) and (c.) show <i>sODF</i> varying the sub-voxel size, respectively, with sub-cubes of 2x2x2, 4x4x4, 8x8x8 and 16x16x16; spherical harmonics functions were computed using MrTrix[341] on CLARITY two-photon microscopy images. (a.) A grey matter voxel is highlighted on top of a <i>FOD</i> reconstruction. (b.) <i>sODF</i> estimations for a grey matter voxel highlighted in figure (a.), first-row show vectors, second-row show the corresponding <i>sODF</i> . (c.) A white matter voxel is highlighted on top of a <i>FOD</i> reconstruction. (d.) <i>sODF</i> estimations for the white matter voxel highlighted in figure (c.), first-row show vectors, second-row show the corresponding <i>sODF</i> . Qualitatively we report a variation of <i>sODF</i> shape varying the sub-voxel size. Voxels with high sub-cubes, i.e. 16x16x16, have <i>sODF</i> more noisy. . . . .	57
3.11	<i>ODF</i> analysis on DW-MRI data and CLARITY two-photon microscopy. First-column shows DW-MRI estimations; the other columns represent CLARITY two-photon microscopy estimations. First-row shows <i>fODF</i> and <i>sODF</i> , respectively for DW-MRI and CLARITY. Second-row show principal peak and third-row show multiple peaks extraction. . . . .	58
4.1	Noise level estimation on raw data and after denoising. . . . .	68
4.2	A cross-section of the synthetic phantom is visualized. The phantom simulates a crossing of two fiber bundles with different $T_2i$ values of $T_{2b1} = 78$ ms (in red color) and $T_{2b2} = 116$ ms (in green color), respectively. Voxels with a single and two fibers were differentiated to test the performance of the three evaluated methods: the direction-averaged technique, AMICO- $T_2$ , and COMMIT- $T_2$ . . . .	70
4.3	Histograms of the $T_2i$ values estimated in the phantom using the three evaluated methods: the direction-averaged technique, Accelerated Microstructure Imaging via Convex Optimization (AMICO)- $T_2$ , and Convex Optimization Modeling for Microstructure Informed Tractography (COMMIT)- $T_2$ . For more details see Figure 4.2. Results from both the noiseless and noisy datasets are reported. . .	70
4.4	Comparison of $T_2$ estimation against ground truth for the direction-averaged, AMICO- $T_2$ and COMMIT- $T_2$ methods. . . . .	71
4.5	Sensitivity analysis on the crossing phantom performed with COMMIT- $T_2$ where a new <i>SD_STREAM</i> tractography is generated. The study is performed in the noiseless and noisy cases. . . . .	71
4.6	Tractometry using $T_2$ values estimated with the direction-averaged technique. A portion of Corpus Callosum, Corticospinal tract and Arcatue Fasciculus is shown with streamlines colored by $T_2$ estimation. Below, we show the profile of the changing of $T_2$ along the bundles. . . . .	72

4.7  $T_2$  estimations using the direction-averaged, AMICO- $T_2$  and COMMIT- $T_2$ . The analysis is performed on three well-known bundles in the brain: Corpus Callosum (CC) and Posterior limb Internal Capsule (PIC) of the left and right hemisphere. The CC was subdivided in 11 equally distant different ROIs, while the PICs are subdivided in 6 ROIs. Comparison is performed considering the average along all voxels where the bundle is defined, where multiple population was occurred, and voxel where only one population is presented (defined as threshold of the Fractional Anisotropy (FA) map at 0.7). . . . . 73

4.8  $T_2$  estimations using the direction-averaged, AMICO- $T_2$  and COMMIT- $T_2$ . The analysis is performed on the arcuate fasciculus (AF), the cingulum (CG), the inferior fronto-occipital fasciculus (IFO), the inferior longitudinal fasciculus (SLF), the optic radiation (OR), the superior longitudinal fasciculus (SLF), and the uncinate fasciculus (UF). Comparison is performed considering the average along all voxels where the bundle is defined, where multiple populations occurred, and voxel where only one population is presented (defined as threshold of the fractional anisotropy (FA) map at 0.7). . . . . 74

5.1 The COMMIT framework. (a) Crossing configuration of cylinders with different diameter. Colors are associated with distinct voxels. (b) DW-MRI acquisition of the crossing configuration. (c,d) two main branches of tools able to process the DW-MRI signal: microstructure imaging, quantitative local estimation of tissue environment, i.e., axonal diameter; tractography, global estimation of trajectories, i.e., bundles. (e) COMMIT framework: unified expression of microstructure and tractography.  $y$ : DW-MRI signal acquired;  $A$ : matrix, express the model that integrates microstructure and tractography.  $x$ : volume fractions derived after the fitting. . . . . 80

5.2 Numerical simulations using histological prefrontal and parietal samples [55] were performed. (A) phantom shape and streamlines generated from: left) prefrontal area, right) motor area. (B) Estimation of axon diameter index (ADI) per streamline. Notice how prefrontal streamlines show a predominance of small diameter (blue) and motor area show predominance of large diameter (red). (C,D), show the axon diameter composition for prefrontal and motor areas. Different ranges were tested in order to find the DW-MRI sensitivity that is closest to the ground truth distributions, see Table 5.1. . . . . 83

5.3 Topology of fibers in the Corpus Callosum (CC) and posterior limb of the internal capsule (PIC), reconstructed with DW-MRI tractography. (A) Subdivision of the mid-sagittal section of the CC in 11 sectors (corresponding to ROIs). (B,C) Streamlines colored according to the corresponding ROIs (medial and lateral views of the hemisphere). (D) Projection of the streamlines into the pial surface. (E) Subdivision of PIC in 6 sectors (ROIs). (F,G) Streamlines colored according to the corresponding ROIs (medial and lateral view of the hemisphere). (H) Projection of the streamlines into the pial surface. . . . . 85

## List of Figures

---

5.4	Histological sampling CC sector 6. (A) Location of histological sampling in CC sector 6. (B) volume weighted distribution of the three samples. Sample 1 in Caminiti et al. (2009) has 1403 axons; sample 2, 451 axons and sample 3, 1934 axons. Significance of difference of samples are in <i>Table 5.2</i> . . . . .	86
5.5	Axon diameter estimation: voxel-wise ActiveAx original implementation and bundle-specific COMMIT. SNR=30, dispersion k=16. . . . .	88
5.6	Comparison of the fiber composition estimated with DW-MRI and histology in 4 CC sectors. The black curves represent axon diameter distributions (normalized to 1) of myelinated axons estimated with histology (dashed=number weighted, nw; continuous=volume weighted, vw). The three colored curves represent the axon diameter composition of bundles of streamlines passing through the respective CC sectors, scaled according to histology in the range 2 $\mu\text{m}$ to 6.5 $\mu\text{m}$ . . . . .	89
5.7	Fiber composition of the streamlines passing through the CC and PIC. (A,C) show streamlines colored according to their Axon Diameter Index (ADI). (B,D) show the projection of streamlines onto the pial surface; colors correspond to the ADI averaged across streamlines. Abbreviations: ces, central sulcus; ifs, inferior frontal sulcus; ips, interparietal sulcus; prs, precentral sulcus; sfs, superior frontal sulcus. Numbers correspond to Brodman areas. . . . .	90
5.8	DW-MRI axon diameter composition within CC and PIC sectors compared to histological mean volume-weighted axon diameter from human (CC) and monkey (PIC) histology. Stars represent means of the volume-weighted histological distributions; hexagons represent the means of volume-weighted distributions in the range 2 $\mu\text{m}$ to 6.5 $\mu\text{m}$ . . . . .	90
5.9	Reproducibility study on the comparison of axon diameters estimates with DW-MRI and histology in 4 CC sectors. The black curves represent axon diameter distributions (normalized to 1) of myelinated axons estimated with histology (dashed=number weighted, nw; continuous=volume weighted, vw). The three colored curves represent the axon diameter composition over streamlines passing through the respective CC sectors, scaled according to histology in the range 2 $\mu\text{m}$ to 6.5 $\mu\text{m}$ . For each diameter, the means and standard deviations over five acquisitions are shown. Reliable estimates of axon diameters could be obtained only between 2 $\mu\text{m}$ to 6.5 $\mu\text{m}$ . . . . .	91
5.10	Myelin-stained transversally-cut axons in sectors 6 (A) and 8 (B) of the Corpus Callosum (CC) of a human case. Scale bar is 10 $\mu\text{m}$ . Some of the axons are surrounded by a measuring circle. Notice the mediocre preservation of the tissue, unavoidable with human material. . . . .	92

A.1 a) Whole-brain tractography of one of the subjects of the HCP dataset; the white colour of the streamlines means that no quantitative information is associated to the tractography; b) Whole-brain tractography with streamlines colored according to the Axon Diameter Index (ADI) estimated using the COMMIT framework; c) Voxel-wise map of the mean Axon Diameter Index (mADI); left: sagittal view, top right: coronal view; bottom right: axial view. . . . . 103

A.2 a) axial view of the b0 image. b) Track Density Imaging [51] (TDI) counting the number of tractography streamlines passing through each voxel. c) Top: mADI map estimated with COMMIT; bottom: mADI map estimated with the neural network (NN). d) Top: EASF map estimated with COMMIT; bottom: EASF estimated with the NN. e) Map of the difference between the mADI estimated with COMMIT and with the NN. f) Map of the difference between EASF estimated with COMMIT and with the NN. . . . . 105





## List of Tables

5.1	Empirical testing for the resolution limit on simulated data. Discarding the first and last bin yields DW-MRI estimates that match the histological ground truth. <i>Associated to Fig.5.2.</i> . . . . .	84
5.2	Reproducibility histological sampling. <i>Table associated to Fig. 5.4</i> . . . . .	86
5.3	Axon diameter estimation: voxel-wise ActiveAx original implementation and bundle-specific COMMIT. . . . .	87



# Introduction

In this dissertation, we explore the advantages and limitations of Microstructure Informed Tractography through Diffusion-Weighted MRI (DW-MRI). The work was conducted under the supervision of Professor Jean-Philippe Thiran (EPFL, Switzerland) and Professor Alessandro Daducci (University of Verona, Italy), from September 2015 to August 2019.

This dissertation needs to be considered a parallel work to the thesis [296] defended by Dr. David Romascano, focused on modeling intra-axonal and extra-axonal signals using a voxel-wise approach. This dissertation is focused on tractography.

Tractography is the only technique available to infer non-invasive information of the brain White Matter (WM) structural connections. It can be used *in vivo*, since it uses a Magnetic Resonance Imaging (MRI) scanner to exploit protons' response to varying the magnetic field and estimate tissue properties, i.e., composition and geometry, in different brain's tissue locations indirectly. More specifically, tractography relies on two essential aspects: 1) orientations which indicates the direction of the white matter fibers, in a typical 3 dimensional (3D) grid, and 2) principles of how to connect the voxels to reconstruct the white matter connections.

Tractography is a relatively young technique which has been proposed 20 years ago. It is used in a few clinical applications, e.g., neurosurgery, and in research studies that involve reconstructions of well-known neuronal pathways. However, it is not widely used in clinical practice because up to date has significant limitations and controversial findings, e.g., Furthermore, a non existence of a proper ground truth and a lack of proper validation technique is a compound.

In this thesis, we learned the limitations of modern tractography methods participating at three international challenges between 2015 and 2019. We proposed a novel approach that uses 3D histology and can potentially be used to validate tractography algorithms. We proposed two novel methods for Microstructure Informed Tractography aiming to estimate bundle-specific  $T_2$  and axon diameter. Finally, in the appendix we proposed a neural network approach for Microstructure Informed Tractography.

## Content of the thesis

The structure of this dissertation is as follows:

1. Chapter 1, we provide a brief state of art and theory regarding brain anatomy, diffusion process, DW-MRI, microstructure imaging, tractography and finally microstructure informed tractography.
2. Chapter 2, we provide an overview of the major tractography international challenges proposed between 2015 and 2019 and their findings.
3. Chapter 3, we propose to use a recently introduced 3D histology technique, named CLARITY, to validate medium-range length connections on primate brain; furthermore we developed the first FOD analysis for CLARITY-based data.
4. Chapter 4, we provide an algorithm that uses microstructure informed tractography to disentangle a specific physical property, i.e., intra-axonal  $T_2$ , showing the advantages in solving crossing fibers.
5. Chapter 5, we provide a second algorithm which uses microstructure informed tractography to estimate a biological property, i.e. axonal diameter, showing the advantages in using tractography to cope with dispersion and complex geometries; the strength of the work lies in the reproducibility studies performed and in the validation of the results through 2D histology.
6. Chapter 6, we propose a neural network to reduce the computational burden of microstructure informed tractography; this has to be considered a preliminary study and propose a novel approach for microstructure informed tractography
7. Appendix, we review the main contributions of each chapter in this dissertation, and provide various directions for future research.

## Relevant publications

The contributions presented in this thesis have been shared publicly as follows:

### Chapter 2 - International tractography challenges

1. Klaus Maier-Hein, Peter F. Neher, Jean-Christophe Houde, Marc-Alexandre Cote, Eleftherios Garyfallidis, Jidan Zhong, Maxime Chamberland, Fang-Cheng Yeh, Ying-Chia Lin, Qing Ji, Wilburn E. Reddick, John O. Glass, David Qixiang Chen, Yuanjing Feng, Chengfeng Gao, Ye Wu, Jieyan Ma, H. Renjie, Qiang Li, Carl-Fredrik Westin, Samuel Deslauriers-Gauthier, J. Omar Ocegueda González, Michael Paquette, Samuel St-Jean,

- Gabriel Girard, François Rheault, Jasmeen Sidhu, Chantal M. W. Tax, Fenghua Guo, Hamed Y. Mesri, Szabolcs Dávid, Martijn Froeling, Anneriet M. Heemskerk, Alexander Leemans, Arnaud Boré, Basile Pinsard, Christophe Bedetti, Matthieu Desrosiers, Simona Brambati, Julien Doyon, Alessia Sarica, Roberta Vasta, Antonio Cerasa, Aldo Quattrone, Jason Yeatman, Ali R. Khan, Wes Hodges, Simon Alexander, David Romascano, **Muhamed Barakovic**, Anna Auria, Oscar Esteban, Alia Lemkaddem, Jean-Philippe Thiran, H. Ertan Cetingul, Benjamin L. Odry, Boris Mailhe, Mariappan S. Nadar, Fabrizio Pizzagalli, Gautam Prasad, Julio E. Villalon-Reina, Justin Galvis, Paul M. Thompson, Francisco De Santiago Requejo, Pedro Luque Laguna, Luis Miguel Lacerda, Rachel Barrett, Flavio Dell'Acqua, Marco Catani, Laurent Petit, Emmanuel Caruyer, Alessandro Daducci, Tim B. Dyrby, Tim Holland-Letz, Claus C. Hilgetag, Bram Stieltjes, Maxime Descoteaux, "The challenge of mapping the human connectome based on diffusion tractography", *Nature Communications*, 2017
2. Vishwesh Nath, Kurt G. Schilling, Prasanna Parvathaneni, Yuankai Huo, Justin A. Blaber, Allison E. Hainline, **Muhamed Barakovic**, David Romascano, Jonathan Rafael-Patino, Matteo Frigo, Gabriel Girard, Jean-Philippe Thiran, Alessandro Daducci, Matt Rowe, Paulo Rodrigues, Vesna Prckovska, Dogu B. Aydogan, Wei Sun, Yonggang Shi, William A. Parker, Abdol A. Ould Ismail, Ragini Verma, Ryan P. Cabeen, Arthur W. Toga, Allen T. Newton, Jakob Wasserthal, Peter Neher, Klaus Maier-Hein, Giovanni Savini, Fulvia Palesi, Enrico Kaden, Ye Wu, Jianzhong He, Yuanjing Feng, Michael Paquette, Francois Rheault, Jasmeen Sidhu, Catherine Lebel, Alexander Leemans, Maxime Descoteaux, Tim B. Dyrby, Hakmook Kang, Bennett A. Landman, "Tractography reproducibility challenge with empirical data (TraCED): The 2017 ISMRM diffusion study group challenge", *J. Magn. Reson. Imaging*, 2019
  3. Kurt G. Schilling, Vishwesh Nath, Colin Hansen, Prasanna Parvathaneni, Justin Blaber, Yurui Gao, Peter Neher, Dogu Baran Aydogan, Yonggang Shi, Mario Ocampo-Pineda, Simona Schiavi, Alessandro Daducci, Gabriel Girard, **Muhamed Barakovic**, Jonathan Rafael-Patino, David Romascano, Gaetan Rensonnet, Marco Pizzolato, Alice Bates, Elda Fisci, Jean-Philippe Thiran, Erick J. Canales-Rodriguez, Chao Huang, Hongtu Zhu, Liming Zhong, Ryan Cabeen, Arthur W. Toga, Francois Rheault, Guillaume Theaud, Jean-Christophe Houde, Jasmeen Sidhu, Maxime Chamberland, Carl-Fredrik Westin, Tim B. Dyrby, Ragini Verma, Yogesh Rathi, M. Okan Irfanoglu, Cibu Thomas, Carlo Pierpaoli, Maxime Descoteaux, Adam W. Anderson, Bennett A. Landman, "Limits to anatomical accuracy of diffusion tractography using modern approaches", *NeuroImage*, 2018

### Chapter 3 - Towards 3D histological validation of diffusion MRI fibre orientation

1. **Muhamed Barakovic**, Christoph Leuze, Ailey K. Crow, Qiyuan Tian, Alessandro Daducci, Giorgio M. Innocenti, Jean-Philippe Thiran, Karl Deisseroth, Jennifer McNab, "Estimating fibre orientation using CLARITY and diffusion MRI in macaque visual cortex", *in preparation* for *NeuroImage*

## List of Tables

---

2. Christoph Leuze, Maged Goubran, Markus Aswendt, Qiyuan Tian, **Muhamed Barakovic**, Brian Hsueh, Ailey Crow, Gary Steinberg, Michael Zeineh, Ed Plowey, Karl Deisseroth, Jennifer McNab, "Comparison of diffusion MRI and CLARITY fiber orientation estimates in the same human brain tissue", *submitted to NeuroImage*
3. **Muhamed Barakovic**, Christoph Leuze, Ailey K. Crow, Qiyuan Tian, Alessandro Daducci, Jean-Philippe Thiran, Karl Deisseroth, Jennifer McNab, "Comparing Fiber Orientation Estimates from CLARITY and Diffusion MRI in Macaque Visual Cortex", 27th annual meeting of the International Society for Magnetic Resonance in Medicine (ISMRM), Montreal, Canada, May 11-16, 2019

## Chapter 4 - Bundle-specific T2 of cortical pathways

1. **Muhamed Barakovic**, Chantal MW. Tax, Umesh S. Rudrapatna, Jonathan Rafael-Patino, Jean-Philippe Thiran, Alessandro Daducci, Erick J. Canales-Rodriguez, Derek K. Jones, "Resolving intra-voxel, intra-axonal  $T_2$  heterogeneity using tract-based estimation", *in preparation for NeuroImage*

## Chapter 5 - Axon diameter signatures of cortical pathways

1. **Muhamed Barakovic**, Gabriel Girard, David Romascano, Simona Schiavi, Maxime Descoteaux, Derek K. Jones, Giorgio M. Innocenti, Jean-Philippe Thiran, Alessandro Daducci, "Axon diameter signatures of human cortical pathways in vivo", *submitted to NeuroImage*
2. **Muhamed Barakovic**, Gabriel Girard, David Romascano, Jonathan Patino-Lopez, Maxime Descoteaux, Derek K. Jones, Giorgio M. Innocenti, Jean-Philippe Thiran, Alessandro Daducci, "Assessing feasibility and reproducibility of a bundle-specific framework on in vivo axon diameter estimates at 300mT/m", 26th annual meeting of the International Society for Magnetic Resonance in Medicine (ISMRM), Paris, France, June 16-21, 2018
3. **Muhamed Barakovic**, Gabriel Girard, David Romascano, Jonathan Patino-Lopez, Maxime Descoteaux, Derek K. Jones, Giorgio M. Innocenti, Jean-Philippe Thiran, Alessandro Daducci, "In-vivo Bundle-Specific Axon Diameter Distributions Estimation across the Corpus Callosum", 25th annual meeting of the International Society for Magnetic Resonance in Medicine (ISMRM), Honolulu, USA, April 22-27, 2017
4. **Muhamed Barakovic**, David Romascano, Gabriel Girard, Maxime Descoteaux, Jean-Philippe Thiran, Alessandro Daducci, "Combining Tractography and Microstructure to Assess Bundle-Specific Axon Diameter Distributions", International Society for Magnetic Resonance in Medicine (ISMRM) Workshop on breaking the barriers of Diffusion MRI, Lisbon, Portugal, September 11-16, 2016

5. **Muhamed Barakovic**, David Romascano, Tim B. Dyrby, Daniel C. Alexander, Jean-Philippe Thiran, Alessandro Daducci, "Assessment of bundle-specific axon diameter distributions using diffusion MRI tractography", 22nd Annual Meeting of the Organization for Human Brain Mapping (OHBM), Geneva, Switzerland, June 26-30, 2016

#### **Appendix - Learning global brain axon diameter index maps using trainable sparse encoders**

1. **Muhamed Barakovic**, Jonathan Patino-Lopez, Gabriel Girard, Alessandro Daducci, Jean-Philippe Thiran, "Learning global brain microstructure maps using trainable sparse encoders", 26th IEEE International Conference on Image Processing (ICIP), Taipei, Taiwan, September 22-25, 2019

#### **Other publications**

I also contributed to other publications whose content is not addressed in this dissertation:

#### **Journal papers**

- Peter Rogelj, **Muhamed Barakovic** "Cervix Cancer Spatial Modelling for Brachytherapy Applicator Analysis", Informatica - An International Journal of Computing and Informatics, 2015
- Erick J. Canales-Rodriguez, Jon Haitz Legarreta, Marco Pizzolato, Gaetan Rensonnet, Gabriel Girard, Jonathan Rafael-Patino, **Muhamed Barakovic**, David Romascano, Yasser Aleman-Gomez, Joaquim Radua, Edith Pomarol-Clotet, Raymond Salvador, Jean-Philippe Thiran, and Alessandro Daducci, "Sparse wars: A survey and comparative study of spherical deconvolution algorithms for diffusion MRI", NeuroImage, 2018
- Matteo Battocchio, Gabriel Girard, **Muhamed Barakovic**, Mario Ocampo, Jean-Philippe Thiran, Simona Schiavi, Alessandro Daducci, "Improving Graph-Based Tractography Plausibility Using Microstructure Information", In: Bonet-Carne E., Grussu F., Ning L., Sepelband F., Tax C. (eds) Computational Diffusion MRI. MICCAI, 2018
- Jonathan Rafael-Patino, Thomas Yu, **Muhamed Barakovic**, Victor Delvigne, Erick J. Canales-Rodriguez, Marco Pizzolato, Derek K. Jones, Jean-Philippe Thiran, "DWI simulation-assisted machine learning models for microstructure estimation", Computational Diffusion MRI. MICCAI, 2019
- Simona Schiavi, **Muhamed Barakovic**, Mario Ocampo-Pineda, Maxime Descoteaux, Jean-Philippe Thiran, Alessandro Daducci, "Reducing false positives in tractography with microstructural and anatomical priors", bioRxiv, 2019

## List of Tables

---

- David Romascano, **Muhamed Barakovic**, Jonathan Rafael-Patino, Tim B. Dyrby, Jean-Philippe Thiran, Alessandro Daducci, "ActiveAxADD : towards non-parametric and orientationally invariant axon diameter distribution mapping using PGSE", *submitted* to Magn. Reson. Imaging
- Francois Rheault et al., "Tractostorm: The what, why and how of tractography dissection reproducibility", *submitted* to NeuroImage
- David Romascano, Erick J. Canales-Rodriguez, Jonathan Rafael-Patino, Marco Pizzolato, Gaetan Rensonnet, **Muhamed Barakovic**, Gabriel Girard, Alessandro Daducci, Tim B. Dyrby and Jean-Philippe Thiran, "HOTmix: Characterizing hindered compartments in diffusion MRI using a mixture of higher order tensors", *in preparation*

## Conferences

- Mohammad Ashtarayeh, Tobias Streubel, Joao Periquito, Andreas Pohlmann, Thoralf Niendorf, Evgeniya Kirilina, Markus Morawski, Carsten Jager, Stefan Geyer, **Muhamed Barakovic**, Alessandro Daducci, Siawoosh Mohammadi, "Axon diameter estimation in fixed human optic chiasm using diffusion weighted MR microscopy and microstructure-informed tractography", 27th annual meeting of the International Society for Magnetic Resonance in Medicine (ISMRM), Montreal, Canada, May 11-16, 2019
- Mario Ocampo-Pineda, Simona Schiavi, Matteo Frigo, **Muhamed Barakovic**, Gabriel Girard, Maxime Descoteaux, Jean-Philippe Thiran, Alessandro Daducci, "Reducing false-positive connections using hierarchical microstructure-informed tractography", 27th annual meeting of the International Society for Magnetic Resonance in Medicine (ISMRM), Montreal, Canada, May 11-16, 2019
- Mohammad Ashtarayeh, **Muhamed Barakovic**, Tobias Streubel, Joao Periquito, Andreas Pohlmann, Thoralf Niendorf, Evgeniya Kirilina, Markus Morawski, Carsten Jager, Stefan Geyer, Alessandro Daducci, Siawoosh Mohammadi, "Axon diameter index estimation in fixed human optic chiasm: voxel or streamline space?" 25th Annual Meeting of the Organization for Human Brain Mapping (OHBM), Rome, Italy, June 9-13, 2019
- Alessandro Daducci, **Muhamed Barakovic**, Gabriel Girard, Maxime Descoteaux, Jean-Philippe Thiran, "Reducing false positives in tractography with microstructural and anatomical priors", 26th annual meeting of the International Society for Magnetic Resonance in Medicine (ISMRM), Paris, France, June 16-21, 2018
- David Romascano, Jonathan Rafael-Patino, Ileana Jelescu, **Muhamed Barakovic**, Tim B. Dyrby, Jean-Philippe Thiran and Alessandro Daducci, "Voxel size matters: big voxels are required to generate realistic extra-axonal dMRI signals from Monte Carlo simulations", 26th annual meeting of the International Society for Magnetic Resonance in Medicine (ISMRM), Paris, France, June 16-21, 2018



- Jonathan Patino-Lopez, Gabriel Girard, David Romascano, **Muhamed Barakovic**, Gaetan Renzonnet, Jean-Philippe Thiran, Alessandro Daducci, "Realistic 3D Fiber Crossing Phantom Models for Monte Carlo Diffusion Simulations", 26th annual meeting of the International Society for Magnetic Resonance in Medicine (ISMRM), Paris, France, June 16-21, 2018
- **Muhamed Barakovic**, David Romascano, Gabriel Girard, Maxime Descoteaux, Jean-Philippe Thiran, Alessandro Daducci, "When does a volume of a bundle achieve saturation? A microstructure informed tractography study", 25th annual meeting of the International Society for Magnetic Resonance in Medicine (ISMRM), Honolulu, USA, April 22-27, 2017
- David Romascano, **Muhamed Barakovic**, Anna Auria, Tim B. Dyrby, Jean-Philippe Thiran and Alessandro Daducci, "Orientation invariant and non-parametric Axon Diameter Distribution mapping using PGSE and regularized discrete linear modeling", 25th annual meeting of the International Society for Magnetic Resonance in Medicine (ISMRM), Honolulu, USA, April 22-27, 2017
- Matteo Frigo, **Muhamed Barakovic**, Jean-Philippe Thiran, Alessandro Daducci, "Hierarchical Tractography Optimisation", Computational Brain Connectivity Mapping Winter School Workshop, Juan les Pins, France, 2017
- David Romascano, **Muhamed Barakovic**, Anna Auria, Tim B. Dyrby, Jean-Philippe Thiran and Alessandro Daducci, "Is it Feasible to Estimate Rotation-Invariant Non-Parametric Axon Diameter Distributions from PGSE? Preliminary Insights from Regularized Discrete Linear Modeling and Simulated Intra-Axonal Signals", ISMRM Workshop on breaking the barriers of Diffusion MRI, Lisbon, Portugal, September 11-16, 2016



# 1 Background

This chapter aims to review the basic principles behind the central nervous system (CNS) and Diffusion-Weighted Magnetic Resonance Imaging (DW-MRI), with a focus on microstructure imaging and tractography. We will not examine the anatomy of the brain in detail, and we will not discuss the basics of Magnetic Resonance Imaging (MRI), concepts that are widely explained in several books [48, 52]. However, we will furnish basic knowledge to understand how to study the human brain structure with a non-invasive technology.

In this background chapter, we introduce crucial elements which will allow understanding the other chapters of the thesis. The first section describes elements of the nervous system, which is the system that we want to study. Then, the diffusion phenomenon is introduced, which indirectly gives us information about the structure. The technique that will be used to measure diffusion in the brain is DW-MRI. The last two sections will deal with microstructure imaging, which gives us information at the voxel level, and finally tractography, which will give us an opportunity to connect voxels and reconstruct neuronal pathways in the brain.

## 1.1 Nervous system

The indispensable elementary unit of the nervous system is the neuron, Figure 1.1. In the human brain, billions of neurons process and transmit information, creating a highly organized and complex network.

The body and the surrounding environment send information to the nervous system, which receives, filters, possibly stores and then transmits, generating a command. More specifically, the nervous system has receptors, which convert stimuli to electrical discharges, i.e., nerve impulses, and directs them along the nerve to the cell bodies, where information processing occurs. Furthermore, it can also evoke external responses in the muscles or glands to generate movement or secretion. In this context, it assures that the body reacts appropriately to the environment.

## Chapter 1. Background

---

The nervous system is divided in the CNS, composed by the spinal cord and the brain, and the Peripheral Nervous System (PNS), which links the CNS to receptors and effectors. In this thesis, we will focus on the brain.

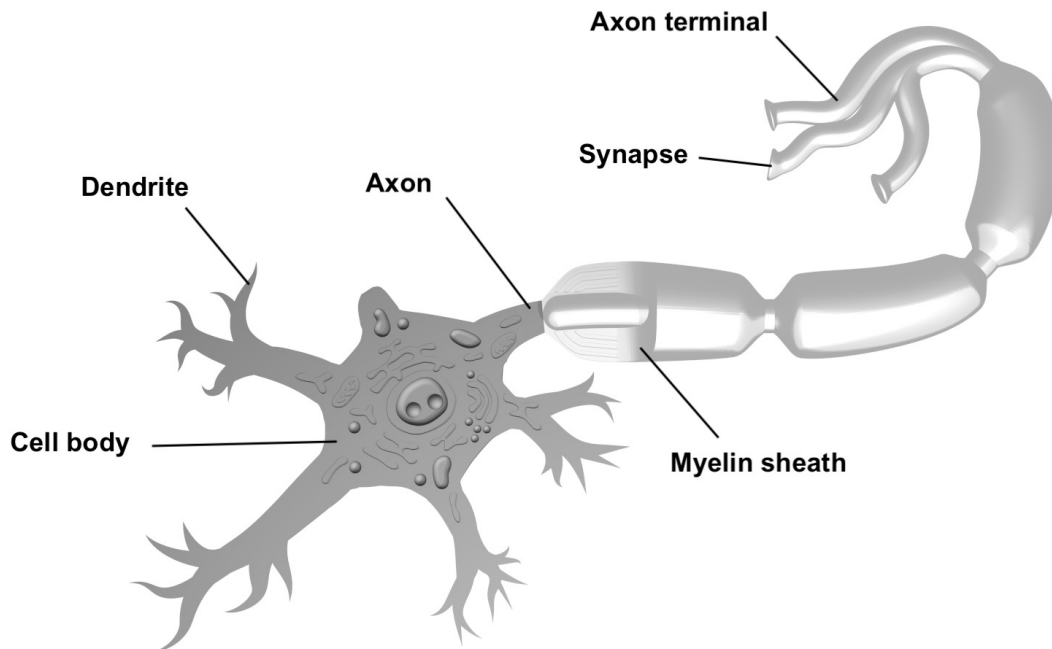


Figure 1.1 – Neuron structure.

### 1.1.1 Neuron

The nervous system architecture is structured with neurons and glial cells. Neurons are responsible for the functions, glial cells protect and support the neurons.

Neurons are composed of a cell body, of multiple short dendrites, which receives input from other neurons, and of a single axon which conducts the nerve impulse. When the nerve impulse reaches the location of the connection between neurons, i.e., synapse, a neurotransmitter is released to the axon terminal. Furthermore, axons are surrounded with a myelin sheath which serves as an insulator and increases the impulse conduction velocity [274].

### 1.1.2 Brain organization

The cerebral hemispheres, the cerebellum, and the brainstem subdivide the brain into three parts. The cerebral hemispheres consist of the Grey Matter (GM), the outer portion containing cell bodies, the White Matter (WM), the inner portion where axons reside, and the ventricles, which are areas filled with Cerebrospinal Fluid (CSF). The cerebral hemispheres are the largest part of the human brain, are the most developed portions of the CNS, and are connected by

the Corpus Callosum (CC). A midline portion and two lateral lobes compose the cerebellum. The diencephalon, midbrain, pons, and medulla constitute the brainstem.

In this thesis we will focus mainly on the WM.

### 1.1.3 Gray matter subdivision

The cerebral cortex, placed on the surface of the brain, is a sheet of neural tissue folded to allow a large surface area to fit in the skull. Cortical ridges are gyri and cortical grooves or fissures separating one gyrus from another with sulci.

The cerebral cortex is approximately symmetrical with two hemispheres connected by the sagittal fissure. Different subdivisions of the cerebral cortex were proposed during the years [12, 17, 69, 94, 107, 113, 128, 140, 142, 143, 159, 300, 347, 375]; here, we report the primary conventional subdivision which divides each hemisphere into four macro-areas lobes: the frontal, parietal, occipital, and temporal lobes; (See Figure 1.2). The frontal lobe is in front of the brain and is associated with higher level cognition, motor skills, reasoning, and expressive language [318]; in the posterior part of the frontal lobe lies the motor cortex which is related to body movements. In the middle section of the brain is located the parietal lobe, which is associated with sensory information such as pressure, touch, and pain [134]. On the bottom section is located the temporal lobe which is associated with the primary auditory cortex, related to speech perception, and the hippocampus, which is related to memory [327]. At the posterior part of the brain is located the occipital lobe, which is associated with interpreting visual stimuli [357].

### 1.1.4 White matter subdivision

Neural tracts form the connections between the distinct functional regions in the cerebral cortex. Neural tracts can be divided into three main categories:

- *Projection tracts* establish connections between the subcortical structures, i.e., basal ganglia and the thalamus, and the cerebral cortex. Projection tracts also establish the connections between the brain and the spinal cord. These are of two types:
  - *Afferent tracts* build up connections to the cerebral cortex from different regions of the body. Except for the olfactory sensory information, all the other sensory information end up in the primary sensory cortex.
  - *Efferent tracts* are the communication fibers from the motor cortex to the glands and muscles, passing through lower brain structures and the spinal cord.
- *Association tracts* establish connections between cortical areas within a hemisphere. They are subdivided into two categories:

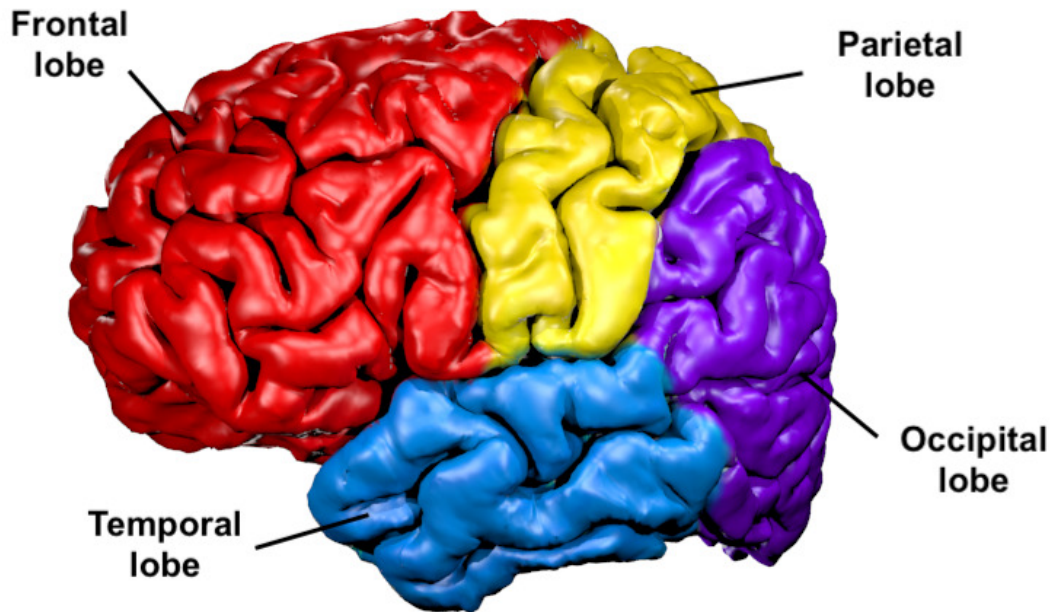


Figure 1.2 – The cerebral cortex is divided in four lobes: frontal lobe, parietal lobe, occipital lobe, and temporal lobe.

- *Short association tracts* establish connections with adjacent gyri and they build up connections within a given lobe, an example are the so-called "U-fibers."
- *Long association fibers* carry information between different cerebral lobes passing through different brain areas. An example of long association fibers is the Uncinate Fasciculus (UF) which goes from the temporal to the frontal lobe.
- *Commissural tracts* build up connections from a region in one hemisphere to another area of the opposite hemisphere. An example of commissural tract is the transcallosal fibers.

In the literature, there has not always been an agreement in the classification and use of "fibers", "fascicles", "bundles", "tracts" and "pathways". A recent study proposed a unified classification [224]. In this thesis, we propose the following classification:

- set of spacially coherent axons: fiber. In the DW-MRI community, we use incorrectly the notion of streamline to think about the fiber. However, the streamline is the output of tractography and is different from a fiber.
- set of fibers: bundle or fascicle or tract
- combinations of fibers/bundles/tract: pathway (synopsis in between)

### 1.1.5 Reconstructing the wiring of the brain

Reconstructing the wiring of the human brain is a crucial step to understand its function. During the past years, several methods have been proposed. We can divide the methods into two main categories: *ex vivo* and *in vivo*. With *ex vivo* studies, the community discovered most of the white-matter connections using tracers. Tracers have the advantage of higher anatomical accuracy, and they use natural axonal transport mechanisms. *In vivo* studies have been conducted mainly with DW-MRI and functional Magnetic Resonance Imaging (fMRI) [204]. In this second category, tractography, which can be associated to virtual dissection, is the tool of choice for inferring white matter structure.

Till now, the results of *in vivo* studies of wiring of the brain are less accurate compared to those of the *ex vivo* studies; however, there are definite advantages, e.g., they can be used for longitudinal and comparative studies.

## 1.2 Diffusion

In this section, we will address concepts of diffusion at the macroscopic scale. Furthermore, we will try, when possible, to historically reconstruct the key events that led the advance of knowledge in diffusion and DW-MRI as it is known today.

### 1.2.1 What is diffusion?

Diffusion is a mass transport process whereby molecules change their position as a result of random, thermally-driven collisions. Commonly, diffusion is reported as an expression of a change in molecular displacement from an area of high concentration to low concentration. Thanks to this property, inhomogeneous materials can become homogeneous. However, diffusion happens also in the absence of a macroscopic concentration gradient; in this case, we speak about "self-diffusion", a process derived by local concentration fluctuations.

Diffusion process differs from advection. Advection occurs with the bulk flow, and it is characterized by a macroscopic effect that involves the entire fluid, e.g., river streaming from a high point to a low point. On the contrary, diffusion occurs without any bulk flow.

### 1.2.2 When was diffusion observed for the first time?

Often the discovery of the diffusion process is attributed to a Scottish botanist Robert Brown (1773 - 1858) [44]. However, this phenomena has been probably observed by many scientists throughout history. The Roman poet and philosopher Titus Lucretius Carus (99 BC - c. 55 BC) in his scientific poem *De Rerum nature* [59] report a phenomenon that can be brought back to the observations of Robert Brown:

*"Observe what happens when sunbeams are admitted into a building and shed light on its*

## Chapter 1. Background

---

*shadowy places. You will see a multitude of tiny particles mingling in a multitude of ways... their dancing is an actual indication of underlying movements of matter that are hidden from our sight... It originates with the atoms which move of themselves*". Although the jiggling dust particles in light seen by Lucretius was probably largely caused by advection of air currents, there was probably a diffusion component in the tumbling motion of small particles caused by diffusion.

The diffusion process was not been commented during history until 1785 when the Dutch physiologist, biologist and chemist Jan Ingenhousz (1730-1799) reported a random motion of coal dust particles on the surface of alcohol [161]. Although Ingenhousz reported a phenomenon that can be related to diffusion, it is not clear if he was the first person able to state the random motion of particles. The uncertainty of the attribution of the discover can be attributed to the lack of information on the microscope used, doubts about the experimental conditions, and quick evaporation of the liquid used.

Therefore, currently the observation of diffusion is commonly associated to Robert Brown, who in 1827 described grains of pollen wiggling around in water [44], what we refer nowadays as "Brownian motion".

### 1.2.3 Fick's First Law

Inspired by the work of the Scottish chemist Thomas Graham (1805-1869) on diffusion of salts in water [144] and of the French mathematician and physicist Joseph Fourier (1768-1830) on his law of thermal conduction [130], in 1855 Adolf Eugen Fick (1829-1901), a German physician and physiologist, introduced for the first time the diffusion coefficient. Fick identified the first quantitative measure of diffusion, relating molecular displacement through time.

In his work [119], he studies the diffusion flux to concentration. The phenomena are described in "Fick's first law" which states that the diffusion flux is proportional to the negative of the concentration gradient and goes from a region of high concentration to region of low concentration. In one dimension, the law is:

$$J = -D_0 \frac{d}{dx} c(\mathbf{r}, t) \quad (1.1)$$

where  $J$  is the diffusion flux and measures the amount of substance which flow,  $D_0$  is the diffusivity or diffusion coefficient,  $c$  is the concentration and  $x$  is the position. In two or more dimensions we have:

$$J = -D_0 \nabla c(\mathbf{r}, t) \quad (1.2)$$

where  $\nabla$  is the gradient operator.



### 1.2.4 Fick's Second Law

From the continuity equation of the conservation of mass:

$$\frac{d}{dx}c(\mathbf{r}, t) + \nabla \cdot \mathbf{J} = 0 \quad (1.3)$$

We combine (1.2) and (1.3) and derive "Fick's second law" or diffusion equation:

$$\frac{d}{dt}c(\mathbf{r}, t) = \nabla \cdot (D_0 \nabla c(\mathbf{r}, t)) = D_0 \nabla^2 c(\mathbf{r}, t) \quad (1.4)$$

where  $\nabla^2$  is the Laplace operator.

Here, there is an implicit dependence on the starting point at 0,  $P(\mathbf{r}, t) = P(\mathbf{r}|\mathbf{r}_0, t)$ , and this quantity is known as the propagator, which give us the probability to be found at the position  $\mathbf{r}$  given that we start at  $\mathbf{r}_0$  at  $t = 0$ .

We assume that  $D_0$  is constant, which is a good assumption for diffusion in water.

Fick's Laws in (1.2) and (1.4), describe mutual diffusion, where particles drift from higher to lower concentration. Albert Einstein (1879-1955), applied the same idea to self-diffusion, the case without a macroscopic concentration gradient and interpreted the phenomena in terms of probability.

### 1.2.5 Diffusion as a Random Walk

Even though the single molecules do not have a preferred direction of motion, if there exists a concentration gradient then over time you see a diffusive flux from high to low concentration. The motion of a single molecule can be described in terms of "random walks".

From the discovery of Brownian motion passed seven decades before some progress in the field happened. During this period, physicist like the Scottish James Clerk Maxwell (1831-1879), the Austrian Ludwig Eduard Boltzmann (1844-1906) and the German Rudolf Julius Emanuel Clausius (1822-1888), founders of the kinetic theory, tried to measure the velocity of particles, without success.

It is only around 1900 that the physicists Albert Einstein and the Polish physicist Marian Smoluchowski (1872-1917) started to gain understanding about Brownian motion, and they understood that velocity is not a useful feature to be characterized.

The simplest mathematical model that can be related to Brownian motion[71] is the "random walks"; a term introduced by the French mathematician Louis Jean-Baptiste Alphonse Bachelier (1870-1946) in his Ph.D. thesis [20] and the English mathematician Karl Pearson with his letter to Nature [271].

Einstein studied the Brownian motion [108–111] and concluded that it was associated

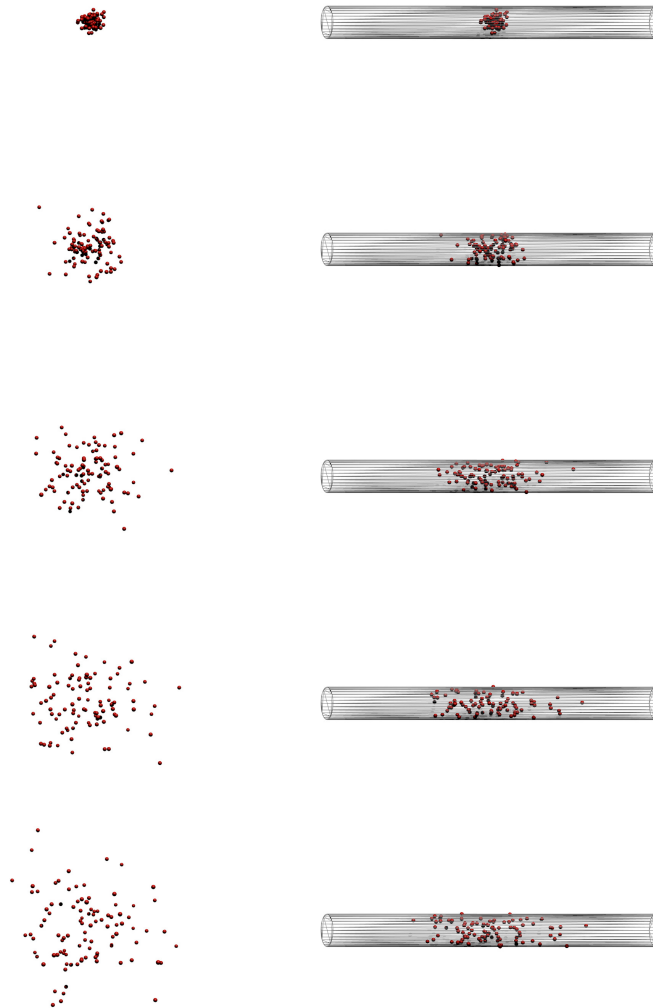


Figure 1.3 – Illustration of Brownian motion. Left side free diffusion, right side restricted diffusion. From top to bottom the time increases.

with diffusion. Furthermore, he concluded that the fundamental quantity is the mean-square displacement and not the velocity. Moreover, he related the mean square-displacement with the diffusion coefficient. During the same period, Smoluchowski worked on the Brownian motion and published his first papers right after the first Einstein publication [354, 355].

In 1909, the physicist Jean Baptiste Perrin (1870-1942) confirmed the Einstein's Brownian motion equation [275], proved the existence of water molecules, and estimated its size, winning the Nobel Prize for Physics in 1926.

In the random walks model, particles start from a position  $\mathbf{r}_0$  and move freely with velocity

$\mathbf{v}_i$  for time  $\tau$ . They collide with another particle, and they change their velocity  $\mathbf{v}_{i+1}$  randomly. This process is repeated. The position  $\mathbf{r}_n$  after  $n$  steps is:

$$\mathbf{r}_n = \mathbf{r}_0 + \tau \sum_{i=1}^n \mathbf{v}_i \quad (1.5)$$

The corresponding time elapsed is  $t = n\tau$ .

What characterizes diffusion is that there is no net transport and the mean distance traversed is zero:

$$\langle \mathbf{r}_n - \mathbf{r}_0 \rangle = \tau \sum_{i=1}^n \langle \mathbf{v}_i \rangle = 0 \quad (1.6)$$

However, the mean squared distance grows in proportion with the time elapsed:

$$\langle (\mathbf{r}_n - \mathbf{r}_0)^2 \rangle = t\tau \langle \mathbf{v}^2 \rangle \equiv 6D_0 t \quad (1.7)$$

where  $D_0$  is the diffusion constant. We can connect the equation to the equipartition theorem:

$$D_0 = \frac{1}{6} \langle \mathbf{v}^2 \rangle \tau = \frac{k_B T}{2m/\tau} \quad (1.8)$$

where  $k_B$  is the Boltzmann constant,  $T$  the temperature.

This relation is more typically rewritten in combinations with the findings of George Gabriel Stokes (1819-1903) [331], which introduced the frictional force, leading to the the Stokes-Einstein relation:

$$D_0 = \frac{k_B T}{\zeta} \quad (1.9)$$

where  $\zeta = 2m/\tau$  is the friction coefficient, proportional to viscosity.

### 1.2.6 Diffusion propagator

For long times, we can use the central limit theorem [84, 200, 282]: a sum of independent and identically distributed stochastic variables tends to be distributed according to the normal distribution when the  $n$  is large enough as long the distribution of the individual variables decays sufficiently fast.

The Einstein relation (1.7), which define the mean squared displacement, can also describe the variance of the spread of positions after a certain amount of time.

Hence, to define the probability of a particle being displaced from  $\mathbf{r}_0$  to  $\mathbf{r}$  in time  $t$  we use the Gaussian function.

For large  $t$  we have:

$$P(\mathbf{r}, t) = \frac{1}{(4\pi D_0 t)^{\frac{3}{2}}} e^{-\frac{(\mathbf{r}-\mathbf{r}_0)^2}{4D_0 t}} \quad (1.10)$$

where  $\sqrt{2D_0t}$  is known as the diffusion length. Einstein showed that the macroscopic movements are related to the thermal energy of molecules. The typical velocity can be estimated by the mean square velocity and the equipartition of the kinetic energy which says that the mean square velocity is proportional to the product of the temperature and the Boltzmann constant divided by the mass of the diffusing particles:

$$\langle v^2 \rangle = \frac{3k_B T}{m} \quad (1.11)$$

## 1.3 Diffusion MRI

### 1.3.1 Bloch and Bloch-Torrey equation

Earlier to the proposal of DW-MRI, in 1946, Felix Bloch (1905-1983), a Swiss-American physicist, proposed in a mathematical context the equation (1.12) [43] with the purpose of calculating the nuclear magnetization as a function of time when  $T_1$  and  $T_2$  relaxation [328] are applied:

$$\frac{d\mathbf{M}}{dt} = \gamma(\mathbf{M} \times \mathbf{B}_0) + \begin{pmatrix} -\frac{M_x}{T_2} \\ -\frac{M_y}{T_2} \\ \frac{M_0 - M_z}{T_1} \end{pmatrix} \quad (1.12)$$

The first term of the equation expresses the torque on the magnetic moments due to  $B_0$  [43], the second term adds the relaxation component of  $T_1$  and  $T_2$ .

In 1956, the equation was extended to be sensitive to diffusion, with the mathematical framework proposed by Henry Cutler Torrey (1911-1998). The framework incorporated the diffusion effects into the Bloch Equations 1.12, creating the so called Bloch-Torrey equation [339]. The equation assumes that the magnetization is proportional to the spin density.

$$\frac{d\mathbf{M}}{dt} = \gamma(\mathbf{M} \times \mathbf{B}_0) + \begin{pmatrix} -\frac{M_x}{T_2} \\ -\frac{M_y}{T_2} \\ \frac{M_0 - M_z}{T_1} \end{pmatrix} + D\nabla^2 \mathbf{M} \quad (1.13)$$

Compared to equation (1.12), the difference is the addition of the diffusion attenuation.

If we ignore the  $T_1$  and  $T_2$  effect, the solution of the Bloch-Torrey equation is:

$$\frac{d\mathbf{M}}{dt} = \gamma(\mathbf{M} \times \mathbf{B}_0) + D\nabla^2 \mathbf{M} \quad (1.14)$$

Since the image depend on the transverse magnetization, we can define the complex

number  $S = M_x + jM_y$ . Then the equation can be reduced to:

$$\frac{dS}{dt} = -j\gamma(G \cdot r)S + D\nabla^2 M \quad (1.15)$$

where  $r$  is the location, not the random position of the spin. Equation (1.14) can be solved as follows:

$$S = S_0 e^{\gamma^2 G^2 \delta^2 (\Delta - \frac{\delta}{3}) D} = S_0 e^{-bD} \quad (1.16)$$

### 1.3.2 Sensitizing the MRI signal to Diffusion

Parallel to the theoretical developments of diffusion in magnetic resonance, work on the hardware and sequence development to measure the phenomena was developing. Only a few years after the introduction of the Bloch equation (1.12), the principles of *spin echo* were noted by Erwin Hahn (1921-2016) in 1950 [148]. At the time, typical Nuclear Magnetic Resonance (NMR) experiments were performed with an initial 90-degree radio frequency (RF) pulse, to align the protons in the plane perpendicular to the main magnetic field. Then the Larmor precession occurs, and the spins start to precess around the main magnetic field. Spins that are initially coherent start to dephase due to dipolar interactions or magnetic field inhomogeneities, leading to a decay of the signal in the receiver.

However, further development was still needed to achieve a better understanding of the contrast acquired. Hahn introduced a 180-degree RF pulse, after the 90-degree degree RF pulse, to remove the inhomogeneities of the field and to reproduce the signal. Later, the technique was refined to be sensitive to diffusion. Herman Y. Carr (1924-2008) and Edwis Mills Purcell (1912-1997) in 1954 [58] introduced a constant gradient field to achieve sensitivity to diffusion. Using the advancements in the field mentioned above, in 1965 Edward O. Stejskal and John E. Tanner developed the widely used DW-MRI sequence, the Pulsed Gradient Spin Echo (PGSE) [330], see figure 1.4.

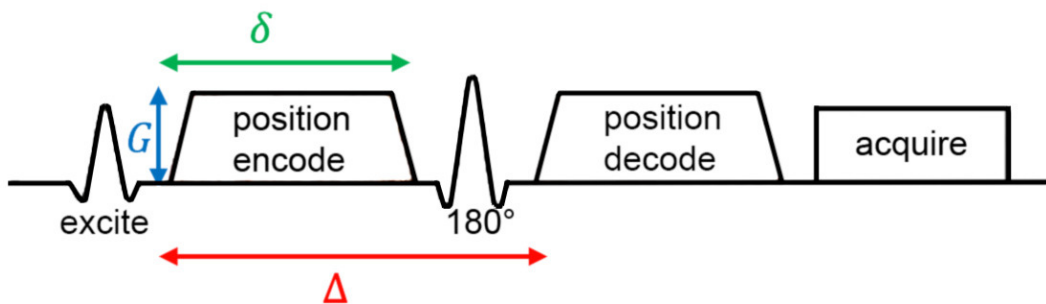


Figure 1.4 – Schematic representation of the Pulsed Gradient Spin Echo (PGSE) sequence.

The underlying principle of PGSE is the introduction of two gradient lobes, before and after the 180-degree pulse, which transmit a spatially-dependent phase to each spin. If the spins are not moving, the second gradient lobe will reverse the phase introduced by the first lobe

resulting in no net effect. However, the protons that experience random movement between the application of the two gradient pulses will experience a phase offset comparable to the degree of the displacements. The result will show a phase dispersion comparable to the spread of positions. The signal will be exponentially attenuated, after a time-echo (TE), according to the diffusion coefficient  $D$ , the  $\gamma$  gyromagnetic ratio, the amplitudes  $G$  and timing of the gradients,  $\delta$  and  $\Delta$ .

It is useful to define the so-called  $b$ -value [330] for a given sequence as:

$$b = \gamma^2 \int_0^{TE} \left( \int_0^t G(t') dt' \right)^2 dt \quad (1.17)$$

More specifically, we define a  $b$ -value of the PGSE sequence, including two diffusion gradients with duration  $\delta$ , separation  $\Delta$  and amplitude  $G$ .

$$b = (\gamma G \delta)^2 \left( \Delta - \frac{\delta}{3} \right) \quad (1.18)$$

### 1.3.3 Measuring the diffusion coefficient

The measured signal can be expressed as:

$$S = S_0 e^{-bD} \quad (1.19)$$

where  $S$ , the measured signal, has a decreased amplitude compared to the spin-echo signal  $S_0$  [330]. The greater the diffusion is, the more the measured signal  $S$  will be attenuated.

Because the methods are used to detect the signals of several processes together, and not only diffusion, e.g., phase dispersion due to susceptibility effects and bulk tissue motion from respiration or cardiac pulsations, we define the overall effect as an apparent diffusion, denoted as Apparent Diffusion Coefficient (ADC) [29]. The ADC along a given direction can thus be estimated by applying the diffusion gradients in said direction, and solving:

$$ADC = \frac{\ln \frac{S(b)}{S_0}}{-b}. \quad (1.20)$$

For free diffusion, the ADC is the same in any direction, and the ADC profile is said to be isotropic.

## 1.4 Microstructure Imaging

The microstructure imaging techniques aim at obtaining valuable information on the tissue microstructure properties utilizing the DW-MRI signal. To extract these microstructural

features we need the DW-MRI signal to be sensitive to specific features; hence, in the case of the simple PGSE sequence, we can vary the amplitude of  $G$ , the timing  $\delta$  and  $\Delta$  of the gradients, and the echo time (TE), to create a contrast in the signal. Ultimately, according to the previous sequence acquired, different approaches can be used for the reconstruction. One of the first microstructural imaging technique proposed was Diffusion Tensor Imaging, then more complex models were proposed to estimate axon diameter, axon density, and dispersion.

### 1.4.1 Diffusion Tensor Imaging

In free water, e.g., a glass of water, the diffusion is isotropic because movement in any direction, given a fixed magnitude of motion, is equally probable. However, in biological tissue, the self-diffusion of water molecules is hindered and restricted by membranes and macromolecules. In particular, in brain tissue, water can diffuse more freely along white matter fibers than across them.

This key concept was used by Basser et al. [28, 279] to define Diffusion Tensor Imaging (DTI).

From the DW-MRI data, fiber orientation in white matter can be estimated using a Gaussian propagator with the following equation:

$$\mathbf{D} = \begin{bmatrix} D_{xx} & D_{xy} & D_{xz} \\ D_{xy} & D_{yy} & D_{yz} \\ D_{xz} & D_{yz} & D_{zz} \end{bmatrix} = \begin{bmatrix} e_1 & e_2 & e_3 \end{bmatrix} \begin{bmatrix} \lambda_1 & 0 & 0 \\ 0 & \lambda_2 & 0 \\ 0 & 0 & \lambda_3 \end{bmatrix} \begin{bmatrix} e_1 \\ e_2 \\ e_3 \end{bmatrix} \quad (1.21)$$

The diffusion tensor is a positive definite, symmetric 3x3 matrix with eigenvectors  $e_1$ ,  $e_2$  and  $e_3$  and eigenvalues  $\lambda_1$ ,  $\lambda_2$  and  $\lambda_3$ . Eigenvectors represent the principal diffusion direction and the eigenvalues give the diffusivity along these directions.

Following the Gaussian assumption, the diffusion signal can be then expressed in terms of the diffusion tensor as:

$$S(b)_n = S_0 \exp(-b \hat{g}_n^T \mathbf{D} \hat{g}_n) \quad (1.22)$$

where  $\hat{g}$  represents the gradient direction. The equation has seven unknowns, six for the diffusion tensor  $\mathbf{D}$  and the  $S_0$ . The primary fiber orientation can be recovered using the eigenvector ( $e_1$ ) associated with the highest eigenvalue  $\lambda_1$ .

With DTI, it is possible to recover two well-known indices: the Fractional Anisotropy (FA) and the mean diffusivity (MD) [3].

$$FA = \sqrt{\frac{(\lambda_1 - \lambda_2)^2 + (\lambda_2 - \lambda_3)^2 + (\lambda_1 - \lambda_3)^2}{2(\lambda_1^2 + \lambda_2^2 + \lambda_3^2)}} \quad (1.23)$$

$$MD = \frac{\lambda_1 + \lambda_2 + \lambda_3}{3} \quad (1.24)$$

**Orientation Distribution Functions**

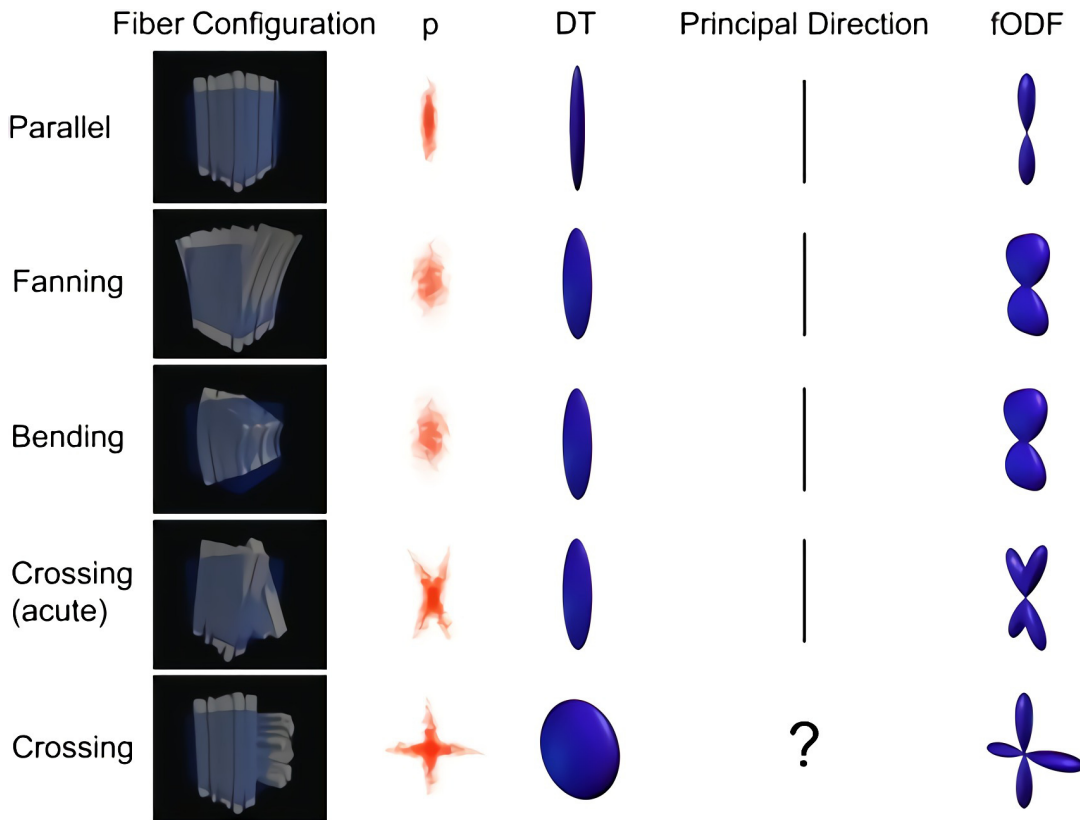


Figure 1.5 – Column one shows configurations of fibers that arise often in voxels (first column). Column two shows the diffusion pattern expected. The third column shows the Diffusion Tensor Imaging (DTI) fitting. The fourth column shows the principal direction of the DTI. In the last row, the DT is perfectly oblate so the principal direction is undefined. The fifth shows the Fiber Orientation Distribution (FOD) function. *The illustration is modified from [315].*

DTI is a very useful technique when we want to estimate anisotropy of diffusion. However, taking into account the resolution at which DW-MRI operate, we are very likely to find in a voxel multiple populations with different geometry: parallel, fanning, bending and crossing [182].

In order to tackle the problem of complex orientation inside a voxel, several approaches have been proposed: multi-tensor models [34, 346], Diffusion Spectrum Imaging (DSI) [345, 361], *pasmri* [167], Spherical Deconvolution (SD) [8, 92, 93, 343]. In this thesis, we will focus on the SD [8, 343] because it is a technique that we will use in the next chapter of the thesis, and it is widely used nowadays. With SD, we will try to recover multiple fiber orientations. See Jbabdi and Johansen-Berg [168] for a more complete view on the crossing fiber problems.



To find multiple orientations for fibers with the SD [343] technique, the diffusion signal can be rewritten as:

$$S(\theta, \phi) = fODF(\theta, \phi) \otimes R(\theta) \quad (1.25)$$

where  $R(\theta)$  is the unit sphere of a response function (kernel), representing the signal of a single-fiber bundle, and  $fODF(\theta, \phi)$  is a Fiber Orientation Distribution (FOD). The diffusion signal  $S(\theta, \phi)$  is seen as the convolution between  $fODF(\theta, \phi)$  and  $R(\theta)$ . In equation 1.25, only  $S(\theta, \phi)$  is known. Initially, a step is performed to estimate the response function  $R(\theta)$  using the algorithm proposed by Tournier et al.[342]. The estimation is performed in voxels where diffusion tensor analysis showed high anisotropy, i.e., an approximation of single fiber voxels. Subsequently, the DW-MRI signal is deconvolved using spherical harmonics [340] in order to obtain multiple orientations per voxel, i.e., fiber orientation density function.

### 1.4.2 Signal models

After the initial applications of DW-MRI, the number of studies in modeling the diffusion signal increased radically. We can divide the approaches used in two fields: signal models and biophysical models. Signal models aim to describe the signal through a continuous function, while biophysical models aim to relate the signal to intrinsic biological properties of the tissue.

Typical signal models are the previously introduced DTI, higher order tensor [219, 265], spherical harmonics ADC profile [7, 131], Diffusion Kurtosis Imaging (DKI) and cumulant expansion [173], SHORE [263], Mean Apparent Propagator (MAP-MRI) [264], anomalous diffusion [37, 262] and Intravoxel Incoherent Motion (IVIM) [205]. This last may be considered more biophysical model compared to previously cited.

### 1.4.3 Biophysical models

Generally, biophysical models are associated with compartment models. In the compartment models, the "stick" was proposed first [33, 34, 329]. Then studies of axon diameters estimation with AxCaliber [14, 25] and ActiveAx [5, 104]. In the same period, estimation of fiber dispersion was proposed [15, 171, 323, 371] and technique that refine the signal neglecting dispersion were proposed with the Spherical Mean Technique (SMT) [189, 190].

The typical compartment model of the WM assumes the separation of intra-axonal signal, the signal from water molecules trapped inside the axons,  $S_i$  and extra-axonal signal  $S_e$  [4], whose signal is derived from the water molecules moving in the space between axons. The WM can then be described as:

$$S = f_i S_i + f_e S_e \quad (1.26)$$

## Chapter 1. Background

---

where  $f_i$  and  $f_e$  represent respectively the signal fraction of intra-axonal and extra-axonal compartments, and  $f_i + f_e = 1$ . Compartment models may also include free diffusion water which is typically modeled as a sphere.

In the following sections, we will present the most used compartment models which we will also use in the following chapter of the thesis.

### CHARMED

The Composite Hindered And Restricted Model of Diffusion (CHARMED) was proposed by Assaf et al. [15] to model hindered and restricted water diffusion. The model proposes a mixture of  $M$  hindered and  $N$  restricted compartments:

$$S(q, \Delta) = \sum_{j=1}^M f_i^j S_i^j(q, \Delta) + \sum_{k=1}^N f_e^k S_e^k(q, \Delta) \quad (1.27)$$

Where  $f_i^j$   $f_e^j$  are the signal fractions of the restricted and hindered compartments,  $S_i^j(q, \Delta)$  is the signal given by a cylinder of radius  $r$  as derived by Neuman [248], and the extra-axonal compartment is modeled with a tensor. The  $q$ -value is equal to  $q = \frac{1}{2\pi} \gamma \delta G$ . Since the model includes several restricted compartments, it is possible to model fiber dispersion.

### AxCaliber

After CHARMED, Assaf et al. [14] proposed a second model, named AxCaliber, to estimate the axon diameter distribution. The assumption that the model uses is that the WM voxel model contains only single populations voxels and the diffusion signal is represented as following:

$$S(q, \Delta) = f_i S_i(q, \Delta) + f_e S_e(q, \Delta) \quad (1.28)$$

Similarly to CHARMED, the extra-axonal signal is modeled with a tensor, and the intra-axonal signal is modeled as a set of parallel cylinders with radii sampled from a gamma distribution. A significant limitation of the method is that the AxCaliber model assumes diffusion gradients to be applied perpendicularly to the axons. Non-linear Least Square (NLS) is used to estimate the signal fractions, the perpendicular diffusivity, and the parameters  $\alpha$  and  $\beta$  of the gamma distribution.

### ActiveAx

In 2010, Alexander et al. proposed ActiveAx [5] where the aim was to simplify previous models and estimate the mean axon diameter or Axonal Diameter Index (ADI). The WM tissue model used is the Minimal Model for White Matter Diffusion (MMWMD) and uses parallel cylinders

for the intra-axonal signal and tensors for the extra-axonal signal. To reduce the degree of freedom in the extra-axonal signal the tortuosity model [332] was used. The model estimates the ADI and the signal fractions, which are estimated using a non-linear optimization with a Markov Chain Monte Carlo (MCMC) procedure.

### **NODDI**

Probably one of the most popular models proposed in the last decade is Neurite Orientation Dispersion and Density Imaging (NODDI) [371]. Instead of modeling the axon diameter with a cylinder, with this approach we model the orientation dispersion with a set of "sticks", i.e., cylinders with radius 0. Similarly to previous mentioned methods the extra-axonal signal is modeled with a tensor. The final parameter estimated by the model is signal fraction and degree of dispersion. These parameters are estimated using a Gauss-Newton non-linear optimization.

Compared to the previous three methods mentioned, NODDI gained much more popularity, mainly because the model was suitable to be used in clinical scanners.

## **1.5 Tractography**

The overall goal of tractography is to reconstruct WM connections. Using the local estimation of orientation, which can be performed using methods cited in the previous section, the goal of tractography is to piece together these orientations to show the underlying 3 dimensional (3D) trajectory of the bundles. Furthermore, tractography is also the only tool that allow us to reconstruct the 3D WM in the living brain.

Several tractography algorithms were proposed during the years. The two main categories that we present in this thesis are: local and global approaches. The main differences between the two are that the local approach creates streamlines independently, one after the other, while the global approach builds streamlines all simultaneously.

### **1.5.1 Local approach**

Local tractography is any method that takes local decisions: starting points, end points, what is the next step.

All the first introduced tractography methods used local approaches. The first local tractography method proposed was in 1992 with the hyperstreamlines [89], however, did not get much popularity, probably due to its complexity. It is easier to relate the proposal of tractography as it is known today with the studies performed around 1998 when several methods were proposed [27, 66, 238, 362, 363].

Among all the first methods proposed, we introduce the Fiber Assignment by Continuous

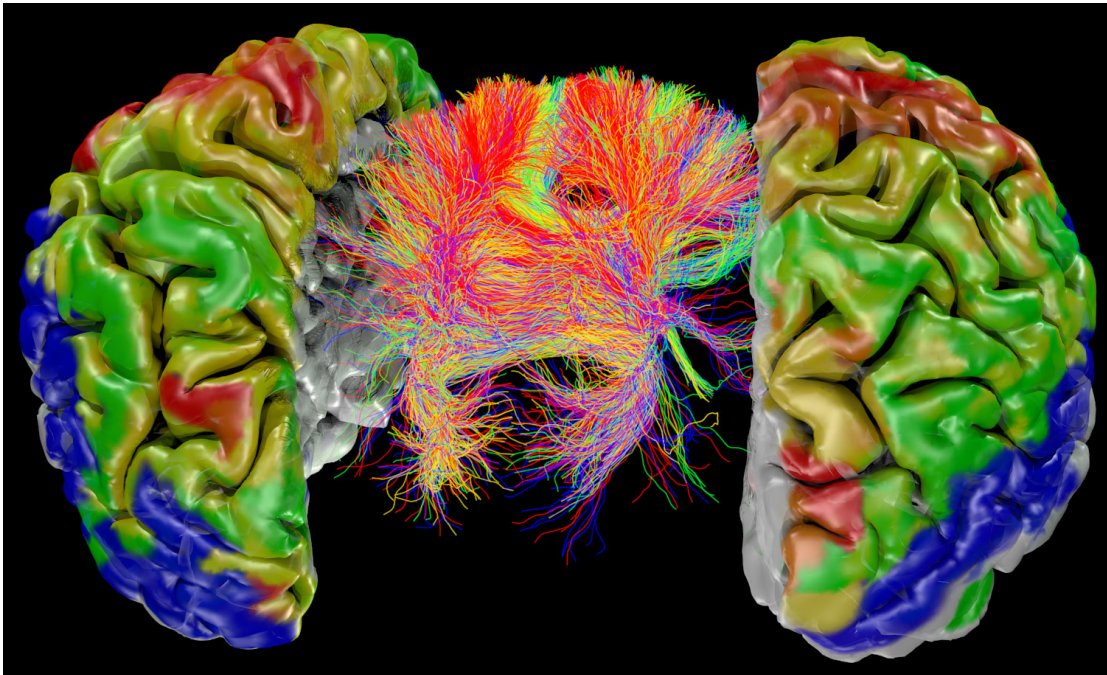


Figure 1.6 – Illustration of tractography. The goal of tractography is to reconstruct the White Matter (WM) bundles of the brain. In this illustration, we show streamlines of the Corpus Callosum (CC) connecting the left and right hemisphere of the brain. Streamlines can be colored according to a tissue property. Endpoints of the streamlines can be projected onto the cortex.

Tracking (FACT) [238]. This algorithm refers at the class of the streamline method which is the most direct method for performing tractography as it can be reconstructed by only starting at a seed point and following the local vector information. The FACT approach shows that it is possible to track the 3D structure of fiber pathways by using the main direction of the voxel diffusion profile and setting three principal parameters: step size, angular constraint, and interpolation.

In terms of usage of local tractography, through the years it became famous thanks to the simplicity of the method and the fast computation time. Local tractography proposed many methods [31] and models; see [178] for a review of tractography algorithms. At the very high level, there are deterministic methods where we find one trajectory per seed point, the location where tractography is initiated, and probabilistic methods [34] which try to explore the space of possible pathways exploring uncertainty in the diffusion orientation.

### **Start and stop criteria**

One of the main local decision to take is the start and the stop criteria. Here we have two main categories: threshold-based and rule-based. The threshold based criteria [223, 238, 269, 286, 310, 341] can be related to: FA, FOD density, bundle-specific, curvature angle between

steps, free-water corrected. The rule-based are related to: seed mask, brain mask, anatomical constraint [34, 106, 135, 139]

### Data interpolation

Other important criteria to choose are the interpolation, which can be: local, less local and with "memory". The first methods proposed were all local: nearest voxel, random voxel, trilinear interpolation, spline interpolation. [26, 34, 238]. For the less local: Runge-Kutta or midpoint method [333] where half of the step is taken, the data is interpolated, and then that info is averaged with the data at the starting point. For the "memory" cases, data from previous steps are used [117, 203, 203, 223, 362, 363].

### Deterministic vs probabilistic propagation

Another important point to highlight is how to take the next step: deterministic or probabilistic. The deterministic algorithm follows the major eigenvector (principal diffusion direction) of the tensor or the maximum peak from an Orientation Diffusion Function (ODF) [93, 168, 238]. Probabilistic generally samples from some local distribution and sometimes they may have priors that may prefer a previous orientation of tracking [34, 132].

### Benefits and limitations

The major benefits of tractography are several and here we report few examples. Firstly, the algorithms are widely available and freely provided by different softwares [135, 341]. Then, tractography is practically helpful, since it can be used to reconstruct in vivo the major bundles known from anatomy [19, 106, 201]. Hence, up to a certain extent, is used in neurosurgery [251]. Ultimately, it has been shown consistency across subjects also in patients with brain tumors [256].

Limitations of tractography include anatomical error such as false positive and false negative connections [196, 221, 307, 319, 335]. More specifically, there is a known bias towards certain type of connections [139, 168, 257, 291], i.e., it is more difficult to track the long-range connections. The fundamental limitation is the resolution, where DW-MRI is in the order of  $mm$ , and the axon diameter is in the order of  $\mu m$ . Nevertheless, validation is also one of the main issues; and when this is put in the context of software availability, it is difficult to evaluate performance due to different Region of Interest (ROI) or software programs [47, 117, 283, 356]. Tractography is improving; however, more research is needed, with better resolution, better algorithms, and better models. Alternatively, as proposed by [335] which have a more pessimistic view, tractography may not be solved based with DW-MRI alone.

Deterministic limitations: the main limitation of the technique is that MRI can only give information on the average axonal orientation within a voxel and the resolution does not allow

distinguishing among several small projections that are immediately adjacent to each other. In conclusion, streamline deterministic algorithms tend to be fast and straightforward but suffer from the propagation of local estimation imprecisions along the path.

**Probabilistic limitations:** Probabilistic tractography techniques can generate streamlines through regions of high uncertainty, where deterministic techniques would stop. Often, several hundred streamlines are generated from each, and the most likely fiber pathways are extracted from the results. However, probabilistic algorithms are more difficult to interpret, and the probability maps generated may not be trivial; hence, they only partially solve the central issues of the local formulations.

### 1.5.2 Global approach

Global minimization approaches have been proposed [126, 197, 288] to reconstruct at once the full tractography over the whole brain. Global tractography concurrently reconstruct all the fiber tracts by finding a solution that best explain the measured diffusion data. In particular, it showed high stability in the presence of imaging artifacts and noise in the data as presented in the work [216]. However, due to the complexity of the problem, a complete global algorithm that recovers biological features needs still to be formulated. Nevertheless these limitations, these methods outperform local methods, at the cost of an increased computational burden, e.g., one week per brain, which is not suitable for some clinical applications.

In the list of the global methods we cite Spin Glass model [126], Gibbs Tracker [197, 288], extension to microstructure [287, 316] and multishell data [63], simulated annealing [212], and global reconstruction FODs [288]. The basic idea is that there is a fiber model where there is a segment which can be associated to spin glasses which are distributed all over the brain and they not fixed to voxels, and they can make connections. Each of the segment can contribute to a signal. The goal is to find the best configuration of these spins that best explain the observed data. Usually, algorithms are probabilistic in nature; however, there is no idea of how many spins should be there and usually to make the fitting practical, the use of simulated annealing with decreasing temperature [288] is performed. Segments also carry variable diffusion parameters like signal fractions and diffusivities [63, 287]. Each segment has a set of parameters: position, orientation intra-axonal diffusivity.

**Limitations:** hard non-parametric optimization problem, millions of connections, the interaction of segments is often limited and each transition requires computation of energy difference. They are slow and not efficient. Generally, it is not possible to guarantee GM connectivity [319]. However, the main advantage is that they can be used to predict the DW image data.

### 1.6 Microstructure Informed Tractography

Initially, tractography and tissue microstructure estimation have been studied as two separate problems. Nevertheless, recent studies [76, 77, 138, 297, 316, 317, 367] have demonstrated the potential benefits of combining local microstructural features and tractography. These last methods use broad set of candidate streamlines using different tractography algorithms, followed by an extraction of a subset that best fits the acquired DW-MRI signal. This technique tackles the problem in a top-down approach, whereas bottom-up strategies characterized all previous tractography approaches.

#### 1.6.1 Non linear methods

In Sherbondy et. al.[316], a supercomputer was used to find a optimal subset of fiber tracts from a huge set of candidates. However, the use of a supercomputer limited the use for real applications. Lately, the framework was optimized in MicroTrack [317] with the addition of multicompartment model similar to Alexander et. al.[5]. MicroTrack was the first algorithm that assumed that the microstructural properties of the fibers remain constant along their trajectory. The algorithm was used successfully showing the advantages of combining microstructure and tractography. However, similar to previous global methods, the approach suffered for two main limitations: first, the complexity of the formulation did not guarantee to converge to the optimal solution, second, increased computational burden.

Other methods similar in spirit to MicroTrack have been proposed more recently. In [297], a variation of the method with the introduction of a particle filter mechanism was proposed. The method included axon dispersion using NODDI [371], during propagation of the streamlines. Another example is the split-and-merge tractography [367] which proposed to split the fibers at inaccurate locations according to an accuracy measure and produces clusters of short tracts as output. One more example that was used more often by the community is the spherical-deconvolution informed filtering of tractography (SIFT) method [320], which uses the fiber orientation distribution reconstructed with constrained spherical deconvolution to select which candidates have to be removed. Despite showing good results, these simplified methods do not use multiple b-values acquisitions and proper tissue models which are required to be sensitive to tissue microstructure.

#### 1.6.2 Linear methods

To overcome previous limitations, the Convex Optimization Modeling Microstructure Informed Tractography (COMMIT) [76, 77] framework has been proposed, see figure 1.7. COMMIT reformulates tractography in the framework of convex optimization, reducing the computational cost to accommodate real application demands and guaranteeing recovery of the optimal global solution. The approach is close in spirit to MicroTrack[317], for both use multicompartment models and global optimization techniques to combine tractography with

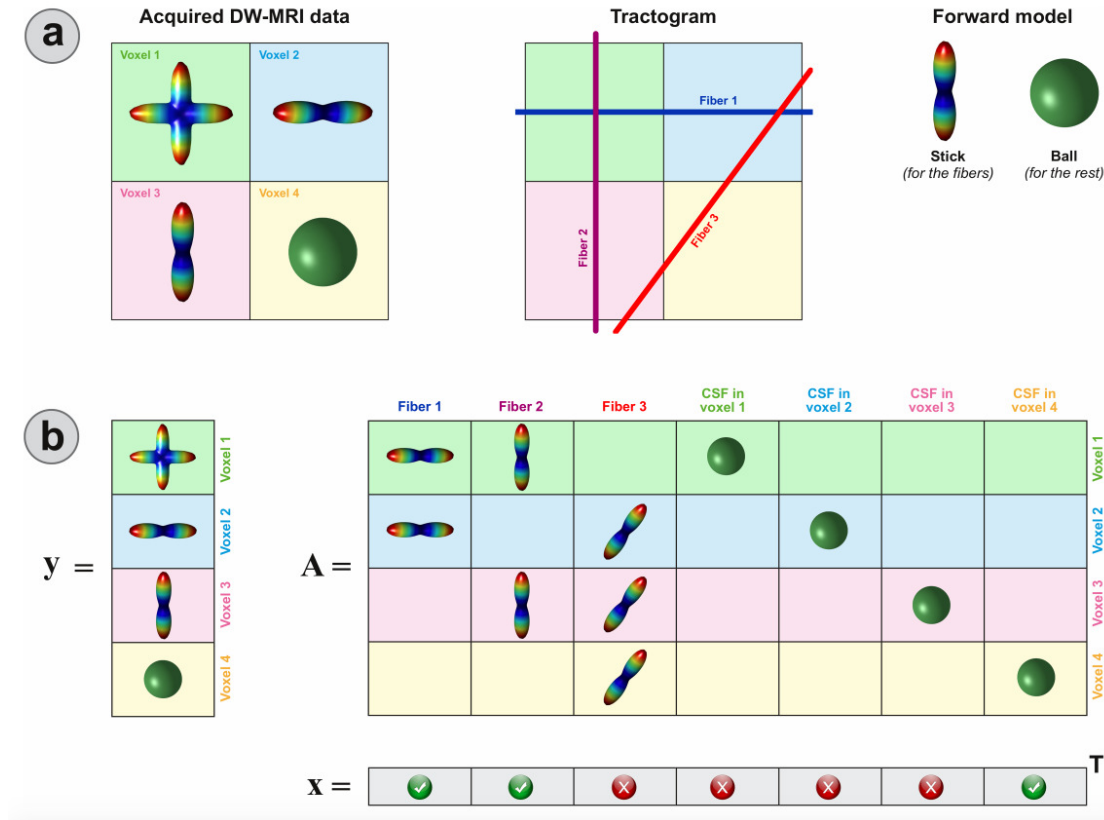


Figure 1.7 – Example to illustrate the modeling of the Convex Optimization Modeling Microstructure Informed Tractography (COMMIT) framework. (a) The simulated Diffusion-Weighted Magnetic Resonance Imaging (DW-MRI) data, a tractography and a forward-model used to associate a signal contribution to each streamline. (b) The corresponding vector  $y$  of DW-MRI measurements, the matrix  $A$  encoding the signal contributions according to the forward-model of each streamline and the coefficients  $x$  estimated by COMMIT. *The illustration is reproduced from [302].*

microstructure tissue parameters.

Although DW-MRI provides quantitative data, tractography is known to be a non-quantitative technique [184, 185, 221, 307, 335]; COMMIT tries to overcome this limitation by assigning a biophysical model [268] to each reconstructed streamline and expressing the whole DW images as a linear combination of the signal's contribution arising from all the streamlines:

$$\mathbf{y} = \mathbf{A}\mathbf{x} + \eta, \quad (1.29)$$

where  $\mathbf{y}$  contains the DW-MRI measurements for all voxels of the brain,  $\mathbf{A}$  is a matrix that accounts for the signal contributions of the streamlines in each voxel (possibly in addition to local voxel-wise contributions tissue compartments, e.g. cerebrospinal fluid) according to any given multi-compartment model [268] and  $\eta$  is the acquisition noise. The unknown



contributions  $\mathbf{x}$  of all the compartments can then be efficiently estimated by solving a non-negative least-squares problem:

$$\operatorname{argmin}_{\mathbf{x} \geq 0} \|\mathbf{A}\mathbf{x} - \mathbf{y}\|_2^2. \quad (1.30)$$

Similarly to previous methods proposed [276, 316, 317, 320, 321], COMMIT enforces the estimated parameter to be constant along the trajectory of the streamlines.

## 1.7 Thesis in a nutshell

The goal of this thesis is combining microstructure imaging and tractography to estimate more robust microstructure parameters. Different approaches have been proposed during the years, but only in 2015, the combination was formulated in a convex fashion, allowing fast computation and exploration of modeling.

In this thesis, we contributed to highlighting standard tractography methods. Furthermore, we proposed a pilot study to use a 3D histological method, named CLARITY 3D, to validate diffusion tractography. However, the real contributions of this thesis lie on the new paradigm proposed for modeling brain data. We will use microstructure informed tractography to disentangle  $T_2$  contributions of different bundles. Furthermore, the second main contribution is related to study the feasibility to achieve axon diameter distributions. Even if the new formulation of microstructure informed tractography is faster when the model becomes complex, the computational time increase. In the appendix, we propose a preliminary study which uses a neural network to recover microstructure informed tractography scalar maps and reduce the computational time from hours to seconds.



## 2 International tractography challenges

The increasing interest in the human brain connectivity has heightened tractography as the modeling technique of choice. Although significant research has been devoted applying and developing tractography algorithms [21, 26, 33, 39, 49, 61, 65, 68, 87, 141, 151, 168, 178, 180, 181, 186, 202, 203, 207, 208, 213, 225, 239, 241–243, 254, 258, 283, 284, 322, 337, 349, 356, 360, 365, 372], rather more limited attention has been spent on proper validation and reproducibility. To learn weaknesses and to test the algorithms that emerged during these last years, we competed in 3 international tractography challenges in the period of 2015 to 2018. In this chapter, we aim to present these challenges, report the final findings and give perspective on what are the principal limitations, and what are the next steps that need to be implemented to obtain more reproducibility and specificity to tractography among, primarily, the neuroscience community, and then other communities.

Of the three challenges, two were organized during the International Society for Magnetic Resonance in Medicine (ISMRM) conference [221, 246], respectively named, the 2015 "tractography" challenge and the 2017 "tractography-reproducibility with empirical data" challenge. The last challenge was organized during the the Institute of Electrical and Electronics Engineers (IEEE) International Symposium on Biomedical Imaging (ISBI) [307] in 2018, named "3-D validation of tractography with experimental MRI".

The three challenges are related to three different problems. In the first section of this chapter, we will focus on the ISMRM 2015 challenge based on numerical simulations. In the second, we will tackle the problem of reproducibility using *in vivo* DW-MRI acquisition. Ultimately, we will focus on tractography validation using physical phantoms and *ex vivo* monkey acquisitions.

### 2.1 ISMRM 2015 Tractography

The ISMRM 2015 tractography challenge is based on synthetic data which gives the advantage of knowing the ground truth. Hence, it is possible to evaluate the performance of tractography

algorithms more accurately.

The next sections will present the dataset and the methodology proposed by several groups. In the end, final comments and perspective works will be reported.

### 2.1.1 Dataset and evaluation

Shortly, the dataset proposed in the work of Maier-Hein et al. [221] is the following: numerical phantoms that use tractography's fiber geometry as ground truth for DW-MRI signal generation.

Comparable approaches have been proposed in earlier studies [68, 125]. The originality of the ISMRM 2015 tractography challenge lies in two aspects: the use of high-quality HCP data[140] to generate realistic fiber bundles geometries and the manual segmentation by an expert radiologist of 25 major fiber bundles. The bundles, (figure 2.1), were determined according to knowledge taken from past electrophysiological and anatomical literature[61].

Ultimately, the DW-MRI signal was generated using a clinical acquisition protocol, generating a brain-like numerical phantom.

To quantitatively evaluate the tractography results submitted by the various groups, the Tractometer connectivity metrics [68] were used. We do not enter in detail of all the metrics used, however, we report briefly the main used: the true positive, defined as Valid Connections ratio (VC) (portion of valid streamlines) and the Valid Bundles (VB) (number of valid bundles) metrics; false positive, with the Invalid Connections ratio (IC) (portion of invalid streamlines) and the Invalid Bundles (IB) (number of invalid bundles) metrics; volume reconstruction, with the Volumetric OverLap (VOL) and the Volumetric OverReach (VOR) metrics. The VOL describe the part of the voxels inside the volume of a ground truth bundle that is crossed by at least one valid streamline; the VOR is the portion of voxels outside the volume of a ground truth bundle that is traversed by at least a streamline associated with the bundles' volume. Notice that few abbreviations from the original article [221] are changed for the reason of dissertation consistency.

### 2.1.2 Results

#### **Most of the ground truth bundles are recovered**

A positive message that came out is that most of the state of art algorithms obtained 90% of the Ground Truth (GT) bundles, considering binary criteria of the ROIs; hence, considering if a connection between two regions exist if at least one streamline connects two ROIs.

However, the volumetric reconstruction shows that accuracy in reconstructing the volume of the bundles varies greatly from different bundles and algorithms. Figure 2.2a shows the analysis performed; identifying VB can be grouped into three clusters of "very hard",

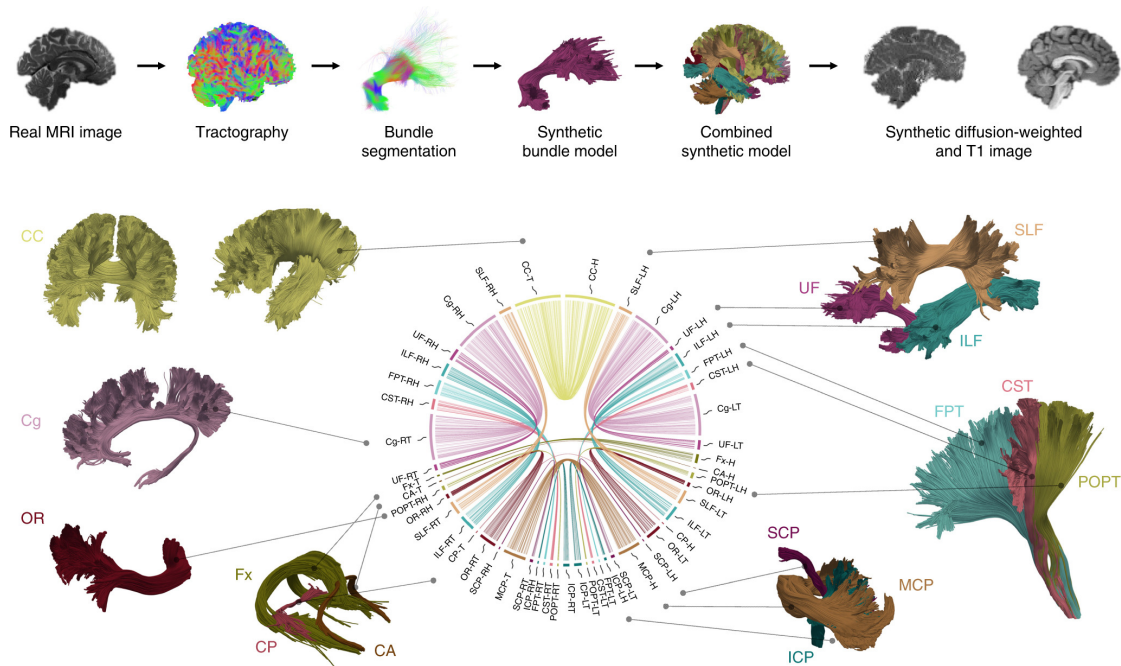


Figure 2.1 – Top, row summarizes the overview of the numerical phantom generation. Bottom, 25 manually cleaned bundles by an expert radiologist; the bundles were segmented from a HCP data set whole-brain tractography. The bundles included in the study are the following: the CorticoSpinal Tract (CST), the Corpus Callosum (CC), Cingulum (CG), Optic Radiation (OR), Uncinate Fasciculus (UF), Superior Longitudinal Fasciculus (SLF), Inferior Longitudinal Fasciculus (ILF), Arcuate Fasciculus (AF), Posterior Commissure, Inferior Cerebellar Peduncle (ICP), Parieto-Occipital Pontine Tract (POPT), Superior Cerebellar Peduncle (SCP) and Fronto Pontine Tracts (FPT). In the middle is shown the connectivity plot of the phantom design. Reprinted from [221], Copyright 2017, with permission from Springer Nature.

"hard", and "medium difficulty", corresponding to the percentage of VOL. Figure 2.2b presents corresponding examples that were reconstructed by different tractography techniques.

The smallest tracts were challenging to reconstruct, that is, the Posterior Commissure (PC) and Anterior Commissure (AC) have a thickness lower than 2 mm; these were labeled as 'very hard'. Bundles of medium difficulty were the UF, the Superior Longitudinal Fasciculus (SLF), Inferior longitudinal fasciculus (ILF) and the CC with an mean of more than 50% volumetric recovery. Furthermore, the Pearson product-moment correlation coefficient [1] was calculated. The results ( $r=0.88$ ,  $p < 10^{-8}$ ), indicated that the probability of reconstructing a greater part of a bundle VOL is directly linked to generating false trajectories VOR.

**More invalid than valid bundles**

The negative message that came out from the challenge is that on the set-up used for this study, on average tractography contained four times more IB than VB. This result shows that

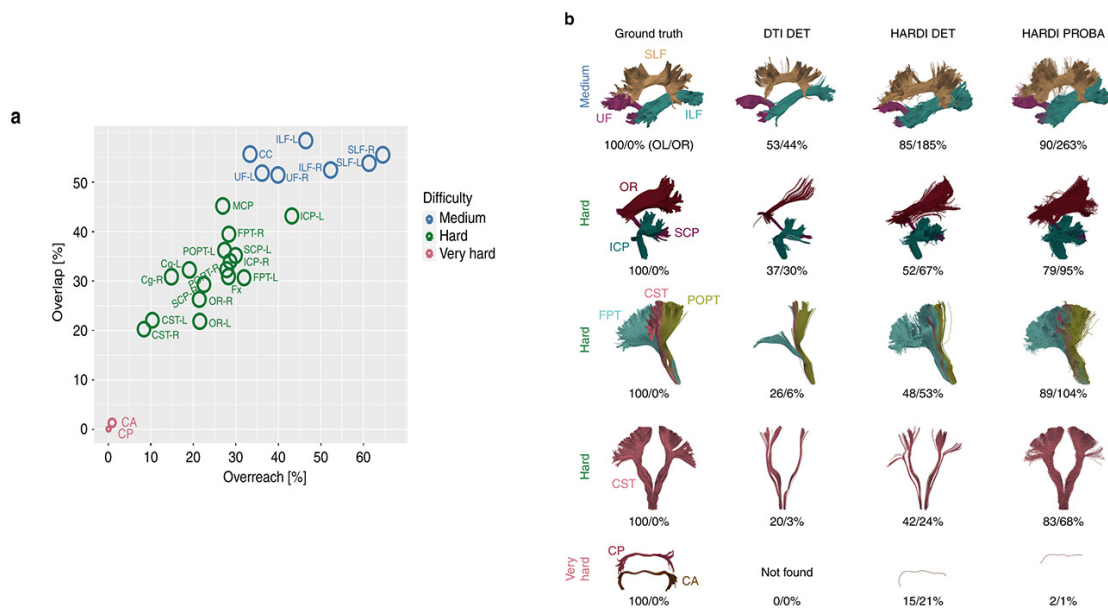


Figure 2.2 – All the ground truth bundles are identified with the method proposed, however, the ratio of streamlines and their volume was not recovered correctly. (a) Averaged Volumetric OverLap (VOL) and the Volumetric OverReach (VOR) values of the submissions for the 25 bundles from the ground truth. Colors: blue - medium; green - hard; red - very hard. (b) Example of bundles for Diffusion Tensor Imaging (DTI) deterministic, High-Angular Resolution Diffusion Imaging (HARDI) deterministic, and HARDI probabilistic. The first column shows ground truth bundles. Volumetric OverLap (VOL) and Volumetric OverReach (VOR) scores are reported. *Reprinted from [221], Copyright 2017, with permission from Springer Nature.*

tractography has still work to accomplish in order to diminish this problem. Moreover, more research is needed to tackle the IB connections [302].

There are bundles which existence have been debatable: the middle longitudinal fasciculus (MdLF) [222], the Superior fronto-occipital fasciculus (SFOF) [129, 232], the Inferior Frontal Occipital Fasciculus (IFOF) [129], the Arcuate Fasciculus (AF) [86] and the Frontal Aslant Tract (FAT) [60]. All these bundles were not integrated into the numerical phantom; however, most of the tractography algorithms found them. These results do not prove that these bundles does not exist. Moreover, the anatomical knowledge of these bundles should be studied more in details. Perhaps, using complementary information with electro physiological and anatomical studies.

### 2.1.3 Discussion

An international tractography competition ([tractometer.org/ismrm\\_2015\\_challenge](http://tractometer.org/ismrm_2015_challenge)) was organized to test tractography algorithms. Numerical simulations of DW-MRI with geometry that simulate known anatomical bundles were used and results of reconstruction were analyzed quantitatively with the Tractometer connectivity metrics [68]. The final results show a funda-

## 2.2. ISMRM 2017: Tractography-reproducibility with Empirical Data

---

mental ambiguities tractography when based only on orientation information. The challenge highlighted that innovative technological and conceptual developments are necessary in order to achieve and solve tractography uncertainties.

### **Methodological innovation**

The initial challenge provided only the DW-MRI. After the conclusion of the challenge, the authors extended the data reducing the complexity of the problem and adding the GT field of orientation. However, even with the GT field of orientation, the tractography results did not improve the bundles's reconstructions significantly. Hence, not only the DW-MRI may not support a correct reconstruction, but even the local modeling may not be enough because it creates ambiguities when used for tractography; at least for the resolution used in the study.

The fundamental problem reported is the presence of "bottlenecks." Maier-Hein et al. [221] report a specific case in the temporal lobe, where multiple bundles overlap and tractography clearly show his limitation. These "bottlenecks" are one of the main reason for the existence of IB connections. The authors propose to use of additional information which could guide better streamlines in the local orientation fields estimated from DW-MRI.

### **Personal considerations**

The positive message that emerges from the ISMRM 2015 challenge is that a consensus of tractography main limitations has been listed. Thanks to these findings, it is now possible to re-direct the attention of the Diffusion MRI community to specific problems and try to achieve better tractography methods.

However, particular attention has to be given to how the dataset was constructed. More specifically, it is essential to highlight that a specific DW-MRI protocol was chosen; we suggest that perhaps different protocol could perform better in terms of tractography reconstruction. For example, as mention in the paper, biophysical modeling, which need more advanced DW-MRI protocols, may help to reduce the ambiguities in tractography, see chapters 4 and 5.

In conclusion, we highlight that it is vital that the limitations of the standard clinical protocol have been highlighted. However, more work is needed to generalize these findings to all the tractography field.

## **2.2 ISMRM 2017: Tractography-reproducibility with Empirical Data**

In the previous section 2.1 validation with numerical simulations was proposed to assess the anatomical preciseness of tractography. In this section, we present an analysis performed on in vivo data, intending to evaluate the level of reproducibility in tractography.

Reproducibility is not directly linked to the validity of the reconstructed WM bundles in the

## Chapter 2. International tractography challenges

brain; however, it is a necessary step to create a tool that can be used in clinical applications.

Similarly as in section 2.1, in this study a standard clinically DW-MRI protocol was used. Nine groups participated to the challenge and had to submit a tractography in the format of the Track Density Imaging (TDI) [51] scalar map for the following bundles : UF, Fornix (Fx), genu and splenium of the CC, Cingulum (Cg), Cortico-Spinal Tract (CST), ILF, SLF, and IFOF. Bundles submitted are shown in figure 2.3.

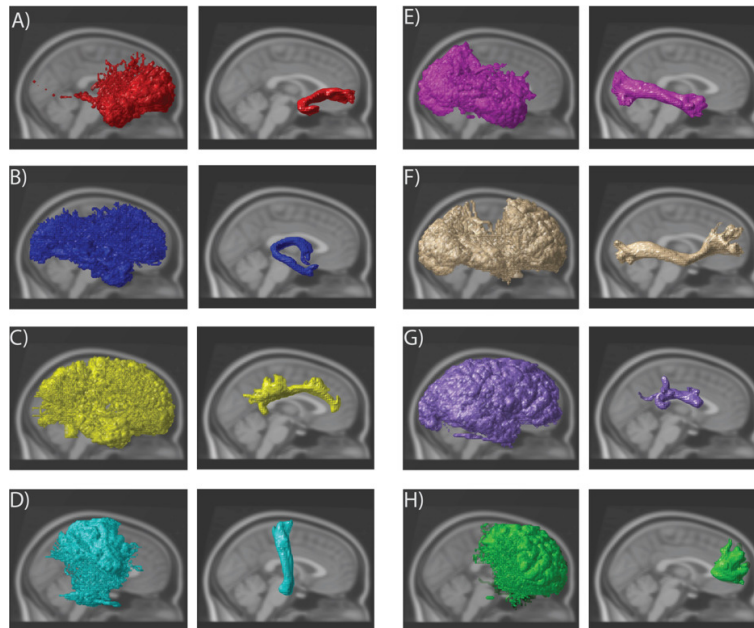


Figure 2.3 – Left side shows the overlay of all the submissions from all sessions. On the right an example of a a single submission. More information of the name of the bundles can be found in the original manuscript [246]. *Reprinted from [246], Copyright 2019, with permission from International Society for Magnetic Resonance in Medicine.*

### 2.2.1 Dataset and evaluation

A multi-shell High-Angular Resolution Diffusion Imaging (HARDI) sequence on single healthy human subject was used for the DW-MRI protocol. Two different Philips scanners were used to test the reproducibility inter-scanner. Five acquisitions in two separate session on the two different scanners were collected with the following protocol: b-value  $1000 \text{ s mm}^{-2}$ ,  $2000 \text{ s mm}^{-2}$  and  $3000 \text{ s mm}^{-2}$  with 20, 48 and 64 uniformly distributed gradient directions respectively were acquired. Other parameters used were:  $\Delta = 48 \text{ ms}$ ,  $\delta = 37 \text{ ms}$ , Echo Time (TE) =  $99 \text{ ms}$ , Repetition Time (TR) =  $2920 \text{ ms}$  and voxel resolution =  $2.5 \text{ mm}$  isotropic.

The following metrics were used for comparison: Intra Class Correlation (ICC) statistics for continuous values and Dice similarity scores [97] with inter-scanner, inter-session, and intra-session metrics. A violin plot, see figure 2.4, was generated using a combinations of pairs of repeats of the two metrics.



## 2.2. ISMRM 2017: Tractography-reproducibility with Empirical Data

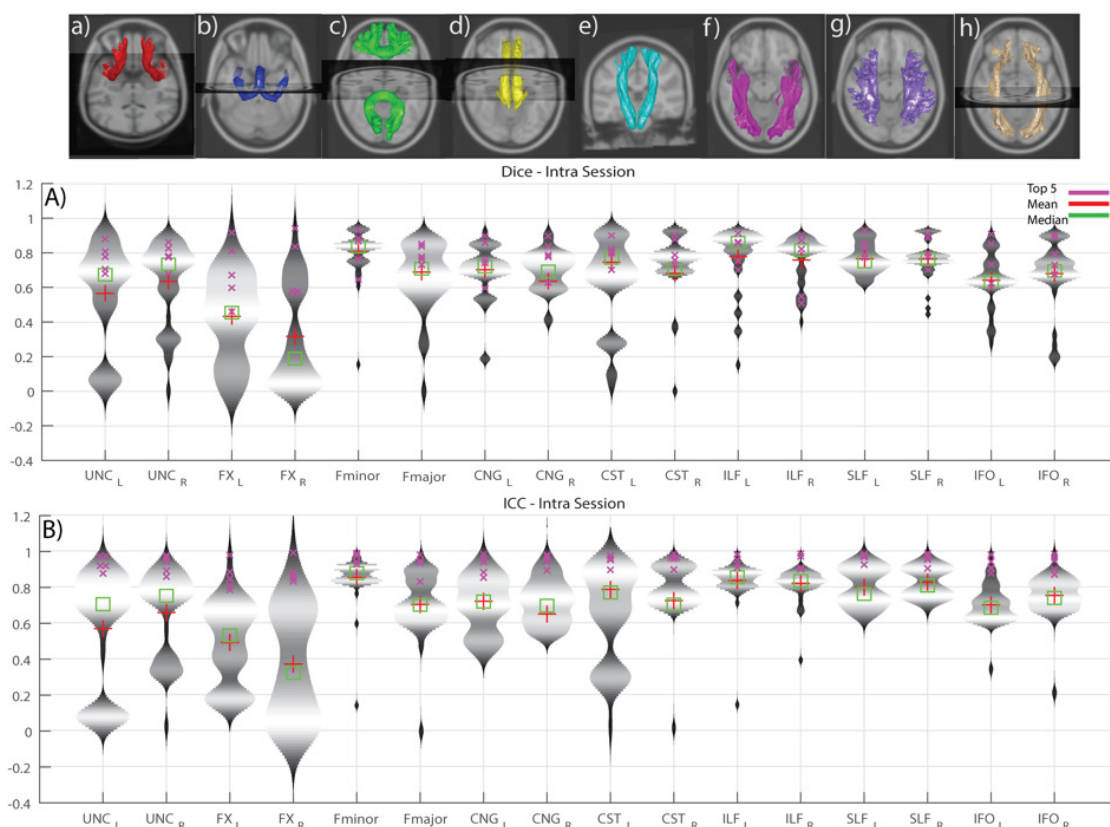


Figure 2.4 – Violin plots of intra-session submissions across both the scanners per tract. A) Dice similarity coefficients B) Intra-class correlation coefficients. The top row depicts the median of the top five intra-session submissions. More information of the name of the bundles can be found in the original manuscript [246]. *Reprinted from [246], Copyright 2019, with permission from International Society for Magnetic Resonance in Medicine.*

### 2.2.2 Results

The reproducibility, ICC, of the tractography methods varied from 0.27 to 0.97, however, most of the algorithms performed with a reproducibility of 0.6 or higher. Tensor and compartment models perform well, but trailed slightly worst compared to the submission that used Constrained Spherical Deconvolution (CSD).

Figure 2.4 identify "low", "moderate", and "high" reproducibility bundles. "High" reproducibility was defined as a median ICC greater than 0.6; less than 5% of entries obtain less than 0.4 ICC. "Moderate" reproducibility was defined as median ICC greater than 0.4; less than 25% of entries obtained less than 0.4 ICC. "Low" reproducibility was defined as a median ICC less than 0.4; more than 25% of entries obtained less than 0.4 ICC. The conclusive findings showed that, the "high" reproducibility bundles were genu of the CC, CST right, ILF, SLF and IFOF. The "moderate" reproducibility tracts were CST left, splenium of the CC, Cg. The "low" reproducibility tracts were UF and Fx.

### 2.2.3 Discussion

A tentative analysis to discriminate the best performing algorithms and the most relevant parameters to achieve reproducibility was performed. What was discovered is that, for example, the step size seems to be an important element. Most of the algorithm used 1/10 of the voxels size, this because it is a default value in most softwares. Moreover, algorithms using unconventional step size choices (e.g., 0.005 mm, 1 mm and 1.25 mm) achieve better results in terms of ICC. In terms of the threshold angle for tractography, different choices have been used. The outcomes showed a nonclear preferential threshold angle to set, and most likely, the optimal value is dependent on the algorithm of choice. High reproducibility has been found at lower threshold angles, 20 degrees, but also at 60 degrees.

Another notable finding is that even if most of the methods did not use additional post-processing steps, pipelines which included these last helped increase the reproducibility. In this category was proposed: outliers rejection and spurious fiber removal.

The volumetric analysis pointed out that bundles that showed conservative volume performed better in terms of reproducibility. However, small bundles showed lower reproducibility even with relatively small volumes.

This challenge pointed attention to the value of reproducibility in tractography, highlighting the difficulties in reproducing different WM bundles. As in other challenges [221, 307], no optimal set up of tractography was found. Known bundles challenging to reconstruct were also challenging to reproduce. Nonetheless, an important finding is those processing techniques used, i.e., COMMIT and Spherical-deconvolution Informed Filtering of Tractography (SIFT), helped in improving reproducibility results.

An important aspect to show is that the pipeline that won the competition included a final step of manual refinement of the WM bundles. This aspect shows that automatic pipelines require still improvement to reach the level of human accuracy.

### Personal considerations

Reproducibility of tractography reconstruction is a fundamental aspect in order to propose tractography as a tool of choice in clinical routine. The challenge provided an impressive acquisition set on one subject; however, it will be interesting to have more subjects with a similar acquisition to test the dependence of reproducibility of tractography on different brain topologies.

Another critical aspect to take into account is the metrics used for evaluation. Depending on the metric chosen results will show preferential algorithms. Advanced metrics are needed in the field to test reproducibility.

Moreover, a consensus of an optimal preprocessing pipeline has not been reached and will

be interesting to test the influence of preprocessing pipelines for the different reproducibility steps.

## 2.3 ISBI 2018: 3-D Validation of Tractography with Experimental MRI

Following the two ISMRM tractography challenges organized by ISMRM [221, 246], a third tractography challenge, named 3-D Validation of Tractography with Experimental MRI (3D-VoTEM), was organized in 2018 during the IEEE ISBI conference. This challenge consisted of three different validation sub-challenges:

- a macaque dataset with tracer connections [335]
- a squirrel monkey dataset with histology [305]
- a 3D physical fiber phantom

Similarly to the 2015 ISMRM tractography challenge, the goal is to test tractography algorithms and find advantages and limitations on ex vivo monkey brain and physical phantoms.

### 2.3.1 Dataset and evaluation

The first sub-challenge consisted on a validation of region-to-region connectivity with high quality, high resolution, and high angular sampling (114 sampling directions) - ex vivo macaque dataset, see figure 2.5a [335] . Two ground truth connections are reconstructed from anterograde tracer injections placed in the Posterior Commissure (PCG) (figure 2.5a, red) and the ventral part of the visual area V4 (V4v), see figure 2.5a, yellow.

The second sub-challenge consisted of both voxel-wise spatial overlap and region-to-region connectivity. The challenge is based on an ex vivo squirrel monkey dataset [305], acquired with 31 sample directions. The retrograde and anterograde tracer injection in the primary motor cortex (M1) define the ground truth. Furthermore, histological analysis allowed extraction of information about the bundles' volume, see figure 2.5b.

The third sub-challenge proposes of data acquired on a biomimetic anisotropic diffusion phantom (Synaptive Medical, Toronto, ON) with 16 separate fiber bundles, see figure 2.5d. The ground truth bundles was manually defined using a high-resolution T1-weighted image.

Standard metrics in the field were used to evaluate the accuracy of tractography. These can be divided into two categories: ROI-based and voxel-based. The ROI-based metrics measure the existence of connections between the two regions. This last was used in both squirrel monkey and macaque sub-challenges. Voxel-based methods are more quantitative, aiming to quantify the accuracy of the volumes generated by the streamlines. Voxel-based measures

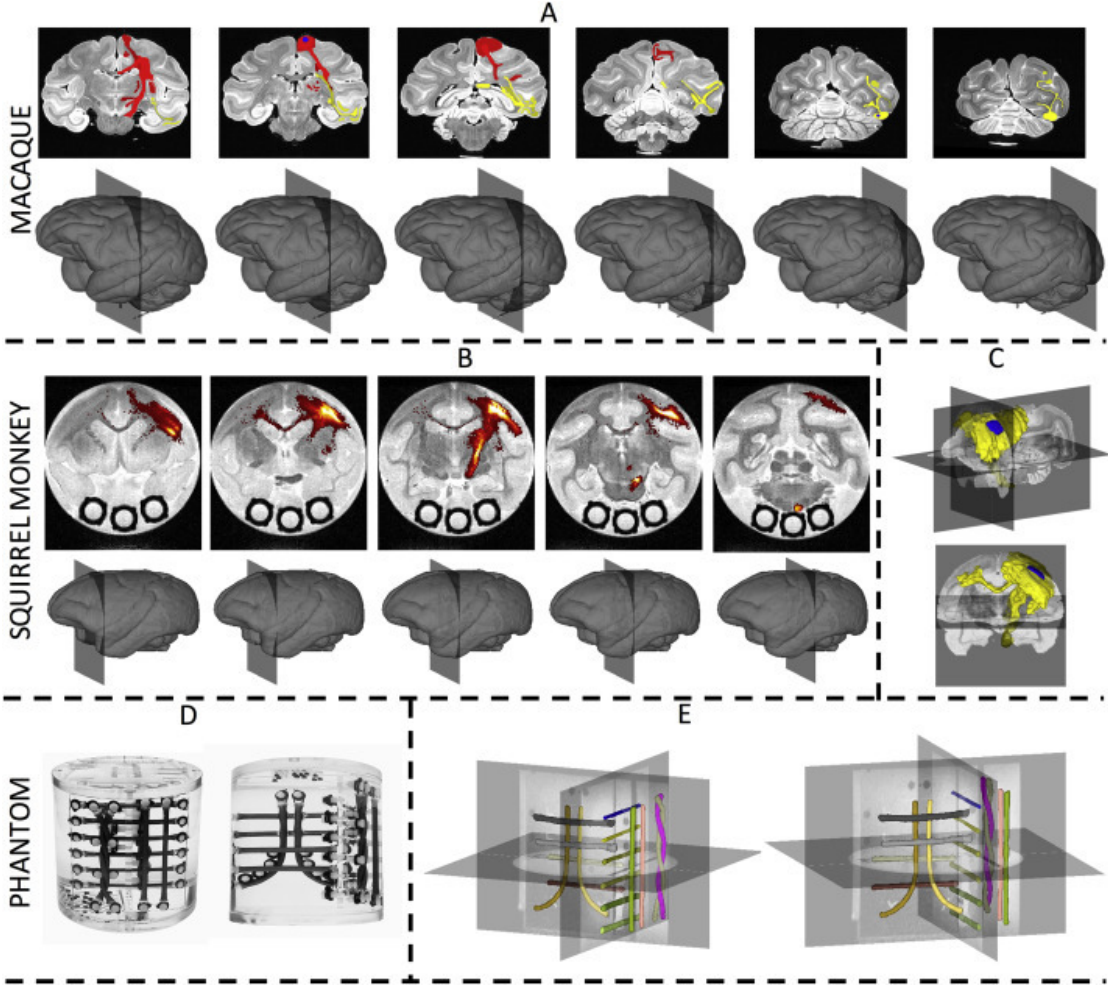


Figure 2.5 – Ground truth fiber pathways for the three sub-challenges. The figure shows different sections and visualizations for the three challenges. *Reprinted from [307], Copyright 2019, with permission from Elsevier Inc.*

### 2.3. ISBI 2018: 3-D Validation of Tractography with Experimental MRI

---

used in the challenges were VOL, VOR and Dice coefficient. In the study was measured the volume overlap, sensitivity measure, and the volume overreach, or specificity measure. These were computed for the squirrel monkey and phantom sub-challenges.

#### 2.3.2 Results

Results for the three sub-challenges of an example of submission are shown in figure 2.6. The final results show that there is considerable variability in the pathways submitted. For the monkey samples, reconstruction showed streamlines with a large spatial extent close to the seed regions, while long connections were more challenging to reach. Moreover, for the phantom submissions, the correct orientation, position and shape of all the bundles is generally well captured. However, differences were shown in the thickness of pathways and sparsity of streamlines.

#### Region-to-region connectivity

On ex vivo data, similarly to the findings in the ISMRM 2015 tractography challenge, the main result is that no tractography method identifies valid connections without also generating a large number of invalid connections. Hence, the increase in true positive rate, comes at the cost of a decrease in specificity, true negative rate. it is valid also the opposite.

#### Spatial overlap

In terms of volumetric analysis, a voxel-based measure between ground truth and tractography was performed on the second and third challenge. The results of overlap and overreach showed similar findings to the region-to-region connectivity: the price to pay to recover the ground truth volume of the pathways is a high overreach.

#### 2.3.3 Discussion

One of the main progress that this challenge achieved is to release material with histological validation freely. These datasets bring advantage, especially for those laboratories that develop tractography algorithms, but do not have the equipment and funding to perform these analyses.

#### Limitations and future perspectives

In general we assume that higher resolution is directly related to more accurate estimates. In this case, tractography in the macaque brain resulted in less precise connectivity compared to squirrel monkey; even if the first one has better resolution, Signal to Noise Ratio (SNR), and diffusion sensitivity. However, differences may be related to the diverse brain used in the first

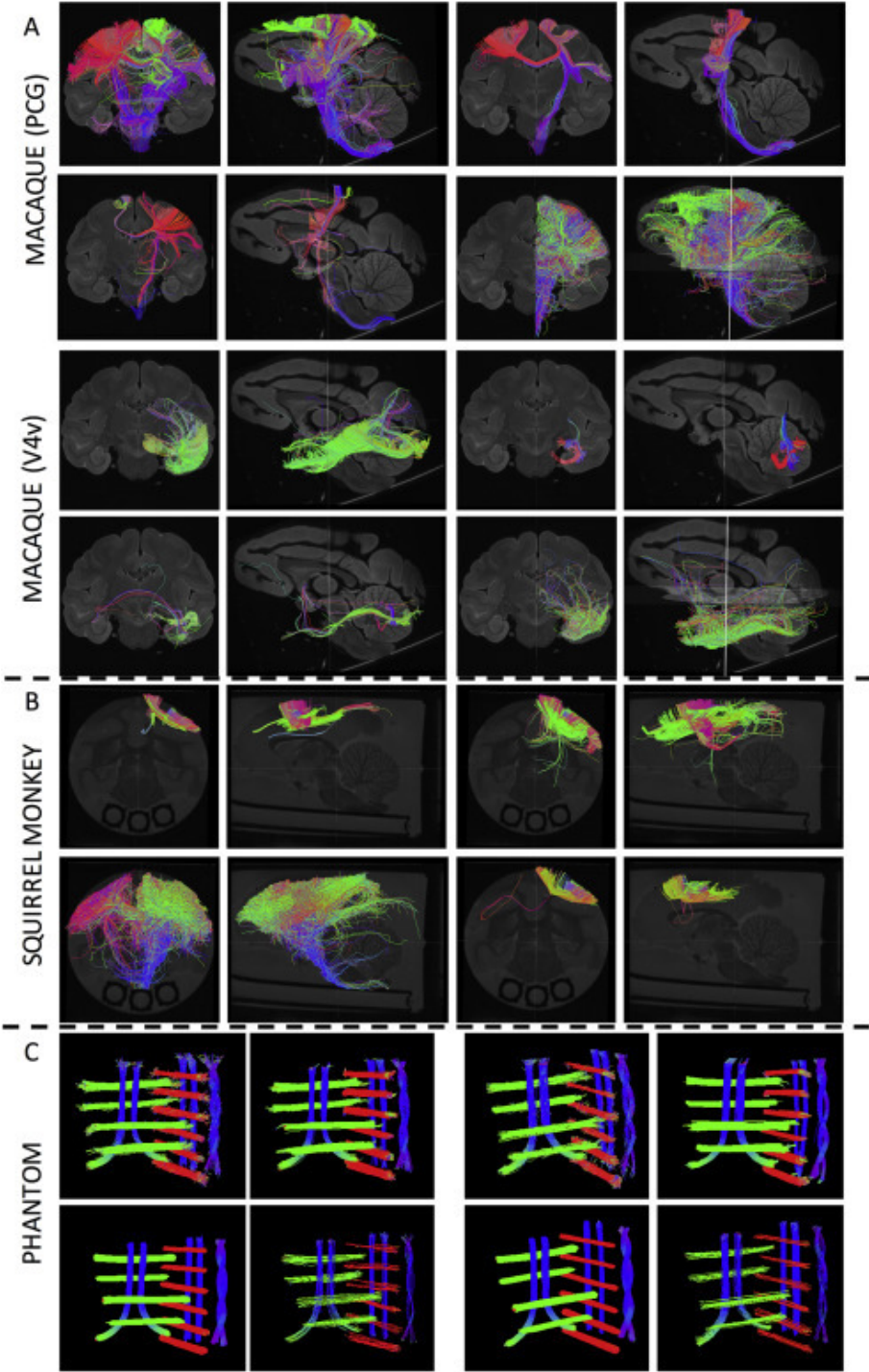


Figure 2.6 – Example of diffusion tractography submitted to the challenge. Coronal and sagittal view. Reprinted from [307], Copyright 2019, with permission from Elsevier Inc.

case and also in the complexity of the anatomical regions studied.

Most of the recent tractography pipelines include a variation of post-processing method.

### 2.3. ISBI 2018: 3-D Validation of Tractography with Experimental MRI

---

In the submission which contained a post-processing method, the specificity increased, and the overreach decreased. However, no significant difference was observed with different post-processing. A confounding factor that needs to be considered is that different pre-processing steps and tractography algorithms were used. This difference makes difficult the comparison of the results.

Improving tractography in these three sub-challenges does not guarantee an improvement directly on the human brain; however, it can provide a better understanding of the limitations. Other factors may limit validations methods, including imperfect registrations between histology and MRI or fixation. From the phantom physical perspective, the geometry build is still too simplistic compared to the complex brain architecture. A possible solution of how tractography can be improved was provided by Dyrby et al. [105] where the idea is to "loop until our method's results agree with the gold standard, and/or until the updated knowledge of ground truth can explain the discrepancies observed."

Surely, there is a need for more advanced gold standards. Furthermore, the metric used till now to analyze the connectivity is quite simple; validation is done as an overall assessment in sensitivity and specificity. However, future studies should focus on using more complementary information and microstructural features of the datasets.

#### **Personal considerations**

The results of this challenge confirm previous findings [19, 100, 335]. More specifically, the main limitations of tractography are: algorithms show a trade-off in specificity and sensitivity. The long-range connections are harder to detect compare to short-range connections, and tractography performs worst when assessing connectivity of fine small connectivity compared to large-scale regions. This challenge confirmed that these limitations have not been yet solved.

Challenges that use ex vivo or physical phantom add a higher and more realistic level of complexity compared to numerical simulations. However, most of the time it may add more problems related to imaging artifacts instead of solving the wiring of the brain through DW-MRI.

In this case, was proposed several challenges that may need completely different optimal tractography algorithms to be solved. Hence, a possible solution is to focus on a specific, well-defined problem. Ideally trying to isolate the problems, for example, having common pre-processing steps or other, and try to conclude and eventually report achievements.

As shown in this chapter, tractography has many limitations. Perhaps, there is a need to focus and work on specific directions, without dissipating energies between different problems. This focusing process may lead to an acceleration in the development of tractography.

### 2.4 Conclusion and Discussion

In this chapter, we presented three different tractography challenges proposed between 2015 and 2018, which aimed to highlight the limitations and positive aspects of nowadays tractography algorithms.

From a philosophical and personal perspective, I consider these challenges an effective group re-focusing exercise. As athletes need a certain number of skills and rules to achieve excellence in their field [261], tractography needs to pass also a certain number of challenges in order to evolve and become more robust and used.

Since in this thesis we will use microstructure informed tractography, which lies on the benefits of tractography, it is essential to understand the limitations of tractography to be able to use and understand the results of this novel technique.

The variety of validation technique proposed gives hope that tractography will be improved in different aspects during the next years; eventually, a consensus will be reached among the MRI community.



## 3 Towards 3D histological validation of DW-MRI fiber orientation

Tissue clearing techniques offer new opportunities for imaging precise 3D axons trajectories. In this study, we cleared a 1.5 cm x 1.5 cm x 0.3 cm cuboid of rhesus macaque visual cortex using CLARITY 3D histology with immunostaining for neurofilament to highlight neuronal projections. We then confronted the CLARITY-based fiber orientation estimate to DW-MRI-based fiber orientation. The comparison confirmed a better agreement in GM than in WM, potentially reflecting complexities estimating the structure tensor in highly saturated regions of the CLARITY sample.

The study was performed in one of the largest and highest quality CLARITY cuboids from a macaque brain and explored critical steps in the co-registration and analysis required to make a robust comparison with DW-MRI data.

### 3.1 Introduction

A crucial goal in neuroscience is to understand the connectivity between neural populations by visualizing fiber pathways in the brain *in vivo* [154, 309, 324]. More specifically, there is an essential need of a technology capable of achieving *in vivo* axon resolution, i.e., 1  $\mu\text{m}$  to 10  $\mu\text{m}$ . As mentioned in previous chapters, scientists nowadays use DW-MRI [183], a non-invasive technique that can indirectly estimate microstructure fiber orientations [30] to recover axonal orientations. For each voxel, typically in the order from 1 mm to 3 mm, DW-MRI probe the random motion of the water molecules in various directions, relying on the increased mobility of water molecules along axons than perpendicular to them. Thanks to these measurements and reconstruction algorithms, it is possible to estimate micro-structure properties of axons, e.g., fiber orientation, up to a certain level of accuracy.

### 3.1.1 Estimating fiber orientation

Diffusion fiber orientation can be reconstructed using a variety of methods [30, 57, 78, 343], see chapter 1.4 for more details. However, due to the absence of proper GT, evaluation and performance of algorithms are limited to the validation technique used.

Previous studies addressed the issue of reconstruction and validation, generating synthetic data [74]. Still, these numerical phantoms are limited by the over-simplistic description of the neural tissue.

To generate more realistic validation designs, studies on ex vivo human, [230, 231, 234] and monkey [50, 335] brains have been proposed, see chapter 2 for more details. The main advantage of performing ex vivo acquisition is that brains can be scanned for a longer time allowing achievement of better resolution; typical high-resolution acquisitions are in the order from 150  $\mu\text{m}$  to 300  $\mu\text{m}$ . After scanning with MRI, histology using microscopes is done to recover a GT.

### 3.1.2 2D histology

Histological data have been used to analyze the mesoscale structure of the tissue in slices [62, 133, 209, 312]. Attempts to reconstruct the 3D wiring of the brain was performed concatenating 2D slicing using numerous techniques: confocal microscopy [176, 193, 304, 306], optical coherence tomography [358] and polarized light imaging [18, 80, 150, 215, 235].

In 2D histology, the brain is cut in thin slices, which are imaged and subsequently reconstructed in 3D. However, 2D histology suffers from tissue deformation during cutting [188], e.g., folding, stretching, compression. These last can lead to artifacts and ambiguity in the 3D reconstruction.

Nowadays, to obtain good 3D reconstruction and avoid artifacts, histologists must be very careful. The accurate manual reconstruction of fibers is enormously time-consuming, and lead to a typical reconstruction of only a few fibers. Recently, semi-automatic algorithms were introduced to segment and label large portions of tissue [38] and, e.g., optical computer tomography (OCT) [210] and tissue-clearing techniques [64, 67, 98, 112, 149, 289, 293, 325], were proposed to overcome previous mentioned limitations. In this thesis, we will focus on tissue-clearing techniques to validate fiber orientations.

### 3.1.3 Tissue clearing and 3D histology

Tissue-clearing techniques [64, 67, 98, 112, 149, 289, 293, 325] allow the volumetric reconstruction of biological tissue. These techniques homogenize the refractive index in the sample, reducing the light-scattering, and allowing deep light penetration for 3D microscopy.

Several techniques have been proposed in the last few years. One of the most promising is

CLARITY [64]. In a nutshell, CLARITY embeds the tissue in an acrylamide-based hydrogel that binds to the proteins in the tissue. Then, the biomolecules that did not bind to the hydrogel, i.e., lipids, are washed. Last, the refractive index is homogenized by replacing the water in the sample with a refractive index matched solution. Compare to other tissue clearing techniques, the major benefit of CLARITY is that it allows a minimal loss of protein during the washing [214], keeping the 3D structure more intact.

CLARITY has been applied to mouse brains to pathology's like Alzheimer [9], autism [64], epilepsy [67], neuro-degeneration due to mitochondrial disease [278] and Parkinson's [218]. Moreover, studies used CLARITY as a validation technique for fiber trajectories; firstly in mouse [214], and recently, the protocol has been tested in tiny human tissue specimens [236].

## 3.2 Methods

### 3.2.1 CLARITY-based tissue clearing acquisition

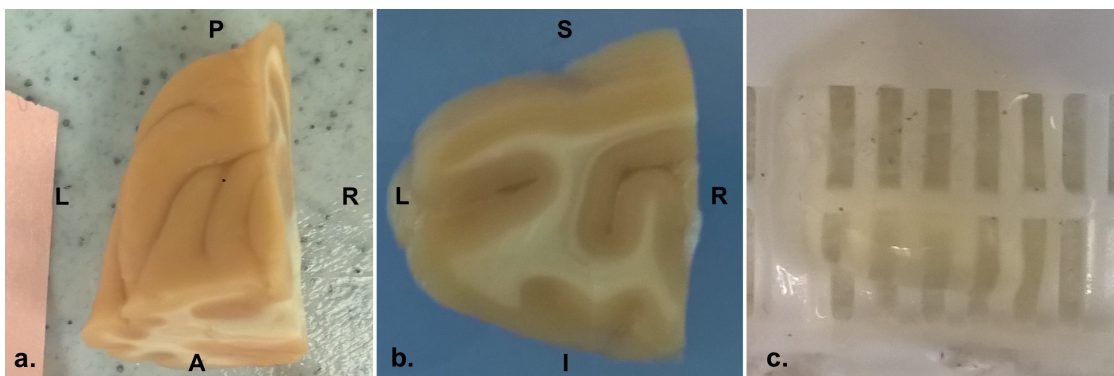


Figure 3.1 – The photographs show the part of monkey brain tissue treated at Stanford University used for the CLARITY clearing. (a.) Brain cut of the posterior lateral part of the left hemisphere (LLP). (b.) LLP4, the piece of tissue chosen for the analysis. (c.) LLP4 after clearing using the CLARITY protocol and lying inside a container.

The macaque brain was cut, and the posterior lateral part of the left hemisphere (LLP; Figure 3.1a) was extracted. A slab in the middle of the tissue block (LLP4, Figure 3.1b), 15 mm x 15 mm x 3 mm size, was chosen for the analysis, and a  $T_1$  weighted sequence was acquired with resolution 0.2 mm x 0.2 mm x 0.2 mm. The slab was cleared using the CLARITY protocol [338] and stained for neurofilaments using the SWITCH protocol [244], with active clearing with electrophoresis in a custom-designed chamber with continuous exchange of sodium dodecyl sulfate (SDS) solution. A small portion of the LLP4 cleared slab (Figure 3.1c) was imaged with a two-photon microscopy [91] at 1.5  $\mu\text{m}$  isotropic resolution, generating a cuboid of 2.6 mm x 2.8 mm x 0.25 mm size (Figure 3.2d). An overview image of the LLP4 was taken with a confocal microscope to localize the two-photon microscopy images (Figure 3.2c). Lastly, the 3D histological images were processed in Fiji [308] for bleach correction, blurring reduction using Gaussian filtering with a kernel size 1/10 of the image dimension, median filtering with

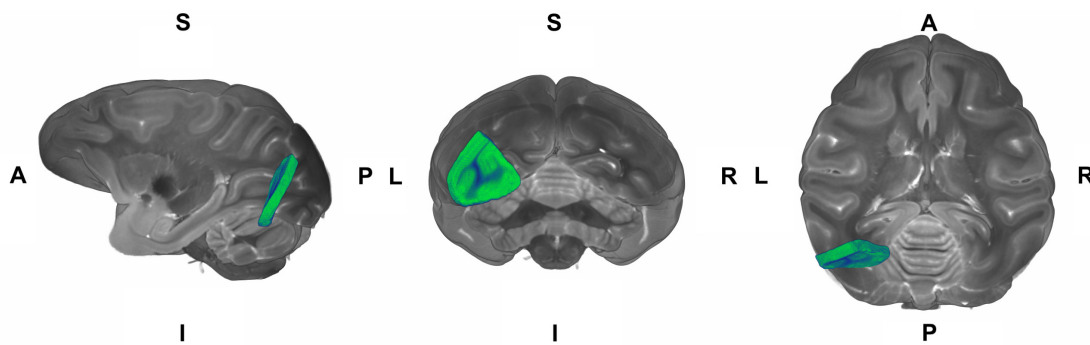


Figure 3.2 – Registration of the LLP4 monkey slab chosen for the analysis and acquired at Stanford University to the whole-brain b0 of a different monkey used in the work of Thomas et al.[335] From left to right: sagittal, coronal and axial view.

pixel size 1, and ultimately, contrast and brightness were adjusted. Fiber orientation from the histological 3D CLARITY data was initially estimated using the structure tensor technique [40, 45].

#### 3.2.2 MRI imaging acquisition

Before cutting, the whole postmortem fixed rhesus macaque brain was scanned on Bruker BioSpin MRI 7T animal system at Stanford University with a Turbo RARE  $T_2$  weighted sequence: resolution 0.15 mm x 0.15 mm x 0.5 mm, TE=53.4 ms, TR=25 s.

The DW-MRI dataset was used from an open available dataset of another monkey brain. The dataset consist of a high-resolution 0.25 mm isotropic macaque brain used in previous studies [291, 307, 335] and also in the ISBI challenge mentioned in chapter 2. The ex vivo brain was acquired in Bethesda at the National Institute of Mental Health (NIMH). We recall the DW-MRI protocol: 114 directions with b-value = 4900  $\text{s mm}^{-2}$  and 7 volume of b-value = 0  $\text{s mm}^{-2}$ . The data were furnished already preprocessed for eddy currents distortions and frequency drift with the Tolerably Obsessive Registration and Tensor Optimization Indolent Software Ensemble (TORTOISE) tool [280] .

Anatomical regions were identified with an expert anatomist. Furthermore, a secondary analysis was performed registering a high-resolution 0.15 mm isotropic macaque brain atlas [50] (Figure 3.3d) from the Center for In Vivo Microscopy (CIVM), Duke University. This second co-registration step was performed to test the accuracy of the localization of the brain with an automatic tool. Both analyses, manual and automatic, ended with the same conclusion.

#### 3.2.3 Co-registration

The co-registration pipelines used are the following: 1) identification of the two-photon (Figure 3.3a) images location was recognized by image contrast created by fluorescent bleaching of

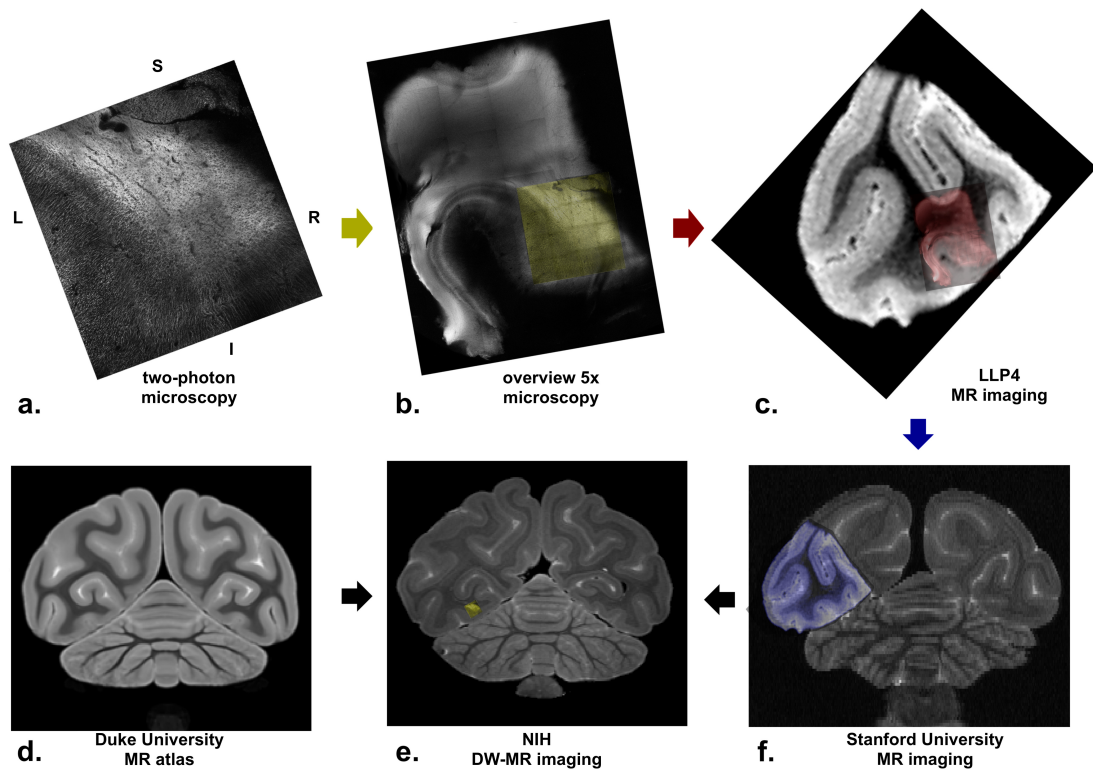


Figure 3.3 – (a.) CLARITY two-photon microscopy images (b.) Registration of CLARITY two-photon microscopy images to the CLARITY overview 5x microscopy; registration helped by fluorescent bleaching. (c.) Registration of CLARITY overview 5x microscopy to structural MRI  $T_1$  of slab LLP4. (d.)  $b$ -value=0  $\text{s mm}^{-2}$  of the Duke University MR monkey atlas used to annotate anatomical regions in visual cortex. (e.)  $b$ -value=0  $\text{s mm}^{-2}$  of NIMH monkey dataset used to co-register the CLARITY data (f.) Registration of structural MRI  $T_1$  images of the slab LLP4 to the structural whole-brain  $T_2$  MRI images.

the overview image (Figure 3.3b); 2) initial manual registration and linear registration of the overview images to the  $T_1$  weighted LLP4 slab (Figure 3.3c); 3) rigid registration of the  $T_1$  weighted LLP4 to the  $T_2$  weighted whole brain acquisition (Figure 3.3f). All previous steps are performed on the same monkey brain, with data acquired at Stanford University. 4) rigid registration of the  $T_2$  weighted Stanford whole macaque brain to the NIMH  $b$ -value=0  $\text{s mm}^{-2}$  image whole macaque brain (Figure 3.3e). Manual registration were performed with 3D Slicer [116] and linear registration with elastix [195]. To refine the initial point co-registration between the NIMH macaque brain diffusion tensor and CLARITY structure tensor a vector field rigid registration algorithm was developed. The optimization algorithm minimizes the angular vector distance allowing rotation and translation. Finally, all the registration matrices were concatenated, and a final intensity-based linear registration with elastix[195] was used to avoid unnecessary blurring.

### 3.2.4 Structural tensor estimation

The fiber orientation for the CLARITY data was estimated using the eigenvector of the smallest eigenvalue of the structure tensor [40, 45] defined as:

$$\mathbf{S} = \begin{bmatrix} \sum_{p \in w} (I_x(p))^2 & \sum_{p \in w} I_x(p) * I_y(p) & \sum_{p \in w} I_x(p) * I_z(p) \\ \sum_{p \in w} I_x(p) * I_y(p) & \sum_{p \in w} (I_y(p))^2 & \sum_{p \in w} I_y(p) * I_z(p) \\ \sum_{p \in w} I_x(p) * I_z(p) & \sum_{p \in w} I_y(p) * I_z(p) & \sum_{p \in w} (I_z(p))^2 \end{bmatrix} \quad (3.1)$$

$I_x$ ,  $I_y$ , and  $I_z$  are the gradients of image volumes  $I$  along each of the x, y and z axes. A 3-dimensional 1st order derivative of Gaussian filters of standard deviation  $1 \mu\text{m}$  was used to recover the coefficients  $I$ . The structure tensor was computed over cubes of lengths of one side equal to 166 voxels, equivalent to  $250 \mu\text{m}$ ). From the structure tensor estimations, principal directions were extracted using the MRtrix3 software [341].

### 3.2.5 Structural fiber orientation distribution estimation

In the structure tensor estimation, we performed analysis on a cube of  $166 \times 166 \times 166$  voxels, equivalent to  $250 \mu\text{m} \times 250 \mu\text{m} \times 250 \mu\text{m}$ . We subdivide the cubes into smaller sub-cubes, and we calculate the polar histogram of all principal direction of the structure tensors. The polar histograms were then fitted with spherical harmonics with order  $l_{max} = 8$  with the MrTrix3 software [341] to generate structure Orientation Distribution Function (sODF).

We varied the sub-cubes dimensions to study the influence of this parameter in the reconstruction of the sODF. Values reported in this study are:  $2 \times 2 \times 2$ ,  $4 \times 4 \times 4$ ,  $8 \times 8 \times 8$  and  $16 \times 16 \times 16$ , corresponding respectively to structure tensors of length size  $83 \times 83 \times 83$ ,  $41 \times 41 \times 41$ ,  $20 \times 20 \times 20$  and  $10 \times 10 \times 10$ . These values are chosen to keep the voxel size to  $250 \mu\text{m}$  to allow comparison with the diffusion FOD.

Segmentation to separate WM and GM regions were performed with a threshold on the DW-MRI b-value =  $0 \text{ smm}^{-2}$  image.

## 3.3 Results

### 3.3.1 Localisation and co-registration

In this study, we performed CLARITY on a portion of the primary visual cortex of a rhesus monkey 3.1, and we imaged a portion of the cleared sample with two-photon photon microscopy for structure tensor analysis. For better localization, the sample was then co-registered, see figure 3.2, and compared to a second monkey acquired with high-resolution and diffusion gradient strength DW-MRI data used in previous work [335].

Figure 3.3 shows in yellow the position of the two-photon microscopy image after co-registration to the macaque brain [335].

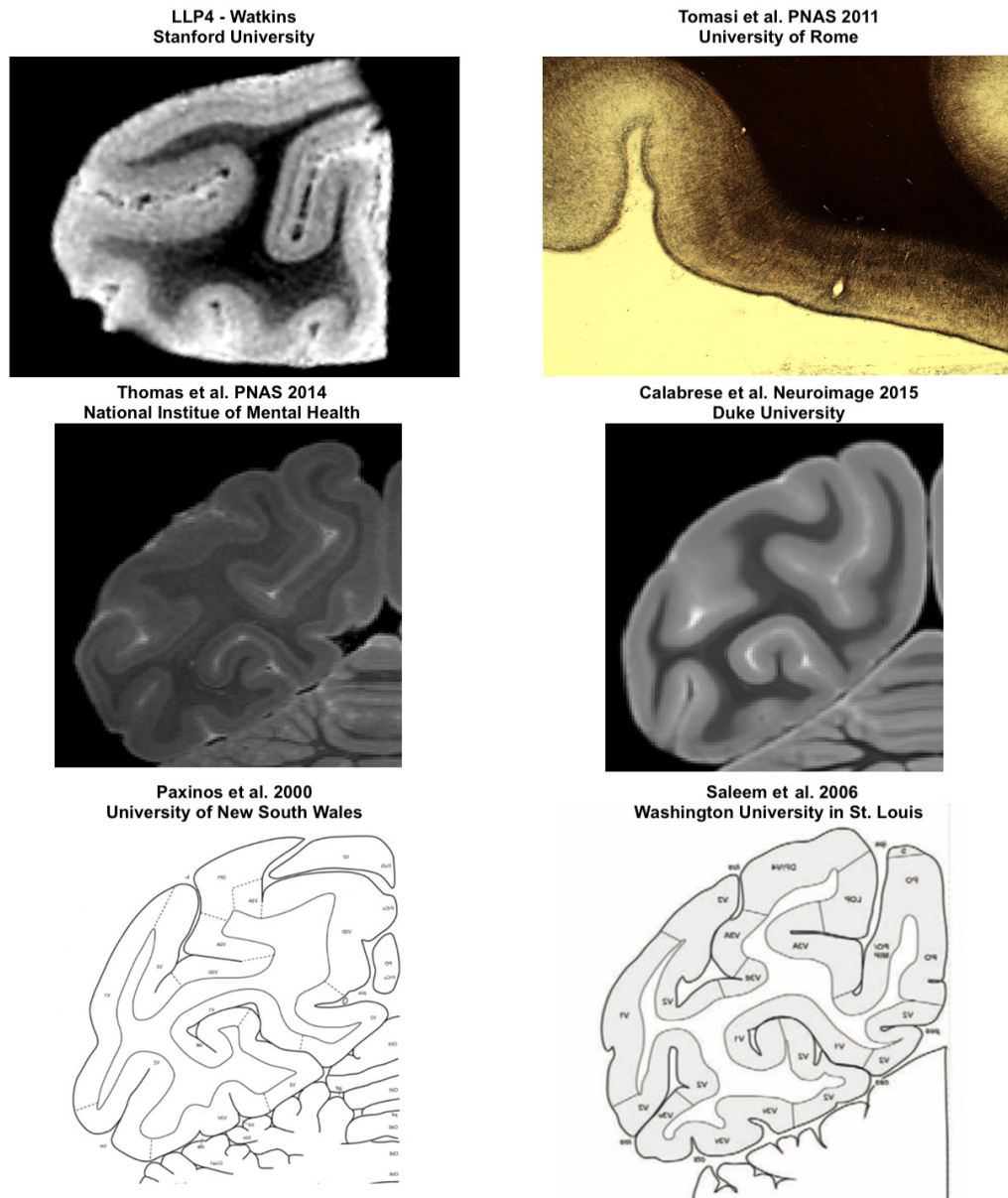


Figure 3.4 – Six different sections of the monkey brain corresponding to location for which CLARITY two-photon microscopy was acquired. The region corresponds roughly to the same section area. The investigation was performed by an expert anatomist.

With an expert anatomist, G.M.I., we analyzed the localization of the two-photon microscopy CLARITY sample in five different monkeys: two monkey atlases [270, 298], two MRI dataset [50, 335] and one monkey 2D histology section [336]. The slice corresponding to the CLARITY sample is shown in Figure 3.4.

### Chapter 3. Towards 3D histological validation of DW-MRI fiber orientation

---

We report differences in morphology between the same region across all the data analyzed. Morphological differences in brains are known; human studies on the human brain have quantified this aspect [22]. We can assume similar findings in the monkey brain.

The analysis across the five monkeys was done accounting for the possibility of different preparation of ex vivo material and different angle of slice sections for MRI and histology. Taking into account these considerations, we do not believe that the difference in brain morphology can be due to those reasons. Furthermore, we report a non-negligible variation in the organization of the WM and GM in this specific visual area of monkey brains.

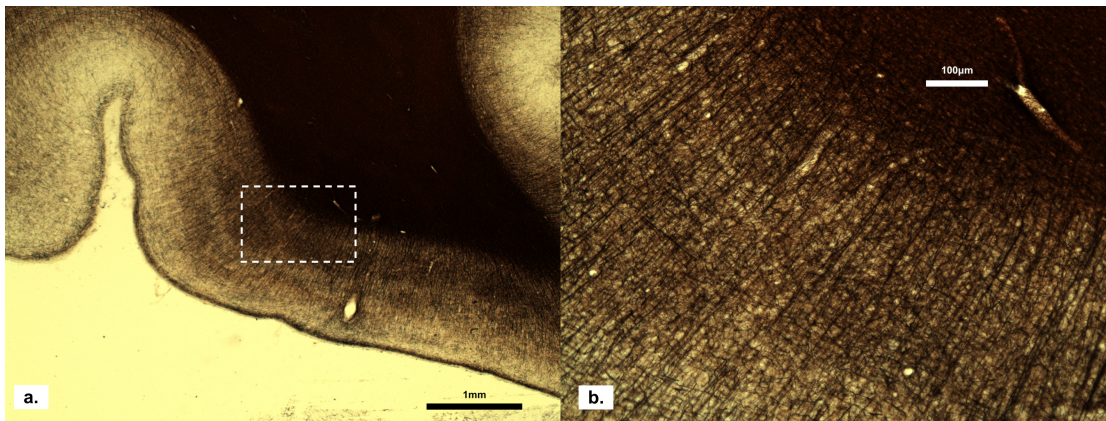


Figure 3.5 – 2D histology of the section corresponding to the same location for which CLARITY two-photon microscopy images were acquired; the data correspond to the CCT4 monkey reported in the work [336]. (a) Overview image b) Zoomed image corresponding approximately to the CLARITY two-photon images.

When investigating orientations, the first analysis with 2D histology in a different monkey brain [336] was performed to get the orientations qualitatively in GM and WM, Figure 3.5. Fibers in the GM, as known from previous literature, are perpendicular to the interface of the WM. In the WM, Figure 3.6, we do not report a preferred orientation of the neurofilaments. This finding can be due to an orientation of the neurons in anterior-posterior, where the coronal sectioning of the 2D histology material cannot be helpful; sectioning on a sagittal or transverse plane may reveal a preferential orientation for WM.

To associate cortical regions to the imaged sample, our expert anatomist G.M.I used two atlases [270, 298]. Figure 3.7 report the closest visual area regions to the location of the sample (green arrow).

#### 3.3.2 Tensor comparison

To evaluate the difference in orientation between the CLARITY and DW-MRI estimations, we initially used the simplest method proposed in the literature, the tensor. Figure 3.8 shows the voxel comparison of the main fiber orientation estimation from structure tensor (Figure 3.8a)



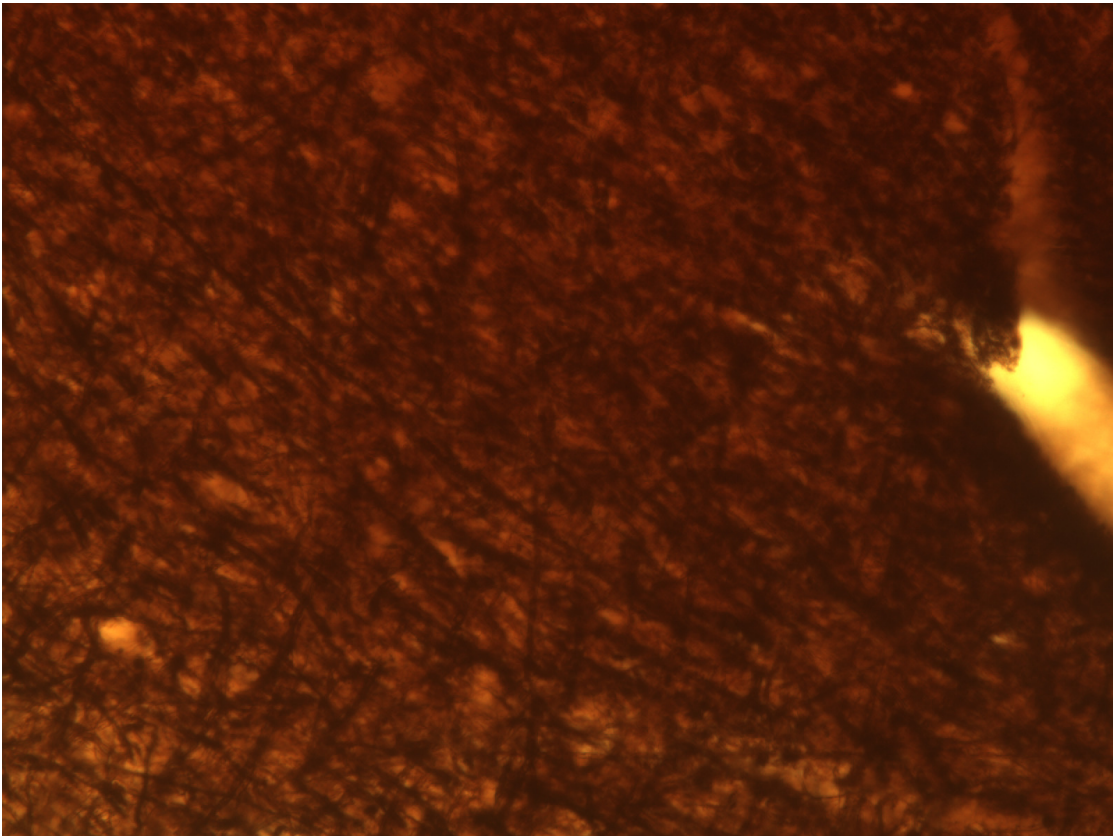


Figure 3.6 – 2D histology of the section of white matter zoomed from the section in figure 3.5; data correspond to the CCT4 monkey reported in the work [336].

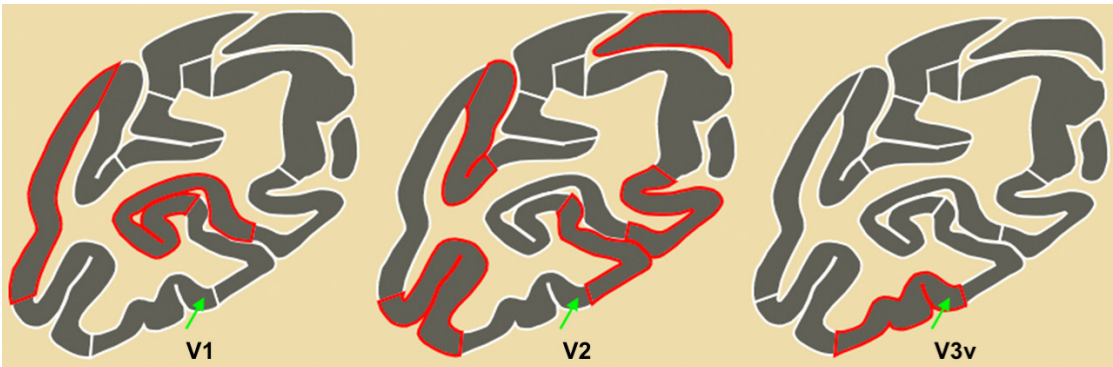


Figure 3.7 – Anatomical characterization of the LLP4 slab used for which CLARITY two-photon microscopy data were acquired. The Paxinos et al. [270] atlas was used to parcellate the visual cortical regions in V1, V2 and V3 ventral.

and the diffusion tensor (Figure 3.8b).

By visual inspection, we confirm that the primary vector in the structure tensor is defined in the direction of eigenvector with the lowest eigenvalues; differently, from the diffusion

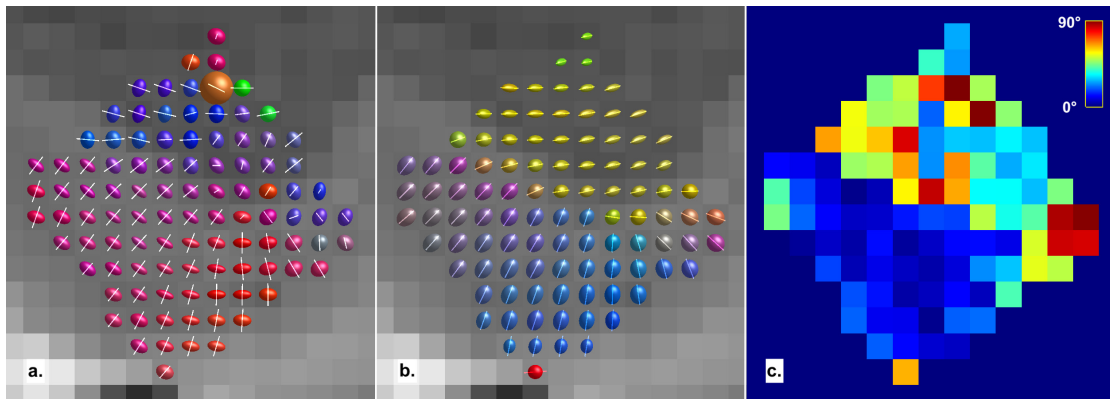


Figure 3.8 – Tensor estimation on the region associated with CLARITY acquisition, and comparison. (a.) Structure tensor estimation; (b.) diffusion tensor estimation; (c.) angle of difference between the structure tensor and the diffusion tensor. Color code for figure (a.) (b.) are: red for right-left, blue for dorsal-ventral, and green for anterior-posterior.

tensor where the main direction is related to the eigenvector with the highest eigenvalue. Furthermore, we report a better orientation agreement in the GM voxels and worst agreement in the WM voxels.

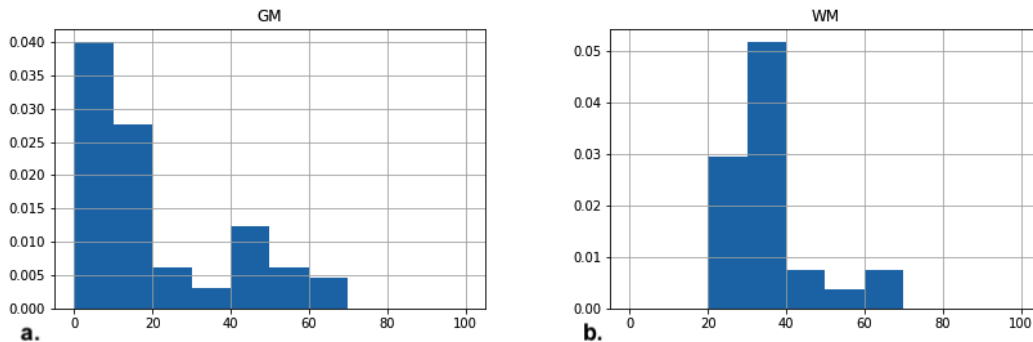


Figure 3.9 – Histogram of angle differences using the tensor analysis in (a.) Grey Matter (GM) (b.) White Matter (WM).

Figure 3.8c shows a comparison of the angle between the two tensors. We report an angle of difference of  $21.00^\circ \pm 18.55^\circ$  in GM and  $42.03^\circ \pm 16.15^\circ$ . Furthermore, we analysed the histograms of angle differences in GM and WM, see Figure 3.9. We report a good agreement in GM with 68% of voxels with an error below  $20^\circ$  and 40% of voxels with an error below  $10^\circ$ .

### 3.3.3 Orientation distribution function comparison

Tensor analysis is limited to a single bundle population. In this section, we extended the tensor model, introducing *ODF*, and allowing comparison of multiple populations in a voxel. Comparative analysis of *ODF* voxels is reported in Figure 3.10. *ODF* are distinguished in fiber

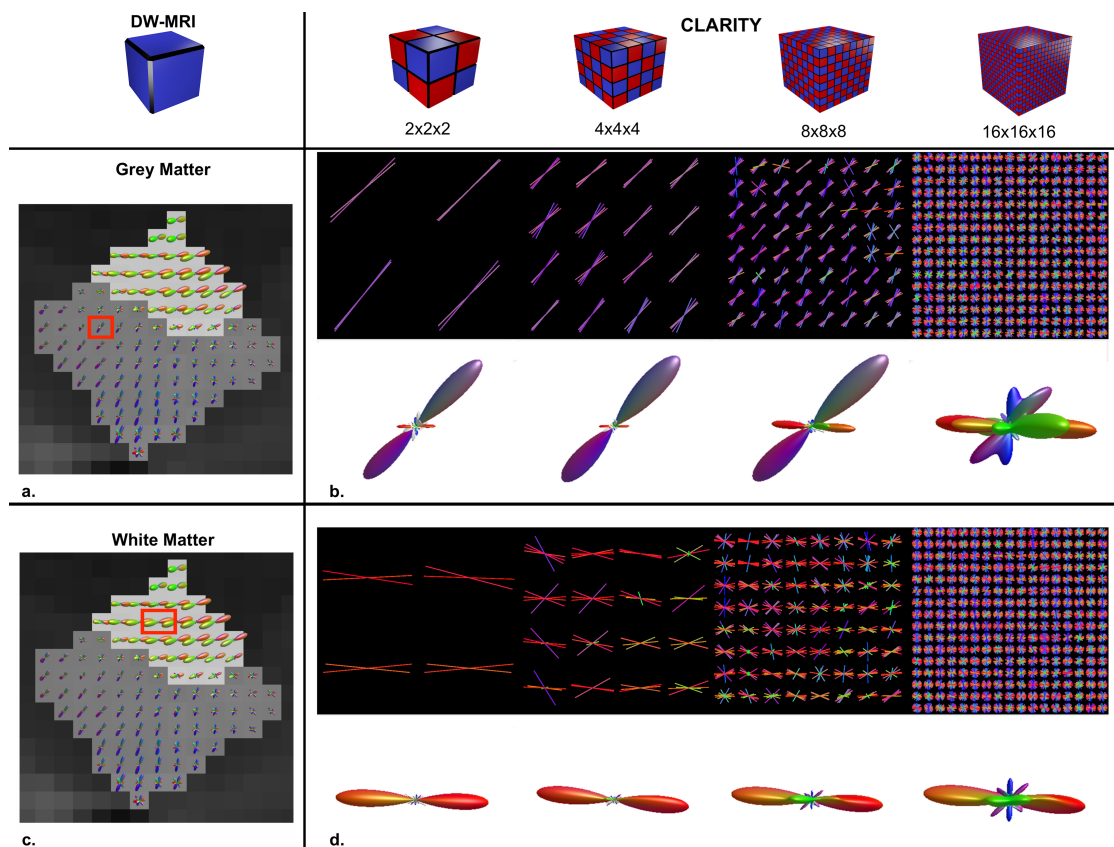


Figure 3.10 – Qualitative analysis of *ODFs*. Figure (a.) and (c.) show *FOD* estimated using constraint spherical deconvolution on NIMH macaque data [335]. Figure (b.) and (c.) show *sODF* varying the sub-voxel size, respectively, with sub-cubes of 2x2x2, 4x4x4, 8x8x8 and 16x16x16; spherical harmonics functions were computed using MrTrix[341] on CLARITY two-photon microscopy images. (a.) A grey matter voxel is highlighted on top of a *FOD* reconstruction. (b.) *sODF* estimations for a grey matter voxel highlighted in figure (a.), first-row show vectors, second-row show the corresponding *sODF*. (c.) A white matter voxel is highlighted on top of a *FOD* reconstruction. (d.) *sODF* estimations for the white matter voxel highlighted in figure (c.), first-row show vectors, second-row show the corresponding *sODF*. Qualitatively we report a variation of *sODF* shape varying the sub-voxel size. Voxels with high sub-cubes, i.e. 16x16x16, have *sODF* more noisy.

*ODF* (*FOD*) if generated from DW-MRI data, and structural *ODF* (*sODF*) if generated from microscopy images.

In 3.10 we compare qualitatively the *FOD* and the *sODF*. The *sODF* can be generated summing structural tensors of different size. A sensitivity analysis was performed exploring different values for tensor size. In 3.10 we report the results for subcubes of 2x2x2, 4x4x4 and 8x8x8 and 16x16x16.

We show how the *sODF* shapes vary, changing the structural tensor size. In particular, the *sODF* increase in the number of population peaks when structural tensor of small size voxels

### Chapter 3. Towards 3D histological validation of DW-MRI fiber orientation

is used, e.g., 16x16x16.

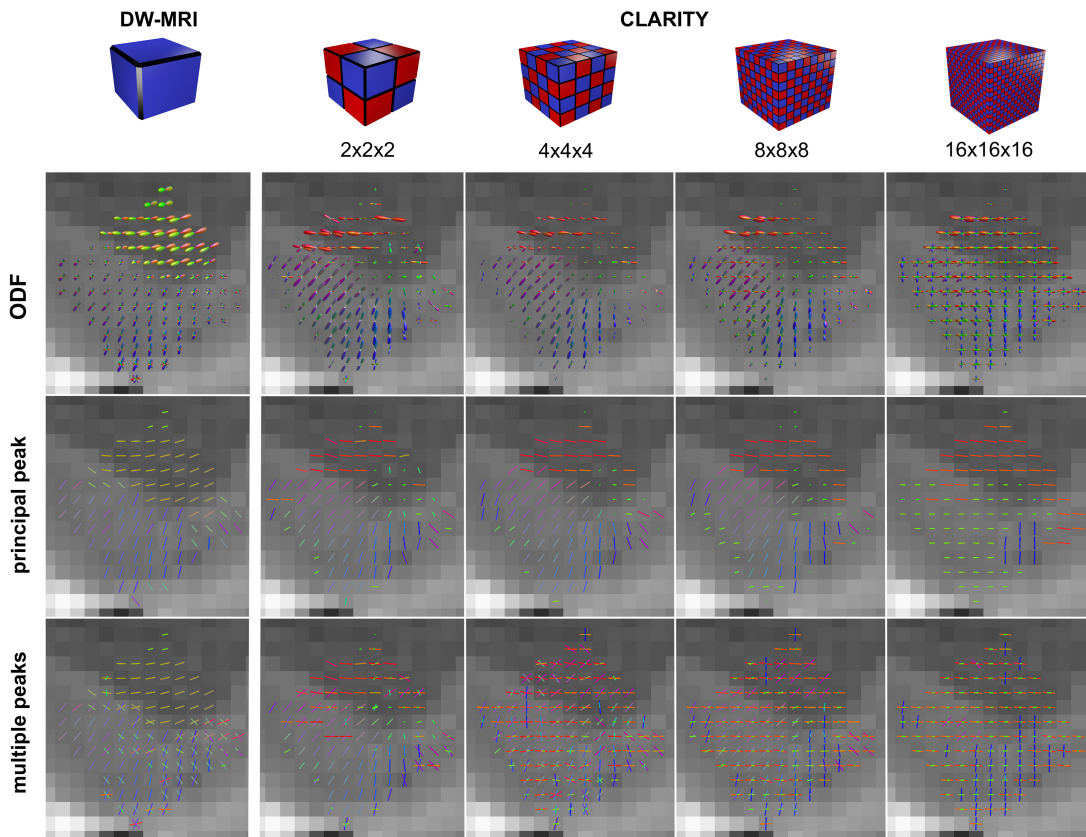


Figure 3.11 – *ODF* analysis on DW-MRI data and CLARITY two-photon microscopy. First-column shows DW-MRI estimations; the other columns represent CLARITY two-photon microscopy estimations. First-row shows *fODF* and *sODF*, respectively for DW-MRI and CLARITY. Second-row show principal peak and third-row show multiple peaks extraction.

In 3.11, we report the *ODF* for the whole sample where we performed a quantitative analysis. The second and third row of the figure 3.11 report respectively the main peak and all the peaks found above a threshold amplitude of 0.3. Comparative results show that DW-MRI analysis commonly obtains more sporadic peaks compared to CLARITY imaging, where we obtain multiple fiber populations, both in GM and WM.

Furthermore, we used the principal peak estimated from DW-MRI and CLARITY to compare the angle of difference. Results are shown in the following table:

sODF	WM	GM
2x2x2	47.76 +/- 14.63	28.34 +/- 21.04
4x4x4	40.05 +/- 11.54	24.12 +/- 15.71
8x8x8	38.79 +/- 14.31	36.26 +/- 26.41
16x16x16	35.10 +/- 10.87	58.42 +/- 11.26

Similar to the tensor analysis, the best results are in GM, where we find good agreement for the structure tensor of 41x41x41 voxels. This result is only 3 degree less accurate compared to the previously reported with the tensor analysis.

## 3.4 Discussion

During the last decades, thanks to the development of MRI and DW-MRI, scientists started to use these techniques to study the cortical connections. The main point in favor of DW-MRI, compared to alternatives approaches, i.e., histology, is the possibility to perform faster analysis [10]. DW-MRI is a relatively young technique and can be used to extract fiber orientation features in vivo. However, parameter estimation needs to be validated accurately.

In this study, we use ex vivo material to create a comparative pipeline. We acknowledge that ex vivo monkey findings may not apply to humans; nonetheless, so far it is the best validation method that can be used.

Our study performed CLARITY on one of the first and the largest monkey sample. Our ultimate goal was to estimate fiber orientation on a relatively large portion of tissue.

We compare CLARITY findings to DW-MRI estimates. Unfortunately, the main limitation of the work is that we are limited to a comparison between two different monkey brains. Hence, the co-registration steps need to be taken carefully, and this aspect may limit the findings of our use of CLARITY as a validation technique for DW-MRI. However, the central message of the study is the significant methodological contribution in terms of the design of the co-registration pipeline and implementation of a novel sODF for 3D microscopy imaging data.

In the following section, we discuss critical steps in co-registration, and WM and GM comparisons.

### 3.4.1 Co-registration

To register the CLARITY two-photon microscopy images of the Stanford University monkey to the b0 NIMH monkey brain, we performed different co-registration steps. All steps were performed using linear registration[116, 195]. However, non linear registration could have been used, especially between two critical steps of the pipeline: 1) registration of the CLARITY two-photon microscopy images to the structural MRI of the LLP4 slab; 2) registration between the whole-brain Stanford University monkey and the NIMH whole-brain monkey, as well as registration between the Duke atlas MRI monkey to the NIMH whole-brain monkey.

In case 1) literature [64] report that during the CLARITY pipeline the sample increase two times in size, and then during the imaging when the sample is immersed in an imaging solution, the sample shrink to approximately the original size. No quantitative study of the

### **Chapter 3. Towards 3D histological validation of DW-MRI fiber orientation**

---

amount of deformation has been done previously. We did not explore the benefits of using non-linear registration because of the small size of the comparison image (10x10x1 voxels). More specifically, the simple geometry of the interface between GM and WM, the main discriminant that can be used to register the sample, do not provide enough information to acknowledge the use of non-linear registration. However, for a more prominent portion of voxels comparison, we do not exclude that non-linear registration could help.

In case 2), for registration between different whole-brain monkeys, we studied the effect of non-linear registration; however, better results are found using linear registration.

#### **3.4.2 WM and GM fiber orientation comparisons**

Both the analysis performed with the structure tensor and sODF showed better agreement in GM and worst agreement in the WM. The differences in WM can be due to several reasons: 1) the neurofilament stain in the WM regions in the CLARITY images is very dense making the estimation of the structure tensor in that region difficult; 2) even if DW-MRI estimates FOD without crossing and fanning in WM, multiple bundle population may be present.

Furthermore, even if co-registration was done accurately, limits on different brain monkeys used is a compound, because the fiber orientation can be different for different monkey specimen in the tested region.

#### **3.4.3 CLARITY and microscopy imaging limitations**

The main advantages of CLARITY, as well as other hydrogel embedded methods, is that it has excellent clearing performance and compatibility with protein-based fluorophores.

The main disadvantage of CLARITY is that passive clearing is slow. Faster clearing requires high temperatures or custom electrophoresis equipment. Furthermore, although the tissue transparency has been attributed to the removal of lipids during the procedure, it is still unknown to what extent the lipids are cleared from the sample.

One of the significant challenges introduced by clarified tissue samples is imaging technology. Only a small sample was acquired, this because confocal and two-photon microscopy imaging techniques have a major limitation in the amount of time required to image a large sample. Better microscopy techniques are needed to increase the amount of data scanned.

### **3.5 Conclusion**

The primary goal of this work was to study if the tissue-clearing protocol can be adapted to a more larger portion of tissue on the primate brain, and both in GM and WM. More specifically, we performed CLARITY on a slab of monkey visual cortex of 1.5 cm x 1.5 cm x 0.3 cm size.

Previous work[118, 348] studied connections of the macaque visual system in detail. Here, we use CLARITY as a complementary tool which allows recovering information of fiber orientation in specific visual areas.

The second purpose of the study is to explore the accuracy of fiber orientation estimated with DW-MRI and compare estimations with the reconstruction achieved with CLARITY. To achieve this goal, we extend standard analysis performed using the tensors, suitable only for single-fiber populations, to more complex functions, which are commonly known as ODF, which are capable of capturing multiple fiber-populations in a voxel.

In general, validations strategies need multiple iterations and refinement [105], and our pipeline is not exempt from this aspect. Nevertheless, this work demonstrates one of the largest and highest quality CLARITY cuboids from a macaque brain and explores critical steps in the co-registration and analysis required to make a robust comparison against DW-MRI data. Our data suggest that CLARITY protocols may need to be adapted for staining of areas of different neurofilaments protein densities. Ultimately, tissue clearing techniques that offer visualization of 3D axons trajectories represent a new complementary imaging modality that can help validate DW-MRI methods.





## 4 Bundle-specific $T_2$ mapping of cortical pathways

At the typical spatial resolution of MRI, approximately 90% of voxels in the human brain contain multiple fiber populations.

Quantifying microstructural properties of distinct populations with a voxel is challenging. While progress has been made for diffusion and  $T_1$ -relaxation properties, resolving intra-voxel  $T_2$  heterogeneity remains an open question. In this chapter, we present a novel framework that utilizes tractography-based spatial regularization and diffusion-relaxometry data.

We demonstrate both in numerical simulations and in vivo that, unlike previously-proposed voxel-based methods, our framework can recover intra-axonal bundle-specific  $T_2$  values within a voxel solving  $T_2$  heterogeneity.

### 4.1 Introduction

DW-MRI is the primary technique for studying the microstructural organization of the brain's WM in vivo. Despite the nominal imaging resolution, typically in the order from 1 mm to 3 mm, being orders of magnitude larger than the tissue features at the cellular level, i.e., few micrometers, the technique is sensitive to the microscopic environment because the distance traveled by water molecules is similar to the cellular dimensions [41].

Several relevant models have been proposed in recent years to quantify the microstructure of white matter tissue, in which the diffusion processes taking place in the intra- and extra-axonal spaces are modeled differently [15, 34, 175, 189, 329, 371].

Distinctly, as noted by Assaf and Basser [15] in the original CHARMED model, the signal fractions assigned to the intra- and extra-axonal spaces are weighted according to their relative transverse relaxation  $T_2$  times, and therefore the relative weighting also depends on the experimental TE.

To obtain a complete characterization of the brain tissue microstructure it is crucial

to develop new DW-MRI models disentangling the volume fractions of the different tissue compartments from their relaxation times [32, 99].

### 4.1.1 $T_2$ Relaxation and suppression extra-axonal signal

Modern studies have proposed the integration of multimodal acquisition techniques and multi-compartment models to characterize distinct features of the tissue. More precisely, the acquisition of DW-MRI data using different TEs allowed estimating the  $T_2$  relaxation times of the different tissue compartments [35, 56, 82, 194, 199, 211, 227, 252, 281, 334, 353]. As hardware and software constraints limit the acquisition parameters in clinical scanners, most of the studies employed diffusion sequences with  $TE > 70$  ms. For such long TE, the signal coming from the myelin water is virtually zero (i.e., because the  $T_2$  of myelin water is around 10 ms to 30 ms) and thus only the intra- and extra-axonal compartments are considered [227].

### 4.1.2 Estimating $T_2$ in single population voxels

Following a history of development in the field of physical chemistry [220, 364] Veraart et al., [353] developed the TE dependent Diffusion Imaging (TedDI) framework to simultaneously estimate the intra- and extra-axonal water fractions and their absolute  $T_2$  values.

Other studies estimated the mean  $T_2$  of the intra-axonal compartment at each voxel by suppressing the extra-axonal signal by using b-value  $> 4000 \text{ s mm}^{-2}$  [174, 227, 228, 253, 351]. Interestingly, the  $T_2$  computed for various ROIs located in regions areas of different bundles with single fiber populations were similar within the tracts and different between tracts, which suggests that different bundles are characterized by different  $T_2$  times and that the  $T_2$  relaxation may be bundle-specific. Thus, in voxels with different bundles,  $T_2$  heterogeneity exists – but only the mean value of the ensemble of  $T_2$  values can be accessed. Given that 60-90% of brain voxels contain multiple fiber populations [179], a complete characterization of the tissue necessitates the development of new methods that can estimate the  $T_2$  of the constituent fibers.

There is a precedent for resolving fiber-specific relaxation properties within a voxel. De Santis et al. [85] developed a framework that combined inversion recovery and DW-MRI to assign a specific value of the longitudinal relaxation time  $T_1$  to each fiber population within a voxel. It was shown that this method resulted in less inter-subject variability compared to conventional voxel-by-voxel  $T_1$ -mapping methods in areas of crossing fibers, suggesting an increased specificity to distinct fiber populations.

### 4.1.3 Bundle-specific $T_2$

In this study, we use a similar acquisition protocol as McKinnon and Hensen [227] and propose an extension of the COMMIT framework [75–77], named COMMIT- $T_2$ . The COMMIT

framework has been extended previously in [303] and used to fit tractography to scalar maps simplifying. On the contrary, our formulation model tractography fully utilizing diffusion-relaxometry and adds the possibility to model the  $T_2$  and diffusion in a unique framework.

As the  $T_2$  value depends on the tissue microstructure and axonal bundles are structurally homogeneous in their composition (i.e., axons tend to group into fascicles of their type [85]), we assume that each bundle has a specific  $T_2$  value. Using a whole-brain tractography result as input, COMMIT- $T_2$  estimates the intra-axonal  $T_2$  value of each streamline, independently of the organizational complexity within the voxel. The fitting is based on a global optimization approach that estimates a  $T_2$  for every tractography streamline.

The framework was evaluated using numerical simulations and was applied to in vivo data. Furthermore, it was compared with voxel-based methods, including the direction-averaged method proposed in [227] and AMICO- $T_2$ , another new extension to the AMICO framework [73] that considers the DW-MRI dependence on  $T_2$ .

In this work, we demonstrate that our approach can detect differences in  $T_2$  between two commonly-studied fasciculi: the CC and the Posterior Limb Internal Capsule (PIC).

## 4.2 Methods

### 4.2.1 Generative model

The measured signal  $S(TE, b, \vec{r})$  for a given  $TE$ ,  $b$ -value, and diffusion gradient unit vector  $\vec{r}$  is given by:

$$S(TE, b, \vec{r}) = kPD \left( f_i e^{-\frac{TE}{T_2^i}} S_i(b, \vec{r}) + f_e e^{-\frac{TE}{T_2^e}} S_e(b, \vec{r}) \right), \quad (4.1)$$

where  $PD$  is the proton density;  $k$  is a factor of the MRI machine that depends of the MRI acquisition, including the pulse, image-reconstruction algorithm, and digital converter, etc;  $f_i$  and  $f_e$  denote the intra- and extra-axonal volume fractions;  $T_2^i$  and  $T_2^e$  are the  $T_2$  values of the intra- and extra-axonal compartments, and  $S_i$  and  $S_e$  denote the diffusion-weighted signals from the intra- and extra-axonal compartments, respectively. An experimental TR higher than 4 s is assumed to suppress  $T_1$  effects.

As in [227],  $S_e \approx 0$  for  $b$ -value = 6000 s mm<sup>-2</sup> and 48 directions [124, 174, 227, 228, 253] and Eq.(4.1) becomes:

$$S(TE, b, \vec{r}) = C e^{-\frac{TE}{T_2^i}} S_i(b, \vec{r}), \quad (4.2)$$

where  $C = kPD f_i$ . The estimation of the  $T_2^i$  values was implemented using three different

approaches: 1) the direction-averaged technique proposed in [227], 2) AMICO- $T_2$ , and 3) COMMIT- $T_2$ . Technical details are provided in the next sections.

### 4.2.2 Direction-averaged technique

By following an approach similar to the one introduced in the SMT [189], Eq. (4.2) can be simplified by computing the direction-averaged DW-MRI signal  $\overline{S}(TE, b) = \langle S(TE, b, \vec{r}) \rangle$  [227]:

$$\overline{S}(TE, b) = Ae^{\frac{-TE}{T_2 i}}, \quad (4.3)$$

where  $A = C \langle S_i(b, \vec{r}) \rangle = C \overline{S}_i(b)$ . After taking the logarithm in both sides, Eq. (4.3) reduces to a linear problem from which  $T_2 i$  can be estimated [227].

### 4.2.3 Voxel-wise formulation: AMICO- $T_2$

The conventional AMICO framework [73] is based on solving the following equation for each voxel:

$$\mathbf{y} = \mathbf{A}\mathbf{x} + \boldsymbol{\eta}, \quad (4.4)$$

where  $\mathbf{y}$  is the vector of measurements,  $\mathbf{A}$  is the dictionary or design matrix,  $\boldsymbol{\eta}$  denotes the vector of noise, and  $\mathbf{x}$  is the vector of coefficients to be estimated: each element in  $\mathbf{x}$  contains the weight that quantifies the contribution of the corresponding column/atom in  $\mathbf{A}$  to explain the measurements.

In this study, matrix  $\mathbf{A}$  was built using a generative model that takes into account the signal dependence on  $T_2$ . Specifically, each element of  $\mathbf{A}$  was obtained by evaluating the model given by Eq. (4.2),  $A_{j,k} = e^{\frac{-TE_j}{T_2 i_k}} S_i(\mathbf{b}_j, \vec{r}_j)$ , where  $TE_j$ ,  $\mathbf{b}_j$ , and  $\vec{r}_j$  are the experimental values used to acquire the  $j$ -th measurement (i.e.,  $y_j$ ), and  $T_2 i_k$  is the  $k$ -th value from a set of predefined  $T_2 i$  times. Specifically, the dictionary was built using 20 equally-spaced  $T_2 i$  values in the range 40 ms to 135 ms and  $S_i$  was evaluated using the "Stick" model [34, 175]. This degenerated diffusion tensor model assumes that the intra-axonal perpendicular diffusivity  $D_{i\perp}$  is equal to 0. Given the known problem of degeneracy in solutions when trying to estimate parameters, we chose to fix  $D_{i\parallel} = 2 \times 10^{-3} \text{ mm}^2 \text{ s}^{-1}$  [96] to ameliorate the degeneracy problem. Before evaluating  $S_i$ , the main eigenvector was calculated using the standard diffusion tensor model.

The vector of coefficients was estimated using a non-negative least square (NNLS) algorithm:

$$\hat{\mathbf{x}} = \underset{\mathbf{x} \geq 0}{\operatorname{argmin}} \|\mathbf{A}\mathbf{x} - \mathbf{y}\|_2^2, \quad (4.5)$$

and the average  $T_2i$  was calculated for each voxel as the weighted mean:

$$T_2i = \frac{\sum_{j=1}^{20} \hat{x}_j T_2i_j}{\sum_{j=1}^{20} \hat{x}_j}. \quad (4.6)$$

#### 4.2.4 COMMIT- $T_2$

The conventional COMMIT framework [76, 77] models the DW-MRI signal in each voxel of the image as a linear combination of the intra- and extra-axonal signals generated in every location of the brain by using a set of candidate tracts, which are estimated using standard fiber-tracking techniques. Then, COMMIT estimates the effective contribution or weight of each of them, such that they globally fit the measured signal. These weights are estimated by solving a global convex optimization problem. In practice, COMMIT creates a large linear system of equations by concatenating the vectors of measurements from all brain voxels and corresponding dictionaries. Notably, each individual dictionary column is not associated with a voxel, but to a specific fiber bundle. For more details, see [76, 77].

In this work, COMMIT is modified to allow for tract-based  $T_2i$  estimation by using the generative model given in Eq. (4.2). COMMIT- $T_2$  assumes that  $T_2i$  remains constant along the tracts trajectories. Specifically, the same model's parameters used in AMICO- $T_2$  were employed (i.e.,  $D_{i\perp}$ ,  $D_{i\parallel}$ , and predefined set of  $T_2i$  values). After solving the resulting global regression problem using a large-scale Non-Negative Least Square (NNLS) solver [77], a vector of coefficients  $x$  for each fiber bundle is obtained, where the  $k$ -th element  $x_k$  quantifies the signal fraction explained by that fiber bundle with a predefined  $T_2i_k$  value. Thus, a distribution of  $T_2i$  values is obtained for each bundle, which mean value is computed using Eq. (4.6). To compare this tract-based estimation method with the voxel-based approaches described in previous sections, the resulting mean  $T_2i$  values from multiple streamlines were averaged and projected at each voxel.

The starting input set of candidates fibers was estimated using the CSD method [344] and the deterministic SD\_STREAM fiber tracking algorithm included in the MRTrix3 software (<http://www.mrtrix.org>). The reconstruction was carried out using default parameters. About 150K streamlines were obtained, and those ending in the WM were filtered out.

#### 4.2.5 Protocol

The protocol is divided in two parts: tractography and intra-axonal  $T_2$  estimates. For all data,  $\delta$  8 ms and  $\Delta$  = 22 ms were fixed. The tractography protocol uses 6 b-value = 0  $\text{s mm}^{-2}$ , 8 directions at b-value = 750  $\text{s mm}^{-2}$  and 30 directions at b-value = 3000  $\text{s mm}^{-2}$  with TE= 45 ms. For the  $T_2$  estimations part 4 b-value = 0  $\text{s mm}^{-2}$ , 8 directions at b-value = 750  $\text{s mm}^{-2}$  and 48

directions at b-value =  $6000 \text{ s mm}^{-2}$  with TE= 73 ms, 93 ms, 118 ms and 150 ms.

The b-value =  $0 \text{ s mm}^{-2}$  and b-value =  $750 \text{ s mm}^{-2}$  data were used for the preprocessing steps for the in vivo data.

### 4.2.6 Numerical simulations

A fiber crossing phantom was drawn in Blender [Blender Online Community] and the fibers coordinates were saved in '.obj' file format. This file was then converted to '.trk' format to be read by COMMIT (<https://github.com/daducci/COMMIT>), which was used to generate the DW-MRI synthetic data.

The DW-MRI signals were generated by using the model given by Eq. 4.2 with the acquisition parameters described in section 4.2.5 and the following model's parameters: bundle1)  $T_{2b1} = 78 \text{ ms}$ , bundle2)  $T_{2b2} = 116 \text{ ms}$ . Each streamline contributed with  $f_i s = 0.0071$  in order to achieve  $\max(S) = 1$ . The diffusivities in both tracts were fixed to  $D_{i\perp} = 0$  and  $D_{i\parallel} = 2 \times 10^{-3} \text{ mm}^2 \text{ s}^{-1}$ .

A second experiment performed was to evaluate the sensitivity of the methods varying  $T_2$  values per bundle. In this case we generated numerical phantoms of the crossing fixing  $T_{2b1} = 78 \text{ ms}$  and varying  $T_{2b2}$  from 40 ms to 135 ms with 41 values equally-spaced.

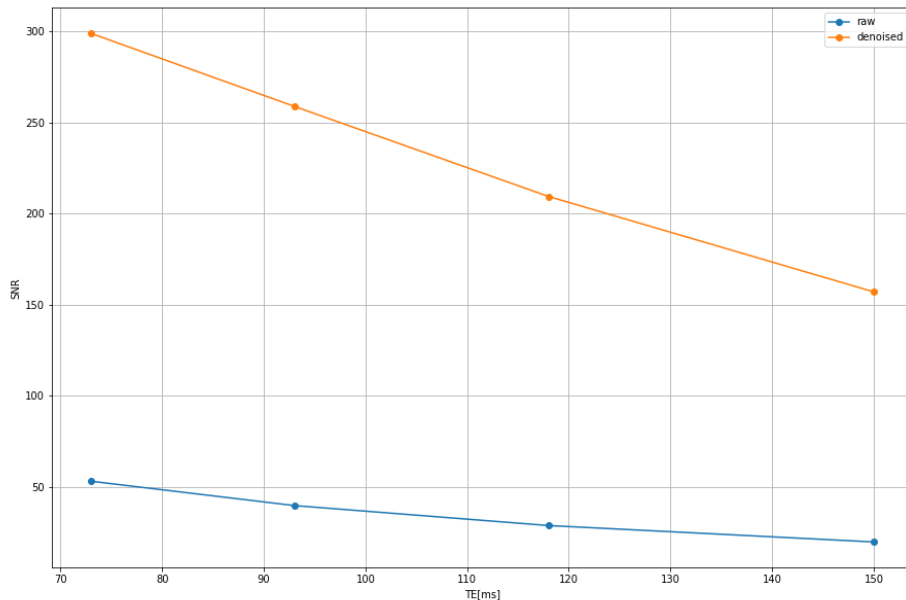


Figure 4.1 – Noise level estimation on raw data and after denoising.

The resulting datasets were corrupted with noise using a noise level similar to that obtained in real data, which was determined after applying the denoising algorithm developed in [352]. For more details see section 4.2.7 and the figure 4.1.

#### 4.2.7 In vivo data acquisition and preprocessing

DW-MRI data were acquired using the Siemens Connectom 3T MRI scanner with  $300 \text{ mT m}^{-1}$  gradients. One healthy human volunteer was scanned within a single imaging session using the acquisition parameters described in section 4.2.5. The study was approved by the local ethics committee and the participant provided written informed consent. Other imaging parameters are: TR = 4100 ms, voxel size = 2.5 mm isotropic, number of slices = 46, acquisition matrix =  $88 \times 88$ . One image with  $b = 0$  and opposite phase encoding direction were also acquired. Additionally, a structural  $T_1$  image was collected using a 3D magnetization-prepared rapid acquisition gradient echo (MPRAGE) sequence with the following parameters: TR = 2300 ms, TE = 2 ms, Inversion Time (IT) = 857 ms, voxel size = 1 mm isotropic, acquisition matrix =  $256 \times 256$ , flip angle=9 degree, and scan time=5:32min.

The preprocessing steps were applied in the following order: 1) noise level estimation and removal [352], 2) Rician unbiasing [190], 3) removal of Gibbs ringing artifacts [192] and 4) motion and geometric distortion corrections using the "topup" and "eddy" tools included in FSL [172]. In order to compensate for motion between the different scan-sets, all data with different TE were preprocessed separately and then co-registered all together using a rigid registration [195]. The registration was done based on the images without diffusion weighting, i.e.,  $b\text{-value} = 0 \text{ s mm}^{-2}$ . Finally, the  $T_1$  image was parcellated with FreeSurfer [79] and the extraction of the different bundles was carried out with the White Matter Query Language (WMQL) [359].

### 4.3 Results

#### 4.3.1 Numerical simulations

Figure 4.2 shows the  $T_2i$  values estimated in the numerical phantom described in section 4.2.6 using the direction-averaged, AMICO- $T_2$  and COMMIT- $T_2$  methods. This result was obtained using the noiseless data. The first column depicts the two bundles with ground truth values of  $T_{2b1} = 78 \text{ ms}$  and  $T_{2b2} = 116 \text{ ms}$ , respectively. The analysis was done separately on voxels with a single and multiple fiber populations. In voxels with a single fiber, the three methods recovered the ground truth values. In contrast, in regions with fiber crossings, the  $T_2i$  values estimated by the voxel-based methods (i.e., the direction-average technique and AMICO- $T_2$ ) are in between the two ground truth  $T_{2b1}$  and  $T_{2b2}$  values. Notably, COMMIT- $T_2$  correctly estimated the  $T_2i$  values in both bundles in the fiber crossing region. This was possible thanks to the spatial regularization naturally enforced by the fiber tracts.

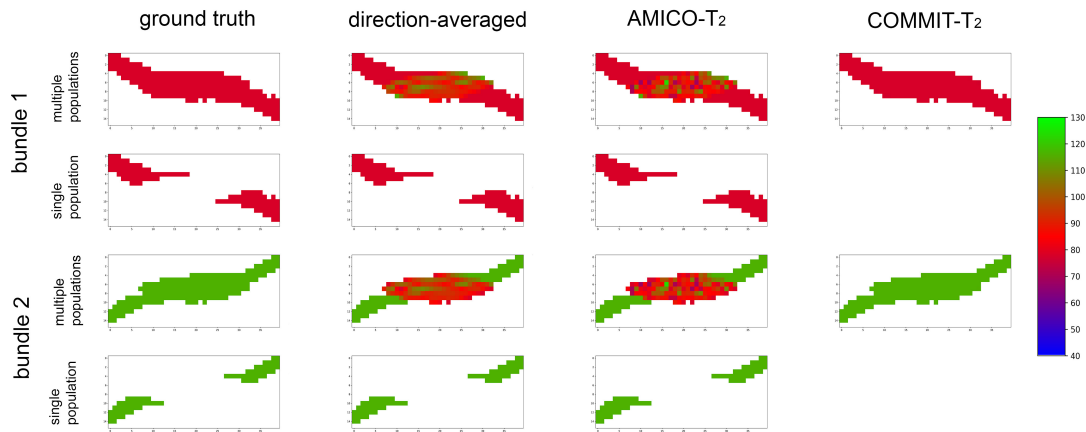


Figure 4.2 – A cross-section of the synthetic phantom is visualized. The phantom simulates a crossing of two fiber bundles with different  $T_2i$  values of  $T_{2b1} = 78$  ms (in red color) and  $T_{2b2} = 116$  ms (in green color), respectively. Voxels with a single and two fibers were differentiated to test the performance of the three evaluated methods: the direction-averaged technique, AMICO- $T_2$ , and COMMIT- $T_2$ .

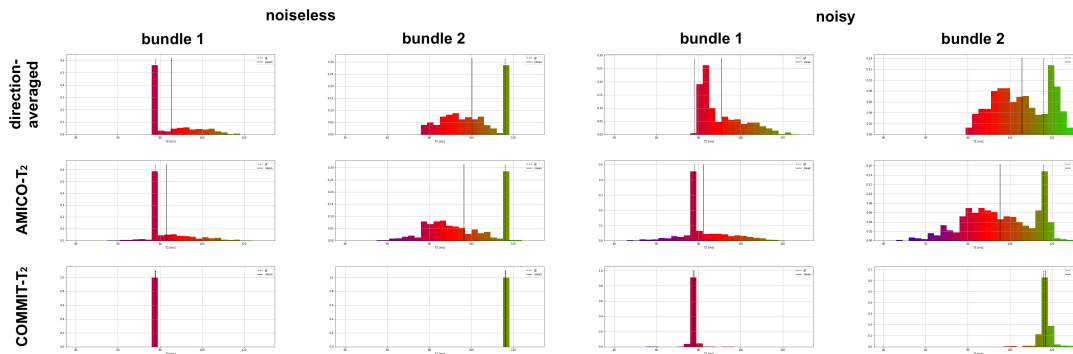


Figure 4.3 – Histograms of the  $T_2i$  values estimated in the phantom using the three evaluated methods: the direction-averaged technique, AMICO- $T_2$ , and COMMIT- $T_2$ . For more details see Figure 4.2. Results from both the noiseless and noisy datasets are reported.

The histograms of the  $T_2i$  values obtained from both the noiseless and noisy datasets are shown in Fig. 4.3. The direction-averaged technique tends to overestimate, even in the case of single bundle population, where AMICO- $T_2$  has a peak on the ground truth value; thus, although neither method addresses the crossing fiber problem directly, AMICO- $T_2$  seems more robust to noise compared to the direction-averaged method. COMMIT- $T_2$ , instead, does a good job of recovering the correct ground truth values and is more robust to noise.

### 4.3.2 Sensitivity analysis

Figure 4.4 shows the plot of the mean value of the bundle 2. For direction-averaged and AMICO- $T_2$  noiseless single bundle population, the methods are recovering the GT values.



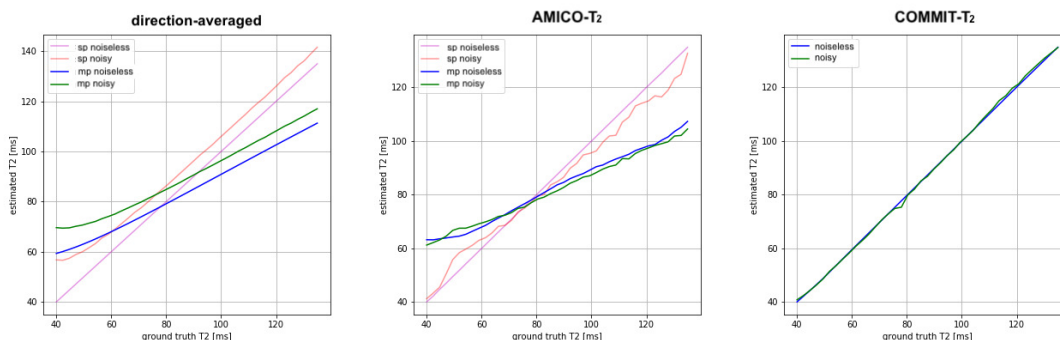


Figure 4.4 – Comparison of  $T_2$  estimation against ground truth for the direction-averaged, AMICO- $T_2$  and COMMIT- $T_2$  methods.

The noise makes the direction-averaged overestimating, wherein AMICO- $T_2$  a clear pattern is less clear. In the voxel-based analysis of multiple bundles, even in the noiseless case, the expected overestimation for values lower than 78 ms and underestimation for values higher is found. COMMIT- $T_2$  recovers the correct  $T_2$  values at the variation of the  $T_{2b2}$ , showing high sensitivity; moreover, the effect of noise is minimal.

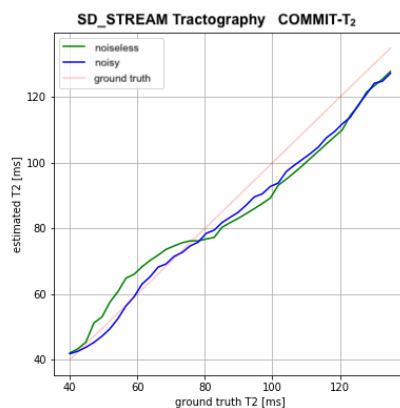


Figure 4.5 – Sensitivity analysis on the crossing phantom performed with COMMIT- $T_2$  where a new *SD\_STREAM* tractography is generated. The study is performed in the noiseless and noisy cases.

One possible reason for COMMIT- $T_2$  outperforming the other methods is that the tracking algorithm used in the signal fitting is the same used to generate the phantom data, warranting the investigation of performance with different tracking algorithms. CSD was performed on the numerical phantom using the *SD\_STREAM* algorithm from MRTrix3 [344] with 10K streamlines. The new tractography generated around 50% of false positive connections, which were removed manually by region of interest in the endpoints and filter the tractography remaining with the two correct bundles. This because in this study, there is no aim to explore the removal of false positive by COMMIT- $T_2$ .

## Chapter 4. Bundle-specific $T_2$ mapping of cortical pathways

The results of the experiment are shown in figure 4.5; COMMIT- $T_2$  can recover values robustly, both in the noiseless and noisy case, showing that the variance due to tractography is minimal.

### 4.3.3 In vivo results

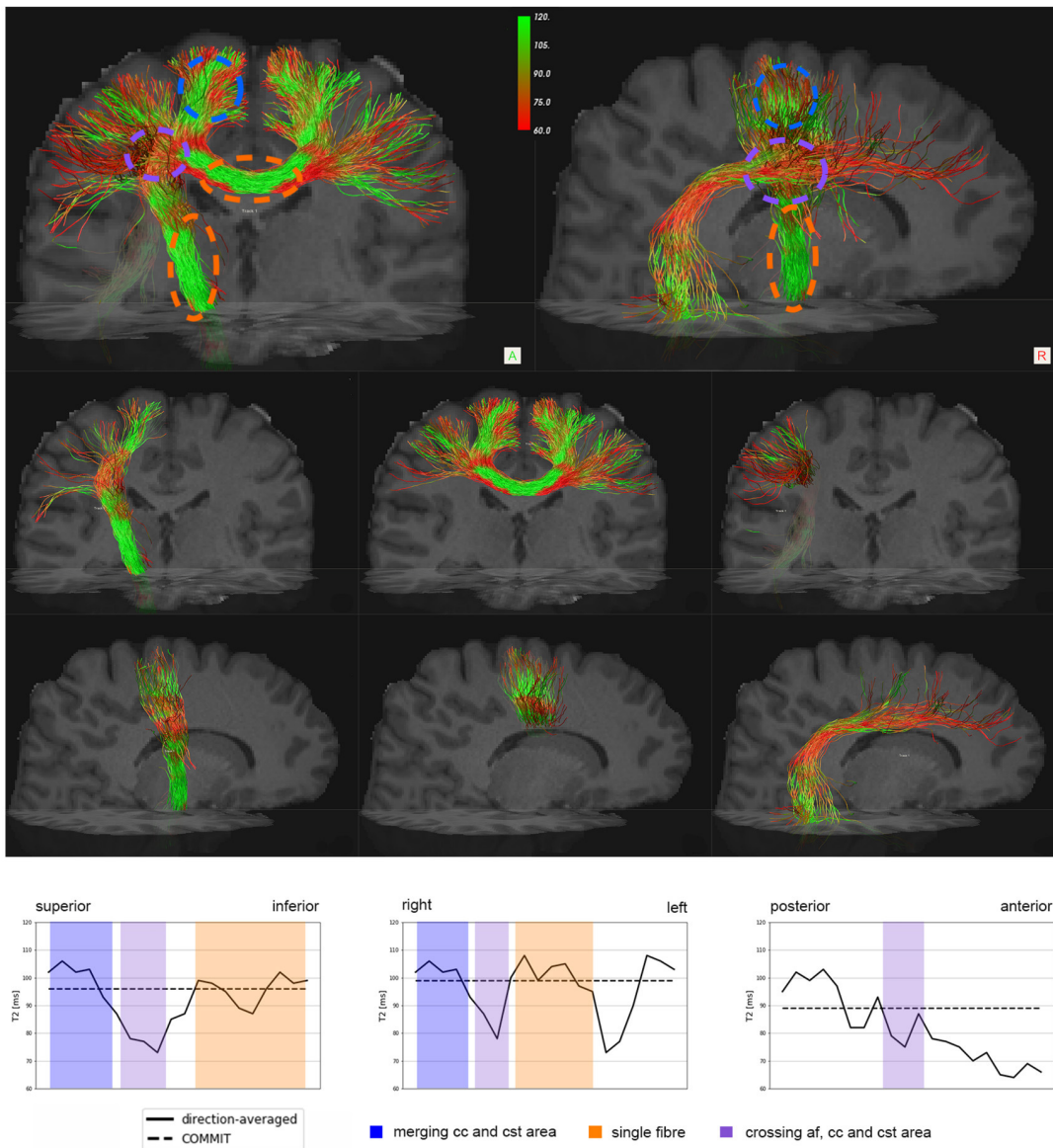


Figure 4.6 – Tractometry using  $T_2$  values estimated with the direction-averaged technique. A portion of Corpus Callosum, Corticospinal tract and Arcatue Fasciculus is shown with streamlines colored by  $T_2$  estimation. Below, we show the profile of the changing of  $T_2$  along the bundles.

In figure 4.6 we highlight three bundles, portion of CC, portion of CST and AF. We show

how using direction-averaged methods the values along the bundles show high variation. Especially in the three bundle crossing area of the CC, CST and AF we see a drop of  $T_2$  for the CC and CST. This can be caused by the overall lower  $T_2$  values of the AF.

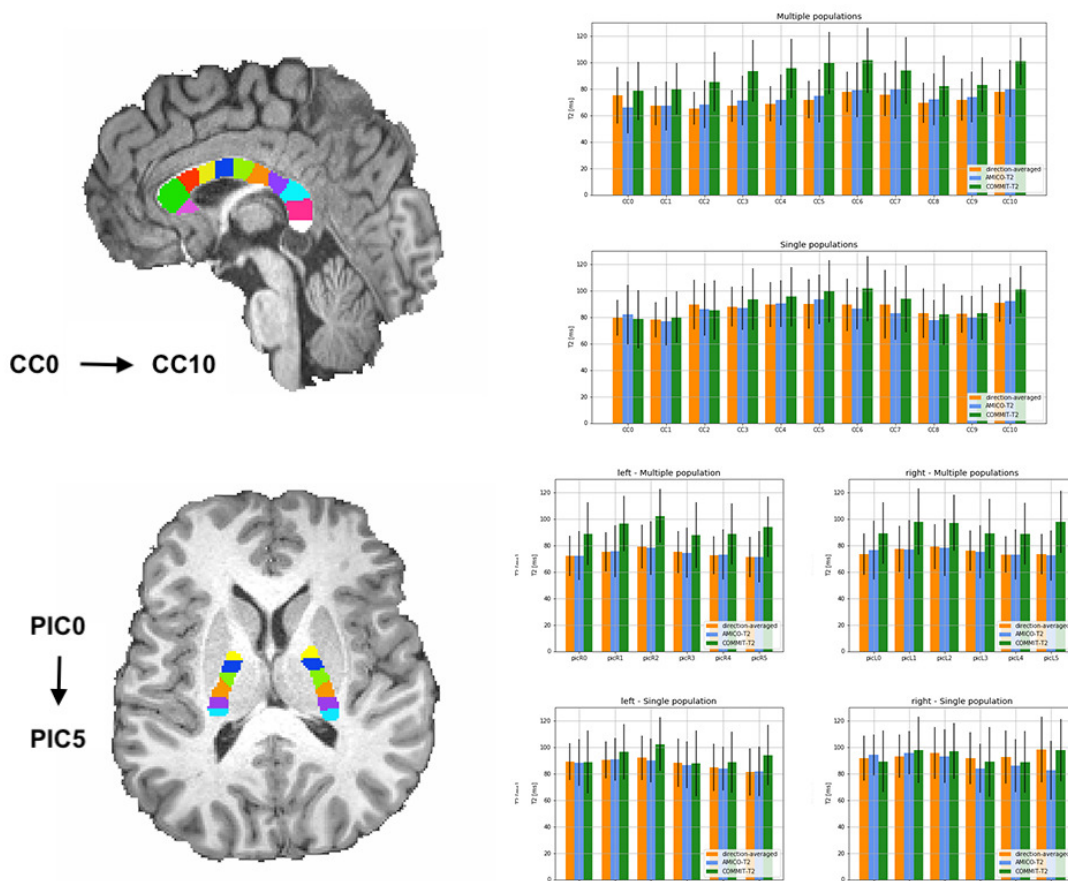


Figure 4.7 –  $T_2$  estimations using the direction-averaged, AMICO- $T_2$  and COMMIT- $T_2$ . The analysis is performed on three well-known bundles in the brain: Corpus Callosum (CC) and Posterior limb Internal Capsule (PIC) of the left and right hemisphere. The CC was subdivided in 11 equally distant different ROIs, while the PICs are subdivided in 6 ROIs. Comparison is performed considering the average along all voxels where the bundle is defined, where multiple population was occurred, and voxel where only one population is presented (defined as threshold of the Fractional Anisotropy (FA) map at 0.7).

Furthermore, it is interesting to examine the  $T_2$  estimates in well-known anatomical bundles in order to correlate results to microstructural knowledge. In this study, we analyzed in detail two well-known bundles, CC and PIC, left and right hemisphere. The CC was divided into 11 ROIs and the two PIC in 6 ROIs, and analysis of  $T_2$  bundle-specific estimate was performed, figure 4.8.

The results of the CC show that the voxel-based methods are recovering  $T_2$  around 20 ms lower compare to the COMMIT- $T_2$ . Furthermore, the  $T_2$  estimation of the bundles was performed in single bundle voxels thresholding the FA at 0.7. Results show that direction-

## Chapter 4. Bundle-specific $T_2$ mapping of cortical pathways

averaged and AMICO- $T_2$  recover similar values to COMMIT- $T_2$ . This outcome confirms in real data that the voxel-based methods proposed, differently from COMMIT- $T_2$  cannot solve complex configuration.

More in detail, we explored the variation of  $T_2$  along the CC and the PIC. In the CC we can define a pattern low-high-low-high. Lower values are associated to  $T_2$  around 80 ms, while higher values are associated to  $T_2$  around 100 ms. In our subdivision CC5, CC6 and CC10, which correspond to regions of bundles ending in motor, somatosensory cortex and visual area, have considerably higher  $T_2$ . In the PIC left and right, we find higher  $T_2$ , above 90 ms in the PIC1, PIC2, and PIC5; both left and right hemispheres seem to have a similar pattern.

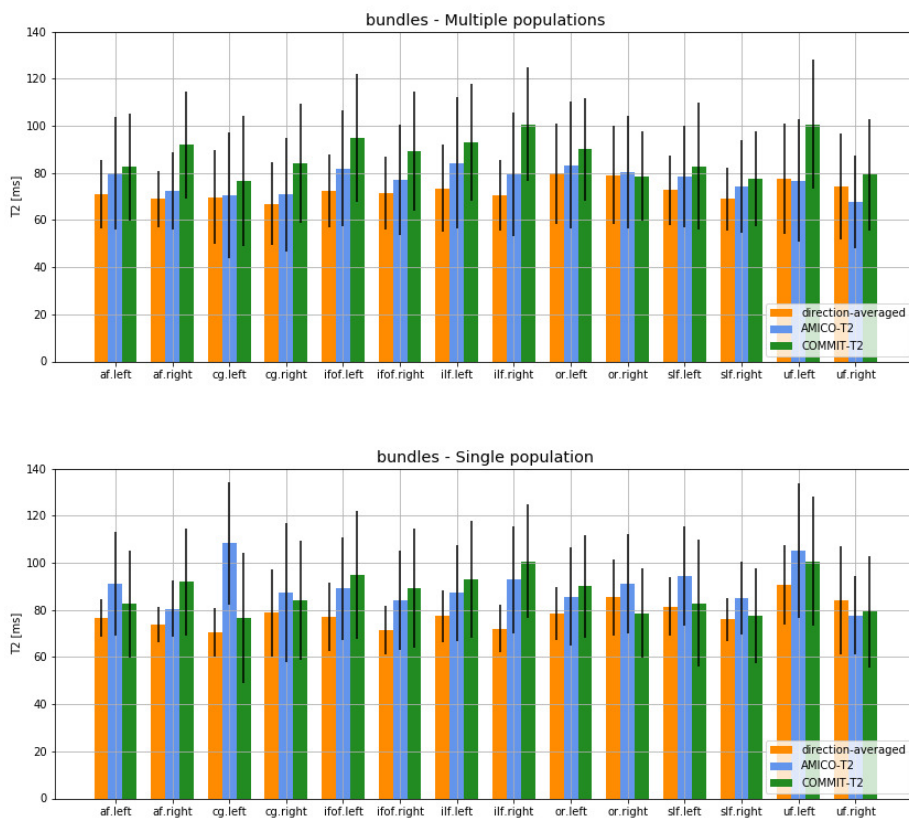


Figure 4.8 –  $T_2$  estimations using the direction-averaged, AMICO- $T_2$  and COMMIT- $T_2$ . The analysis is performed on the arcuate fasciculus (AF), the cingulum (CG), the inferior fronto-occipital fasciculus (IFOF), the inferior longitudinal fasciculus (SLF), the optic radiation (OR), the superior longitudinal fasciculus (SLF), and the uncinate fasciculus (UF). Comparison is performed considering the average along all voxels where the bundle is defined, where multiple populations occurred, and voxel where only one population is presented (defined as threshold of the fractional anisotropy (FA) map at 0.7).

In figure 4.8 we report the results of the comparison of single and multiple voxel populations in other geometrical well-known bundles in the brain: the AF, the Cg, the IFOF, the

SLF, the Optic Radiation (OR), the SLF, and the UF. The analysis was performed on both hemispheres.

Results of COMMIT- $T_2$  are showing similar results for left and right hemisphere, except for the UF, where higher  $T_2$ , around 100 ms is found in the left hemisphere while lower values are found on the right hemisphere 80 ms. We highlight that when voxel considers only a single bundle population higher is the  $T_2$  estimated, compared to when also multiple bundle voxels are considered.

## 4.4 Discussion

In this work, we explored the feasibility to estimate intra-axonal  $T_2$  in tracts with complex geometry, i.e., crossing, fanning, and merging; and we propose the COMMIT- $T_2$  framework. To achieve these results, we used only high b-value, where the extra-axonal signal can be neglected.

The origin of different  $T_2$  is not known. However, it is known that different tissue microstructure experience different  $T_2$ , and previous work mainly focused on the disentangling of intra-axonal and extra-axonal component [56, 281, 334, 353]. Some work went further and proposed a possible subdivision of intra-axonal  $T_2$  components in different bundles [227, 353].

All previous studies focused on a model for a single bundle population which can be applied in limited regions of the human brain. It is desirable to obtain of  $T_2$  estimates in multiple population voxels. Hence, we proposed the COMMIT- $T_2$ , the first framework able to disentangle  $T_2$  estimates of different bundles thanks to spatial regularization derived from tractography.

The novel approach was compared to two voxel-based methods, the direction-averaged proposed by [227] and another novel approach which we implemented and named AMICO- $T_2$ .

AMICO- $T_2$ , as COMMIT- $T_2$  are dictionary approaches which are extensions respectively of AMICO [73] and COMMIT [76, 77]. The original implementation of AMICO and COMMIT frameworks used two different computational solvers to solve the non-negative least square, respectively, an active set and gradient descent solver. Gradient descent solvers are slower compared to the active set; however, they do not require storage of the matrix  $A$  in-memory RAM, which for the complexity of the COMMIT global problem is not feasible. In order to have a fair comparison between AMICO and COMMIT and avoid variability dependent on the solver, we implemented the gradient descent solver in AMICO. We report that for the protocol used, for relative tolerance lower than  $10^{-6}$ , the two solvers reach to the same solution.

We also can compare the two voxel-based methods. The comparison showed similar results between the two. From a theoretical perspective, the main difference between the two is that the direction-averaged method handle bundle dispersion, while in AMICO- $T_2$  the model does not account for dispersion. Nevertheless, the two voxel-based methods, when

applied on in vivo data, did not show relevant variation between them.

In terms of robustness to noise on numerical simulations, our findings show that dictionary-based methods seem more robust to noise compared to the direction-averaged method, in which we find constant overestimation of the  $T_2$  estimates.

One of the main limitations that can be attributed to the method is the fact that the model assumes constant properties along the tract trajectories. Changes of axonal properties have been reported at the micro-scale level, however at long scale connection and for resolution used it is conventional thinking that it is not a strong approximation [276, 316, 317, 320, 321].

Another critical limitation is related to the limits of tractography [221, 307] and of the FOD estimated per voxel [57]. To address this issue, we mainly focus on well-known bundles, where we assume false positive is minimal. However, it is of interest to analyze the whole brain  $T_2$  connectivity matrix, which we will address in future works.

Future approaches could be used to improve tractography, and consequently recover more reliable estimates of bundle-specific  $T_2$  [292, 302].

Future works will address the possibility to extend the model for extra-cellular  $T_2$  estimation and perhaps even myelin [240].

From the application perspective it is essential to highlight that this new contrast could potential bring more benefits to find useful contrast in longitudinal studies, in developmental, aging, early studies of decease, and pathological processes or bring anatomical landmarks to describe different areas of a bundle, for example in the CC as shown in 4.8.

Moreover, this work did not aim to optimize a protocol, which was addressed in parallel recent studies [160].

## 4.5 Conclusion

In this chapter, we proposed a novel framework that uses tractography-based spatial regularization with diffusion-relaxometry data. We demonstrate both in numerical simulations and in vivo that, unlike previously-proposed voxel-based methods, our framework can recover intra-axonal bundle-specific  $T_2$  values within a voxel solving  $T_2$  heterogeneity. Furthermore, our finding shows that different bundles in the human brain report different  $T_2$  values, opening up the new opportunity to characterize bundles based on  $T_2$  relaxation.

# 5 Bundle-specific axon diameter mapping of cortical pathways

In the central nervous system of non-human primates, several pathways are characterized by different spectra of axon diameters. It is desirable to obtain similar information in live humans where axon diameters are affected by different pathologies and probably by individual skills.

In vivo methods based on DW-MRI are available, but can only provide such estimates in few and very selective locations along the course of axonal bundles, and are limited by the power of the scanners used.

In this chapter, we propose a novel method for microstructure informed tractography based on recent advances in MRI scanners applying ultra-strong gradients. This novel approach allows characterizing the composition of central nervous system pathways, in vivo and in humans, at a level of resolution compatible with the investigation of differences between healthy and exceptional brains.

## 5.1 Introduction

The WM of the CNS consists of axons with different diameters [2, 55, 146, 163, 164, 166, 277] organized in pathways, tracts, bundles or fascicles. Diameters correlate with i) the size of the parent cell body [336], ii) the size and density of synaptic boutons [162], iii) conduction velocity [158], which together with axon length determines conduction delays between brain sites; and possibly, iv) the frequency of firing [273]. All these different aspects, strictly related to diameters, may play a crucial role in understanding sensory, motor, and cognitive functions. Moreover, diameter estimation is of utter importance for interpreting pathological cases [90, 157, 374].

In the early stages of DW-MRI, the technique was mainly used to recover the coefficient of the impedance of water molecule diffusion [122], see chapter 1 for more details. Then, researchers have focused on estimating diffusion profiles to estimation the local orientation of the fiber, fundamental to reconstruct the pathways fascicles in the brain with tractography

## Chapter 5. Bundle-specific axon diameter mapping of cortical pathways

---

[26, 33, 66, 93, 170, 238], see chapter 1.5 for more details.

Following the development of the MRI scanners, new tools were developed to study features going beyond the local orientation of the white matter structure [4, 5, 14, 15, 72, 73, 88, 121, 156, 185, 190, 264, 268, 286, 287, 301, 369–371], see chapter 1.4. Nowadays, we can report that the DW-MRI community furnished useful tools to recover different axonal features [4], e.g., density, cell shape, and diameter.

In this chapter, we focus specifically on axon diameter, as it may be the key feature that will finally allowing the relation between structural and functional connections in the brain to be solved [154].

The axon diameter is known to be related to conduction velocity [127, 153, 155, 273, 294]; hence, it is associated with the flow of information from the different regions of the brain. Diameter estimation could potentially help to find the specific behavior and function of a bundle of neurons [368]. Finally, it is used and will be used more in the future, in the diagnosis of different neurological diseases, e.g., multiple sclerosis [147, 157].

Three decades ago, MRI was not ready to estimate such a feature in the brain; axon diameter was initially estimated *ex vivo* using electron microscopy. Initial studies were performed in the peripheral nervous system [137, 226, 311] for then move to the central nervous system [2, 54, 166, 198, 217]. Remarkably, histological studies reported similar trends of axon diameter in similar regions across different species, from monkey to human. In particular, the findings revealed a systematic trend in the CC, the region of the brain involved in interhemispheric functional connectivity [295]. From Genu to Midbody it is found a trend of axons that goes from small to big, to end in the Splenium with a distribution of small axons and very at the end of the Splenium there is part of higher axons connecting to the visual area. Furthermore, large axons are also found in the portion of the CST that end in motor areas. These histological findings have been used as a reference for most of the studies done with MRI.

The first theoretical model that tried to model pores of different size was done in NMR [248]; applications can be found in the context of oil research [266], food science [53] and in skeletal muscles [350]. Lately, with the development and improvements of the MRI, researchers focused on the human neuronal tissue measuring the axon diameter using DW-MRI[13].

The first attempt to estimate the axon diameter was proposed with AxCaliber [14, 15]. In the study, Assaf et al. used a method to map the axon diameter on an *ex vivo* spinal cord with a technique that fit gamma distribution. Later, the technique was for the first time applied on the CC *in vivo* rat brains with [25].

Initial studies with AxCaliber were done in the spinal cord [102, 103] and only recently with the development of the CONNECTOM scanner, with a maximum gradient of 300mT/m, the approach was applied on the CC *in vivo* human brain [156, 229, 314].

However, the major limitation of AxCaliber is that the signal needs to be acquired perpen-



dicular to the axons and in single bundle population. An attempt to solve such limitations was proposed with AxCaliber 3D [72]. Furthermore, from histological estimates it seems that imposing a gamma distribution is not the optimal solution to recover the axon diameter distribution [267, 313].

To overcome previous limitations, different approaches focused on estimating the mean axon diameter or the ADI instead of the full distribution. One of the first studies was performed by [260] using Q-space imaging in the spinal cord [259, 260]. Later, when was proposed the ActiveAx model [5], which could be applied directly in the human brain, the ADI became more popular. ActiveAx does not impose a gamma distribution. Furthermore, after the first proof of concept on in vivo data was [5] was also used and validated on the CC on monkey ex vivo material [104]. Attempts to extend the original formulation to include crossing fibers [369] and dispersion [370] were performed but did not achieve popularity among the community.

These two approaches, AxCaliber and ActiveAx, used both non-linear optimization algorithms, which are computationally expensive and prone to local minima. To overcome such limitations, AMICO was proposed as a framework to accelerate the ActiveAx model with a convex linear formulation [16, 77].

More recently, new approaches to estimate the axon diameter were proposed. In particular estimation of axon diameter with non-convex regression method [115], non-parametric mapping of the distribution [36] and machine learning [120, 247] seems to be promising works. Furthermore, a method to improves tractography having estimates of ADI was proposed in [138].

Estimation of axon diameter by DW-MRI has limitations [6, 249], Work has been done, and is in the process, to improve sequences protocols to find better contrast [101, 191, 233, 255]. Furthermore, more advanced modeling using e.g., time-dependence [46, 123, 299], was demonstrated to improve in the axon diameter estimation.

The method proposed in the literature focused mainly on regions where the axons are parallel. Only a few unsuccessful attempts on complex regions were proposed to study the axon diameter of more complex geometries.

All the methods mentioned above are based on local voxel estimations; hence, estimation is performed voxel by voxel independently. However, the main disadvantage is that local methods hardly solve the problem of crossing, dispersion, and undulation [250].

To overcome the limitations of existing methods, we propose for the first time a framework that uses tractography to estimate the axon diameters distribution globally. We propose tractography as implicit regularization to solve the problem of estimating diameter in regions of fiber crossing, dispersion, and undulation.

## 5.2 Methods

### 5.2.1 Axon diameter signatures

In this work, we extended the COMMIT framework using the Cylinder-Zeppelin and Ball model [5] to estimate the fiber composition. The COMMIT framework is schematically summarized in Figure 5.1, for more detail on the implementation see section 1.6. We then grouped streamlines sharing the same anatomical pathways in bundles defined from the cortical parcellation.

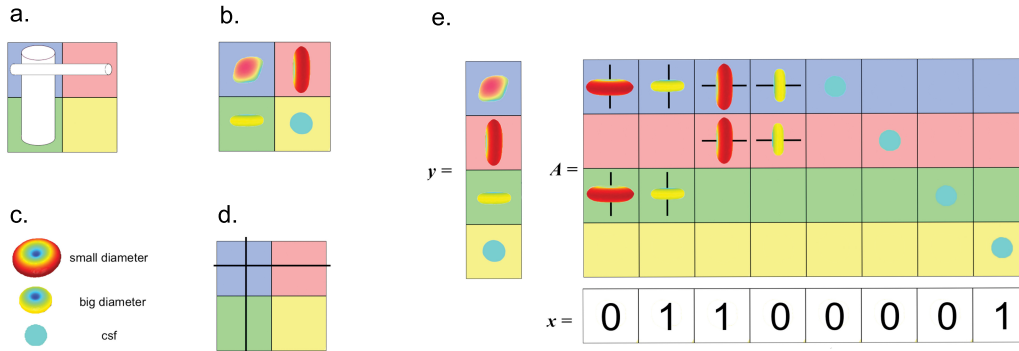


Figure 5.1 – The COMMIT framework. (a) Crossing configuration of cylinders with different diameter. Colors are associated with distinct voxels. (b) DW-MRI acquisition of the crossing configuration. (c,d) two main branches of tools able to process the DW-MRI signal: microstructure imaging, quantitative local estimation of tissue environment, i.e., axonal diameter; tractography, global estimation of trajectories, i.e., bundles. (e) COMMIT framework: unified expression of microstructure and tractography.  $y$ : DW-MRI signal acquired;  $A$ : matrix, express the model that integrates microstructure and tractography.  $x$ : volume fractions derived after the fitting.

The proposed method considers each streamlines as consisting of distinct axon populations having different diameters the amount of which must be estimated. Hence, several contributions are associated with each streamline reconstructed by tractography. The estimated coefficients  $\mathbf{x}$  (eq. 1.30) of a given streamline represent its volume-weighted axon diameter composition. We used as a forward model (columns of the matrix  $A$  in eq. 1.30) uses DW-MRI signal arising from axons represented as parallel cylinders oriented in the same orientation of the streamline in the voxel and with fixed radii and fixed longitudinal diffusivity  $d_{\parallel}$ .

To account for different contributions arising from axons with distinct radii, we considered 12 columns for each streamline corresponding to 12 cylinders with radii equally-spaced diameters in the range  $1.5\mu\text{m}$  to  $7\mu\text{m}$ . Unlike in Assaf et al. (2008), no assumptions are made on the fiber composition to be estimated. To compute the columns related to the extra-axonal DW-MRI signal, we used as a forward model the signal arising from anisotropic tensors with the same longitudinal diffusivity but different perpendic-

ular diffusivities  $d_{\perp}$ . Finally, the cerebrospinal fluid is modeled as isotropic tensor with fixed diffusivity  $d_{iso}$ . The physical parameters were set as follows:  $d_{\parallel} = 1.7 \times 10^{-3} \text{ mm}^2 \text{ s}^{-1}$  [5, 370, 371],  $d_o = 3 \times 10^{-3} \text{ mm}^2 \text{ s}^{-1}$  [5, 206, 370, 371], and four values equally-spaced in the range  $0.5 \times 10^{-3} \text{ mm}^2 \text{ s}^{-1}$  to  $1.0 \times 10^{-3} \text{ mm}^2 \text{ s}^{-1}$  for  $d_{\perp}$ .

COMMIT estimates the volume-weighted axon diameter composition for each streamline. To facilitate visual inspection of the results, we associated an ADI [5] to each streamline and colored them accordingly. We recall the ADI is the mean of the axon diameter composition, as described in [5].

Differently, from the AMICO framework formulation [73], the estimation of the ADI is done excluding the smallest ( $1.5 \mu\text{m}$ ) and the biggest ( $7 \mu\text{m}$ ) cylinder compartments. This step was done for two reasons: i) the used DW-MRI acquisition was shown to be insensitive to diameters smaller than  $2 \mu\text{m}$  [249]. ii) We found that the smallest cylinder captures, only partially, the signal of axons from  $0 \mu\text{m}$  to  $1.5 \mu\text{m}$ , and the biggest cylinder captures the signal of axons above  $7 \mu\text{m}$ ; hence, those columns of the matrix  $A$  are indeterminate and cannot be included in the estimation. Simulations were performed to validate this conclusion, see the Simulation section.

The axon diameter composition can be defined for a given bundle (i.e., a group of streamlines coursing through a specific ROI). We calculated the overall axon diameter composition of a bundle by performing the weighted sum, column by column, of the axon diameter compositions of all streamlines of the bundle. Furthermore, in order to represent the axon diameter of a bundle with one value, we calculated the ADI of a bundle as the mean of the bundle axon diameter compositions.

### 5.2.2 Acquisition Protocol

The DW-MRI acquisition protocol used is the following: TE 80 ms, TR 3900 ms, matrix size  $110 \times 110$ , 2 mm isotropic resolution, gradient strengths  $G = 138 \text{ mT m}^{-1}$ ,  $276 \text{ mT m}^{-1}$ ,  $102 \text{ mT m}^{-1}$ ,  $203 \text{ mT m}^{-1}$ ,  $85 \text{ mT m}^{-1}$ ,  $169 \text{ mT m}^{-1}$ ,  $74 \text{ mT m}^{-1}$  and  $175 \text{ mT m}^{-1}$ ,  $\delta = 7 \text{ ms}$  and  $\Delta = 17.3 \text{ ms}$ , 17.3 ms, 30 ms, 30 ms, 42 ms, 42 ms, 55 ms and 55 ms. With the above parameters, a total of 360 DW-MRI images distributed over 8 shells and including 4 non-diffusion weighted images (b0) were acquired. An additional b0 image was acquired in reverse phase encoding to estimate the inhomogeneity field and induced eddy currents effect, which were used for the preprocessing steps for the in vivo data. We also acquired a 1 mm isotropic resolution T1-weighted anatomical image using a MPRAGE sequence: TE 2 ms, IT = 857 ms, TR=2300 ms, matrix size  $256 \times 256$ , flip angle  $9^\circ$ .

### 5.2.3 Numerical simulations: crossing configuration

A numerical simulation experiment was performed to generate a 45 deg crossing configuration between two bundles, from which, main directions were obtained at each voxel. The intra-

axonal and extra-axonal signals were generated separately and then merged to generate unique numerical phantom [290]. For each bundle, the DW-MRI intra-axonal signal and extra-axonal signal were simulated, using an in-house Monte Carlo Simulator [285], for a gamma distribution of parallel cylinder diameters with a mean diameter of  $2.70\mu m$  and  $4.00\mu m$ , with intra-axonal signal fractions of 0.3 and 0.4 and extra-axonal signal fraction of 0.7 and 0.6. Two additional extra-axonal signals were generated in the crossing area with a signal fraction of 0.21 and 0.09. All the signal were summed up to have a total signal fraction of 1 in each voxel, both in crossing and single population voxels. The diffusivity of the simulations were fixed to  $D = 1.7 \times 10^{-3} \text{ mm}^2 \text{ s}^{-1}$  [5, 370, 371], both for intra-axonal and extra-axonal signals.

The resulting dataset was corrupted with Rician noise using a SNR of 30 in the  $b = 0$  images. Furthermore, a Watson distributed dispersion with  $k = 16$  of was added to the resulting dataset [370, 371]. Tractography was then performed using a second-order integration over Fibre Orientation Distribution (iFOD2) algorithm [341], generating 10,000 streamlines, seeding from the white matter mask. Streamlines not ending at the bundle extremities were removed before processing with COMMIT.

### 5.2.4 Numerical simulations: resolution limit

A numerical phantom simulating the axon diameter distributions in the prefrontal and motor sectors of the CC derived from histology was used. These two sectors were chosen as they show significant differences in mean axon diameter, e.g., a representative of small and one example of large diameters. The purpose of this experiment was to test the feasibility of the newly proposed extension of the COMMIT framework to distinguish the bundle axon diameter composition and in an environment without MRI distortions. A second purpose of the simulation was to test the optimal range of diameter sensitivity. The intra-axonal signal of the two bundles was generated analytically to have two number weighted gamma distributions with means of  $1.18\mu m$  and  $1.59\mu m$  for the prefrontal and the motor bundles, respectively. The intra-axonal volume fraction used for both bundles was 0.7.

The number-weighted distributions are typically used in histological reports. However, MRI probes the volume of the structure, and thus provides estimates of the volume-weighted axon diameter [5]. The conversion from number weighted to the volume-weighted was performed, and the corresponding means were estimated to be  $1.94\mu m$  and  $3.32\mu m$ , respectively. The extra-cellular signal was computed with an in-house Monte Carlo diffusion simulator[285]: two different signals were generated, one for each bundle, with an extra-axonal volume fraction of 0.3 in each voxel. The signal was used then assemble to form two bundles with dimensions  $4 \times 4 \times 20$  voxels.

The data was simulated with 0.5 mm isotropic resolution, 360 DW-MRI images distributed on the same 8 shells and 4 b0 used to acquire in vivo data,  $\delta=7 \text{ ms}$ ,  $G= 138 \text{ mT m}^{-1}$ ,  $276 \text{ mT m}^{-1}$ ,  $102 \text{ mT m}^{-1}$ ,  $203 \text{ mT m}^{-1}$ ,  $85 \text{ mT m}^{-1}$ ,  $169 \text{ mT m}^{-1}$ ,  $74 \text{ mT m}^{-1}$  and  $175 \text{ mT m}^{-1}$ ,  $\Delta=17.3 \text{ ms}$ ,  $17.3 \text{ ms}$ ,  $30 \text{ ms}$ ,  $30 \text{ ms}$ ,  $42 \text{ ms}$ ,  $42 \text{ ms}$ ,  $55 \text{ ms}$  and  $55 \text{ ms}$ . Rician noise with SNR=30 was added

for the simulated data.

Figure 5.2, show that the extended COMMIT framework can distinguish the two distinct distributions of the prefrontal and the motor areas axons. Furthermore, analysis of the bundle ADI was done considering two different ranges: the full distribution (1.5  $\mu\text{m}$  to 7  $\mu\text{m}$ ) and removing the smallest and the biggest diameter (2  $\mu\text{m}$  to 6.5  $\mu\text{m}$ ), see Table 5.1. The comparison shows that considering the full distribution leads to an overestimation of the bundle's ADI is overestimated. However, when removing the contribution from diameters 1.5  $\mu\text{m}$  and 7  $\mu\text{m}$ , we recover the ground truth bundle ADI. These simulations show that those diameters are indeterminate and should not be included for the ADI estimation.

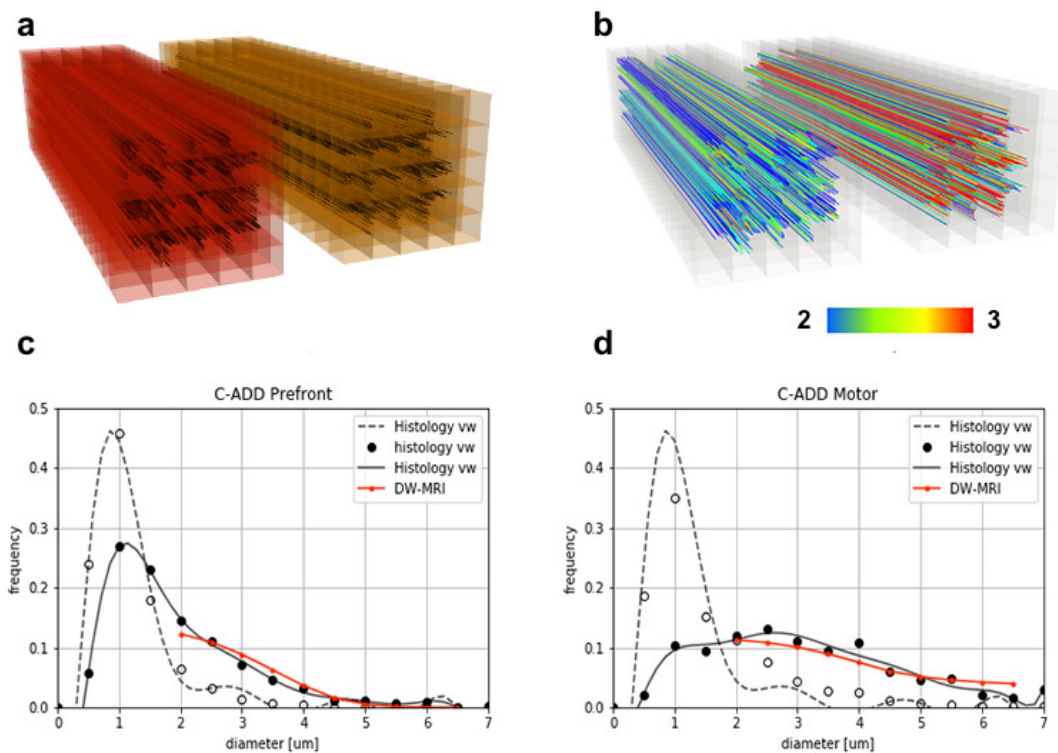


Figure 5.2 – Numerical simulations using histological prefrontal and parietal samples [55] were performed. (A) phantom shape and streamlines generated from: left) prefrontal area, right) motor area. (B) Estimation of axon diameter index (ADI) per streamline. Notice how prefrontal streamlines show a predominance of small diameter (blue) and motor area show predominance of large diameter (red). (C,D), show the axon diameter composition for prefrontal and motor areas. Different ranges were tested in order to find the DW-MRI sensitivity that is closest to the ground truth distributions, see Table 5.1.

### 5.2.5 Image processing

In vivo human data were acquired from 3 healthy volunteers on a Siemens Connectom 3T MRI system (Cardiff University Brain Research Centre, Cardiff, Wales). Each subject was imaged

## Chapter 5. Bundle-specific axon diameter mapping of cortical pathways

---

Table 5.1 – Empirical testing for the resolution limit on simulated data. Discarding the first and last bin yields DW-MRI estimates that match the histological ground truth. *Associated to Fig.5.2.*

mean diam [μm]	Hist nw	Hist vw	Hist vw	DW-MRI	Hist vw	DW-MRI
range	0-7	0-7	1.5-7	1.5-7	2-6.5	2-6.5
prefrontal	1.18	1.94	2.41	2.54	2.85	2.84
motor	1.59	3.32	3.42	3.65	3.52	3.52

five times over two weeks using the same MRI acquisition protocol described in section 5.2.2.

The anatomical T1-weighted image was registered to the average b0 image using FSL/FLIRT [172] using rigid-body registration. The white matter and gray matter masks were estimated using FSL/FAST [172]. The brain cortical parcellation was performed using FreeSurfer [79, 95].

The DW-MRI data were corrected for magnetic field inhomogeneities, eddy currents, and motion using the TOPUP and EDDY tools of FSL [172]. Subsequently, gradient non-linearity correction was performed [187]. The shell with diffusion time  $\Delta=17.3$  ms and  $G=276$  mT m<sup>-1</sup> was used to perform CSD [340]. Tractography was then performed using iFOD2 algorithm [341], generating 10,000,000 streamlines from the white matter mask. Streamlines not reaching the gray matter were removed. To reduce the computational burden of the COMMIT analysis, 300,000 streamlines were randomly selected for each DW-MRI dataset.

### 5.2.6 Analysis of specific neuronal connections

Our *in vivo* study is focused on two well-characterized axonal tracts: the CC and the PIC. The CC has been well studied in the past with different methodologies including DW-MRI [5, 25]. The PIC has been less studied with DW-MRI but is extremely important since it is traversed by cortico-descending axons involved in motor control, whose lesions lead to irreversible paralysis. Moreover, we concentrate the analysis on these two bundles since they are known to have a sufficiently large axons diameter to which we can be sensitive with DW-MRI.

To study the topology of bundles, the CC and the PIC were segmented and subdivided in, respectively, 11 and 6 equal sectors normalized for different individuals as described in section 5.2.6. The streamlines passing through ROIs corresponding to these sectors were selected, and we analyzed their projections to and from the cortex. These projections correspond to corticofugal and corticopetal (for the CC) connections since DW-MRI does not distinguish the direction of the connections.

Bundles of streamlines systematically organized from anterior to posterior connect the CC to similarly ordered slabs of cortex extending from the cingulate gyrus to the lateral sulcus, Figure 5.3. This has been shown by tracer injections in the CC of the cat [245], and is compatible with the ordering of CC connections already described with DW-MRI [152]. Also,

anteroposterior organized bundles of streamlines connect the sectors of PIC to anteroposterior cortical territories, compatible with the topology shown by tracer injections and DW-MRI in the monkey [237] and DW-MRI in humans [11].

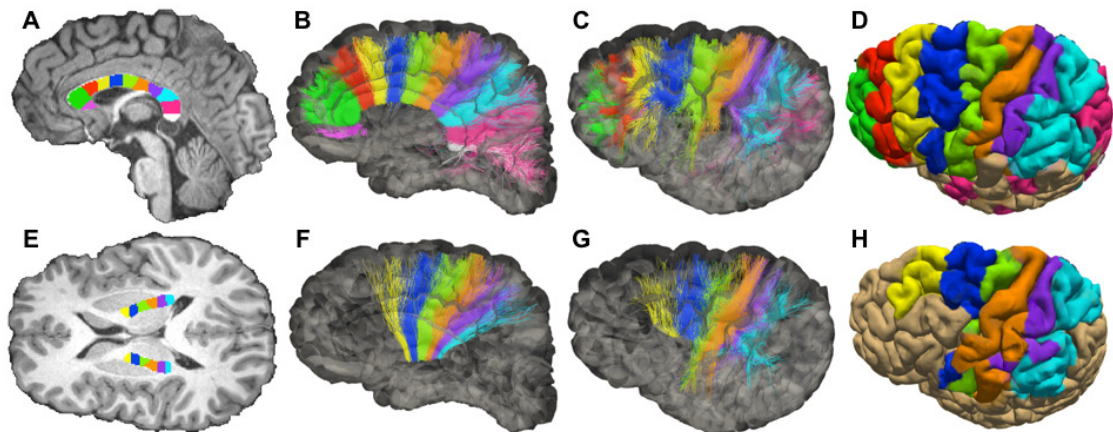


Figure 5.3 – Topology of fibers in the Corpus Callosum (CC) and posterior limb of the internal capsule (PIC), reconstructed with DW-MRI tractography. (A) Subdivision of the mid-sagittal section of the CC in 11 sectors (corresponding to ROIs). (B,C) Streamlines colored according to the corresponding ROIs (medial and lateral views of the hemisphere). (D) Projection of the streamlines into the pial surface. (E) Subdivision of PIC in 6 sectors (ROIs). (F,G) Streamlines colored according to the corresponding ROIs (medial and lateral view of the hemisphere). (H) Projection of the streamlines into the pial surface.

### 5.2.7 Histological preparation

One of the subjects already studied in Caminiti et al. (2009) was used: 489/07. The subject is a 60 year and 9-month female obtained from forensic medicine department in Frankfurt who died of a stabbing wound and whose post-mortem before fixation was 6 hours. Briefly, the brain was fixed by immersion in 4% (w/vol) paraformaldehyde, and a sagittal block containing the CC was removed, cryoprotected, cut frozen, and stained for myelin. The relevant ethical committee approved tissue sampling and procedures. The analysis was performed with Neurolucida 7 software (MBF Biosciences) and a digital camera-mounted Olympus BX51 microscope. The outline of the CC was drawn at low magnification and partitioned as in the DW-MRI work. In Caminiti et al. (2009), axon diameters were measured at 2,900 magnification 112  $\mu\text{m}$  to 600  $\mu\text{m}$  wide probes, traversing the CC from dorsal to ventral in the regions of maximal density of labeled axons. In the measurements, the transverse cut axonal profiles were approximated to circles whose size was incremented in steps of 0.09  $\mu\text{m}$ .

### 5.2.8 Histological analysis

We similarly performed new measurements of axonal profiles to test the stability of axonal assessments over several years and the biases potentially introduced by different sampling

## Chapter 5. Bundle-specific axon diameter mapping of cortical pathways

strategies. In the 6th sector of the CC, wherefrom projections course mainly to the precentral gyrus we compared the axon diameter distribution of 1403 axons measured in Caminiti et al. (2009) along a vertical dorso-ventral probe with a second sample of 451 axons in the middle of the sector 6 and with a third cohort of 1934 axons sampled systematically across the whole sector 6, see Figure 3 left. The 1st and the 3rd sample returned similar means ( $1.35\ \mu\text{m}$ ) and medians ( $1.06\ \mu\text{m}$  and  $1.1\ \mu\text{m}$  respectively). Values were not statistically different with t-test although they were different with Mann-Whitney U and Kolmogorov-Smirnov tests. The second sample (mean  $1.5\ \mu\text{m}$ , median  $1.25\ \mu\text{m}$ ) was significantly different from the others with all tests. Whether this difference is due to local inhomogeneities in the distribution of axon diameters or to other factors could not be determined. The frequency histogram of the three samples and the corresponding volume-weighted distribution are shown in Figure 5.4. The significance of the difference between samples is shown in Table 5.2.

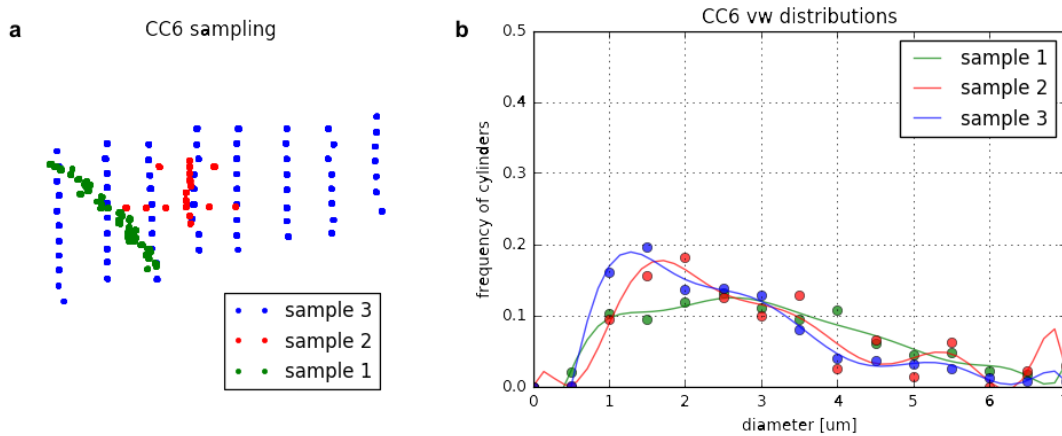


Figure 5.4 – Histological sampling CC sector 6. (A) Location of histological sampling in CC sector 6. (B) volume weighted distribution of the three samples. Sample 1 in Caminiti et al. (2009) has 1403 axons; sample 2, 451 axons and sample 3, 1934 axons. Significance of difference of samples are in Table 5.2.

Table 5.2 – Reproducibility histological sampling. Table associated to Fig. 5.4

p-value	T-test	Mann-Whitney U	Kolmogorov-Smirnov
S1 - S2	0.000256	2.532e-10	2.127e-33
S1 - S3	0.832280	1.161e-16	9.919e-53
S2 - S3	4.575e-07	2.593e-10	7.001e-07

## 5.3 Results and Discussion

### 5.3.1 *In-silico* analysis

The bundle-specific COMMIT framework and the voxel-wise ActiveAx [5] method were firstly tested on the numerical phantom described in Section 5.2.3. The qualitative and quantitative results are reported in Figure 5.5 and Table 5.3. For the voxel-wise estimation, the ADI for each



voxel was estimated with the ActiveAx method described in [5]. For the COMMIT framework, the two bundles were reconstructed using tractography, and two scalar maps were generated, projecting the weighted signal fraction ADI estimated for each streamline onto the voxel-based space. Various studies ([16, 369]) have already shown that the ActiveAx method [5] encounter difficulties in solving the crossing problem. However, it has been widely used in single populations voxels. Hence, the reason to include in the analysis also single populations voxels.

As expected, results show that the ActiveAx method report diameter overestimation and significant-high standard deviation in all the phantoms configuration. The best performance in our simplistic phantom is obtained for the case of no dispersion, single population and diagonal bundle at 4  $\mu\text{m}$  of ground truth in diameter. In this specific case, good results are also reported for the smaller bundle, which we observe an overestimation of 0.5  $\mu\text{m}$ . We highlight that the standard deviation reported is in the range 3  $\mu\text{m}$  to 4  $\mu\text{m}$  in all the cases.

Contrary to the voxel-wise method, COMMIT can solve the crossing problem and estimate diameter indexes closer to the ground truth values. More precisely, in the case of no dispersion, the bundle corresponding to the smaller diameter is overestimated by 0.2  $\mu\text{m}$  while the largest diameter is underestimated by 0.5  $\mu\text{m}$ .

Interestingly, in the case of dispersion, the estimation with COMMIT performs better achieving the ground truth in the bundle with the lower mean diameter and underestimating by 0.5  $\mu\text{m}$  in the bundle with the bigger mean diameter. Furthermore, the standard deviation reported is from three to four times smaller compared to the voxel-wise method.

In these numerical experiments, we proved the benefit of using COMMIT to estimate ADI.

		Axon diameter index [ $\mu\text{m}$ ]	
		no dispersion	dispersion
ActiveAx	bundle straight	4.16 +/- 3.00	5.57 +/- 1.60
	bundle straight (no crossing)	3.16 +/- 3.27	5.31 +/- 1.81
	bundle diagonal	4.40 +/- 3.91	5.59 +/- 4.07
	bundle diagonal (no crossing)	3.95 +/- 4.30	5.45 +/- 4.57
COMMIT	bundle straight	2.92 +/- 0.90	2.66 +/- 1.00
	bundle diagonal	3.54 +/- 1.39	3.67 +/- 1.87

Table 5.3 – Axon diameter estimation: voxel-wise ActiveAx original implementation and bundle-specific COMMIT.

### 5.3.2 Bundles composition

The fiber composition of the CC obtained with our novel technique was compared with postmortem measurements of a human brain. Between 451 and 1934 axons stained for myelin were measured in CC sectors crossed by axons connecting the prefrontal, motor, parietal and visual cortices. Most measurements were from a previous study [55], but one of the sectors was

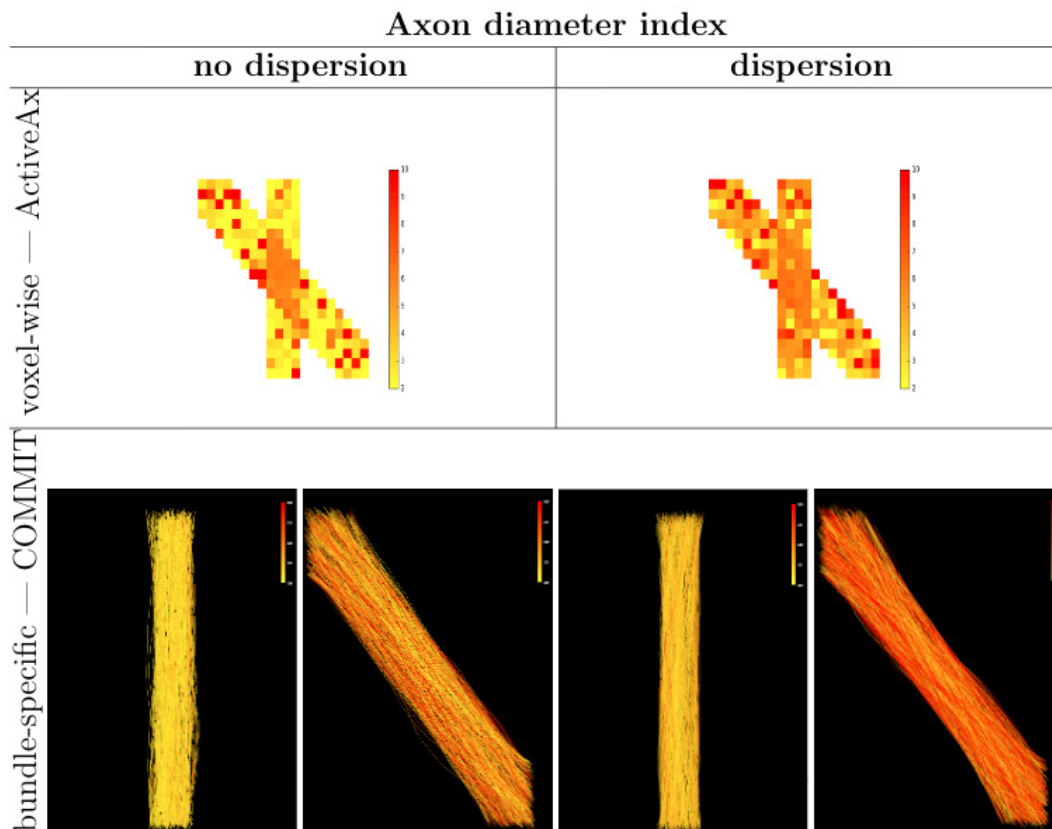


Figure 5.5 – Axon diameter estimation: voxel-wise ActiveAx original implementation and bundle-specific COMMIT. SNR=30, dispersion  $k=16$ .

measured again to evaluate the impact of histological sampling. From the histological data, we estimated the histogram of diameters in each sector. However, since DW-MRI estimates the signal fractions that are related to the volume occupied by axons of different diameter, not their number, the data was converted to volume-weighted distributions, to allow comparison with the DW-MRI estimates. Figure 5.6 shows that fiber composition estimated with DW-MRI closely corresponds to the histological estimates within the DW-MRI range of sensitivity.

In the absence of human data, the *in vivo* estimates of the PIC were compared with measurements of axons stained for myelin in the monkey PIC [163]. In both bundles we studied, the highest axon diameters recovered by COMMIT were found in sectors of PIC traversed by axons connecting the motor cortex (BA 4) while thinner axons were connected to other areas. In order to facilitate visual inspection of the results, the streamlines passing through each CC sectors were colored according to the corresponding ADI [5], which is a weighted average of the different contributions estimated for each streamline, and their endpoints were projected on the cortical surface, see Figure 5.7.

This visualization reveals that streamlines with thicker axons connect the CC to the pre-

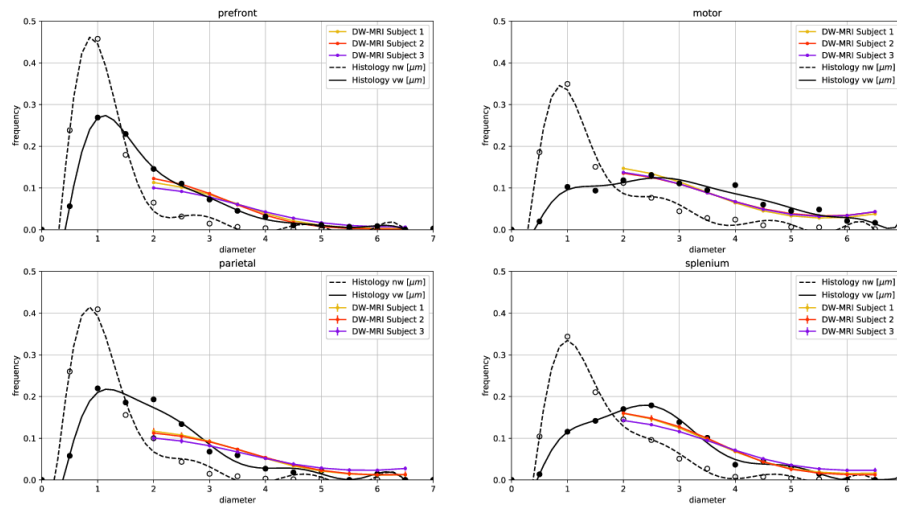


Figure 5.6 – Comparison of the fiber composition estimated with DW-MRI and histology in 4 CC sectors. The black curves represent axon diameter distributions (normalized to 1) of myelinated axons estimated with histology (dashed=number weighted, nw; continuous=volume weighted, vw). The three colored curves represent the axon diameter composition of bundles of streamlines passing through the respective CC sectors, scaled according to histology in the range 2  $\mu\text{m}$  to 6.5  $\mu\text{m}$ .

central gyrus, corresponding to the primary motor cortex (M1; Brodmann area BA 4), the more lateral part of premotor cortex (BA 6), and to the postcentral gyrus (BA 3,1,2) corresponding to the primary somatosensory cortex (S1). Streamlines with progressively thinner axons terminate in the medial premotor cortex (BA 6) and the parietal cortex (BA 5,7 and 40) and still thinner axons in the rostral prefrontal cortex (BA 8 and 9) and BA 44 and 45.

Our method provides an *in vivo* estimate of the distribution of axon diameters along a fiber tract (the CC); previous measurements were only possible *ex vivo*, with histological tracers in the monkey [55, 336]. In both species, a hierarchy of axon diameters exists with thicker and faster-conducting axons connecting the motor and somatosensory cortices, thinner and slower axons elsewhere. The streamlines coursing in the PIC were color-coded as above according to their estimated ADI. Those consisting of the thickest axons are mapped onto the dorsal part of the precentral BA 4 (M1) and postcentral (BA 3,1,2; S1) gyrus. Progressively thinner axons mapped onto the parietal cortex (BA 5 and 7) and the premotor cortex (BA 6) and still thinner axons onto the rostral prefrontal cortex (BA 8 and 9).

This arrangement is similar to that demonstrated with injections of anterogradely transported tracers in corresponding areas of the monkey, although in the monkey the diameter of axons originating in the precentral gyrus exceeds that of axons originating in the postcentral gyrus [163]. Identical findings were reproduced for different sectors of the CC and PIC in three

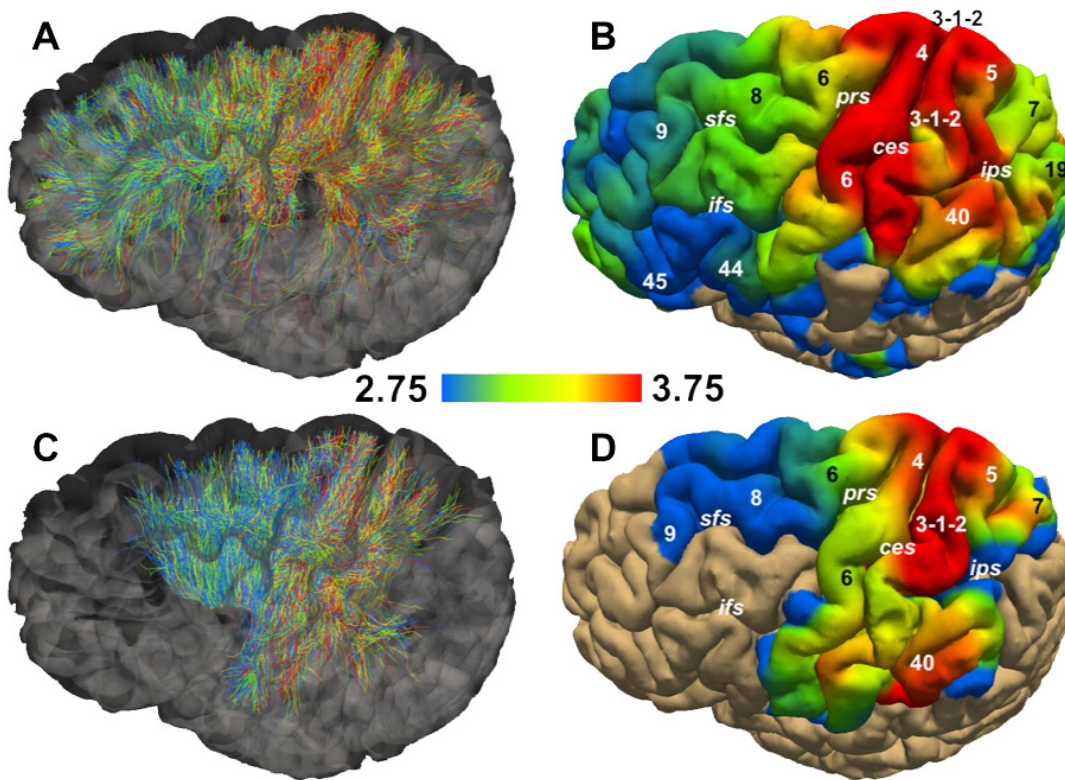


Figure 5.7 – Fiber composition of the streamlines passing through the CC and PIC. (A,C) show streamlines colored according to their Axon Diameter Index (ADI). (B,D) show the projection of streamlines onto the pial surface; colors correspond to the ADI averaged across streamlines. Abbreviations: ces, central sulcus; ifs, inferior frontal sulcus; ips, interparietal sulcus; prs, precentral sulcus; sfs, superior frontal sulcus. Numbers correspond to Brodmann areas.

subjects and five times for each subject, Figure 5.8 and Figure 5.9.

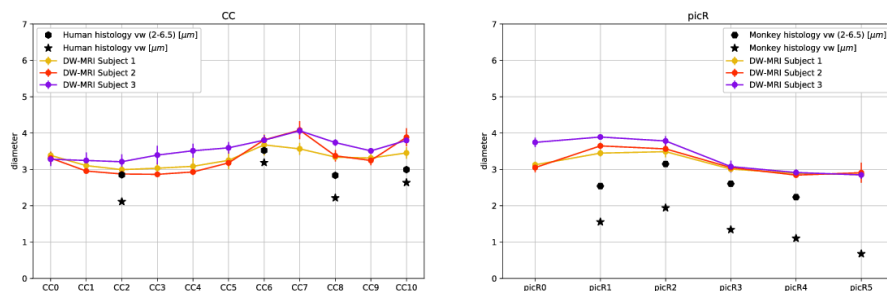


Figure 5.8 – DW-MRI axon diameter composition within CC and PIC sectors compared to histological mean volume-weighted axon diameter from human (CC) and monkey (PIC) histology. Stars represent means of the volume-weighted histological distributions; hexagons represent the means of volume-weighted distributions in the range 2 μm to 6.5 μm.

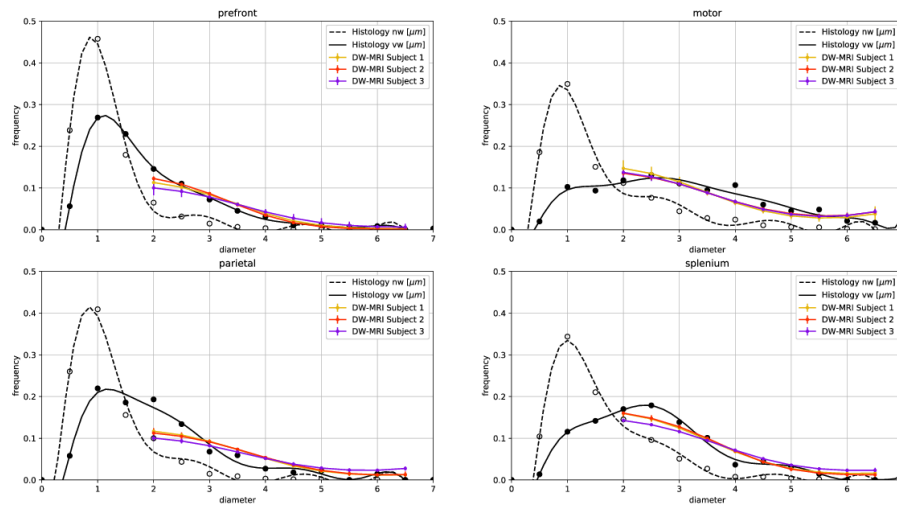


Figure 5.9 – Reproducibility study on the comparison of axon diameters estimates with DW-MRI and histology in 4 CC sectors. The black curves represent axon diameter distributions (normalized to 1) of myelinated axons estimated with histology (dashed=number weighted, nw; continuous=volume weighted, vw). The three colored curves represent the axon diameter composition over streamlines passing through the respective CC sectors, scaled according to histology in the range 2  $\mu\text{m}$  to 6.5  $\mu\text{m}$ . For each diameter, the means and standard deviations over five acquisitions are shown. Reliable estimates of axon diameters could be obtained only between 2  $\mu\text{m}$  to 6.5  $\mu\text{m}$ .

The crucial importance of long connections in brain function is well established among others by split-brain studies [326], and so is the importance of different axon diameters in the peripheral nervous system [136]. The existence of brain pathways consisting of axons of different diameters has been guessed in humans based on brain slices, sometimes processed for electron microscopy, and invariably weakened by poor tissue preservation. The histological material used here was no exception to this drawback, Figure 5.10. The previous DW-MRI methods modeled axons at selected locations within a tract assuming their linear trajectory. This assumption caused gross overestimation of axon diameters [5]. In this study, tracking cortical pathways in vivo from DW-MRI acquisitions using a cutting-edge scanner and evaluating their composition using a novel technique overcame these limitations. Moreover, it provided estimates of axon diameter composition closer to histology findings. Current technologies restrict the resolution of axon diameters to about 2  $\mu\text{m}$  [249].

## 5.4 Conclusion

Since thick axons are found preferentially in specific pathways, their absence in the expected pathways, or abnormal presence in unexpected pathways can disclose the neural basis of

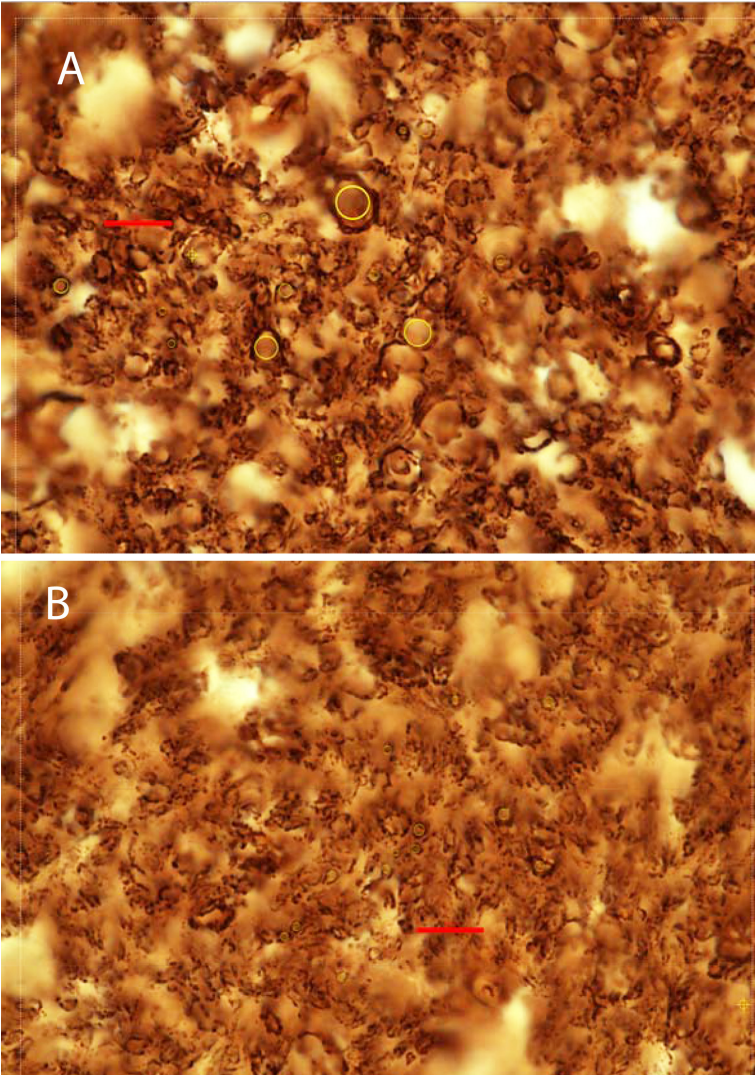


Figure 5.10 – Myelin-stained transversally-cut axons in sectors 6 (A) and 8 (B) of the Corpus Callosum (CC) of a human case. Scale bar is 10  $\mu$ m. Some of the axons are surrounded by a measuring circle. Notice the mediocre preservation of the tissue, unavoidable with human material.

specific neurological or psychiatric pathologies [90, 157, 374] and, possibly, of individual skills [83]. An additional advantage of our approach is that the axon diameter composition of a tract could be mapped onto the cortex where it originates (and/or terminates in the case of CC), eliminating the ambiguities of tracking axon diameters at selected locations along the white matter pathways [5, 14, 25]. Our findings stress the similarities between humans and monkey in the axonal composition of callosal and corticospinal projections. The existence of corticospinal projections with different axon diameters and hence conduction velocities from different cortical areas, in both species, raises the question of how the motor command is integrated at the spinal cord level [163] a crucial question for strategies attempting to restore corticospinal control after lesions. On the other hand, the size and speed advantage of motor and sensory axons in corticocortical connections raises in humans, more appropriately than in monkey, the question of their role in the generation of the sense of body ownership [336]. Further studies could extend the presented approach to other CNS pathways significantly amplifying the human “connectome” enterprise [70, 140, 169].





# 6 Conclusion

## 6.1 Summary of the contributions

The ultimate goal of the neuroscience research is to study the human brain, understand the underlying biological mechanisms, reconstruct the complex network of neurons, i.e., connectomics, diagnostic pathological conditions and ultimately give insights of how to cure these conditions. All of these aspects are essential and related to each other. For what concerns this thesis, we focused on the non-invasive imaging of the brain structure. From the several techniques available to image the brain, we focused on MRI and more specifically on DW-MRI.

We used DW-MRI, and not conventional MRI contrasts because our goal is to reconstruct the brain network, which is mainly composed of axons and cell bodies of neurons. These last structures are on the size of micrometers; however, with clinical MRI the resolution is in the order of millimeters. DW-MRI comes as a tool of choice to infer micrometer structures using the natural diffusion of water measured in multiple directions at a millimeter resolution. More specifically, thanks to inverse problem techniques, it is possible to use the measures acquired with DW-MRI and reconstruct tissue properties, e.g., fiber orientation, axonal density, axon diameter. Furthermore, it is possible to connect the different WM voxels in the brain and performed the so-called tractography. Both problems have high complexity, and over the last years, the community has split the two field and focused either on tractography or microstructure. Few attempts have been made to merge the two fields using non-convex formulations. However, at the cost of a computational burden of several weeks. In 2015, the COMMIT framework was proposed to linearize the problem and showed advantages in the combination of minimal microstructure modeling, e.g., the use of Stick for intra-axonal compartments and Zeppelin for the extra-axonal compartment. In this thesis, we show the advantages of combining microstructural imaging and tractography in a unique formulation using advanced modeling, e.g., axon diameter mapping and  $T_2$  estimation.

In Chapter 2, we report the advancement of tractography, focusing on the benefits and main limitations learned through international challenges competitions proposed in the

## Chapter 6. Conclusion

---

period of 2015 and 2018. This first analysis of state of the art study in tractography was necessary for two main reasons: 1) to understand what is the best tractography algorithm available, which potentially can be used in our formulation; and 2) to understand what if exist WM bundles where DW-MRI tractography recovers with high precision and which are more harder to reconstruct.

Another important limitation, which we discussed in Chapter 2, is the challenge in tractography validation. In the field, three main validation methods have been proposed: using simulated data with know ground truth, using physical phantoms with know ground truth, and using histological analysis from ex vivo data. The first two techniques suffer from oversimplistic geometry, while the ex vivo analysis is often achieved with 2D slicing. In Chapter 3 we investigate the potential of using a novel 3D histological technique to validate fiber orientation and tractography, named CLARITY. CLARITY has been proposed two years ago as a validation technique for DW-MRI in small cuboid in the order of less than 1 mm and only in GM. In this chapter, we propose the first study that uses CLARITY in large slabs of monkey brain, in the order of 1.5 cm. The sample covers GM and WM. We find that CLARITY is a potential complementary tool to extract information on fiber orientation. Furthermore, a second contribution of the study is in the development of a FOD estimation algorithm for 3D ex vivo histology.

In the latest years, one of the main topics that got interested in the Diffusion MRI community is the capability of disentangling intra-axonal  $T_2$  of different bundles in the brain. The state of art methods is limited to a single bundle population. In Chapter 4, we implemented an extension of COMMIT modeling the intra-axonal  $T_2$  even in presence of multiple population within a voxel. We showed that this new framework has advantages in disentangling intra-axonal  $T_2$ . The analysis was performed in numerical simulations and on real data.

From a biological perspective, the major proposal in this thesis is in the estimation of axon diameter features regularized by streamlines tractography. In Chapter 5, we extended the COMMIT framework allowing streamlines to have cylinder model of different sizes. We proposed two simulation studies, one selecting the optimal dictionary for the resolution limit of the protocol used, and the second showing that our formulation have major advantages in crossing bundles and in presence of axonal dispersion. Furthermore, we compared the DW-MRI estimates with histological material, finding good agreement on the fiber composition.

The approach used in the previous two chapters, to extend the original COMMIT dictionary, led to an increase of the computational burden. For example, in the case of the axon diameter estimation, the computation time can reach up to 24 hours. In the appendix A, we propose a neural network to recover scalar maps extracted from the global features estimated by COMMIT, e.g., axon diameter map. This novel approach brings down the COMMIT fitting time from several hours to few second, maintaining similar results compared to the original formulation, and allowing fast computation and in the future potential clinical application usage.

## 6.2 Perspectives

Following the order of the chapters proposed in this section, we want to highlight the future works and perspectives that emerged from the work proposed in the thesis.

**Tractography.** Tractography, as a tool, has been the *leitmotif* of this thesis. We have showed the advantages and limitations, and we showed the potential benefits of combining the technique with microstructure modeling using convex optimization. However, not all the work is done. What can we do next and what is the future of tractography?

We need to start from the basics. A streamline is not an axon, it is not a bundle and is not a biological representation of the underlying structure. It is a potential representation of the underlying structure. The reason is that we have a limited understanding of the physical and biological properties and the technology which tractography is based on.

In the following list, I report my view on what the *ultimate* tractography algorithm should be able to do:

- *Tractography needs to learn from mistakes.* Since the complexity of the problem is high, most researchers implement tractography algorithms to solve one specific problem, e.g., solving a bias or following biophysical parameters. The researcher injects the prior, spend several months for the implementation, and finally, the tractography algorithm is used for a specific application. However, often, development stops, and it is difficult to integrate this new knowledge in a unique formulation from another researcher which may be working on a different aspect.
- *Tractography needs quality feedback when tracking.* This statement is related to the previous one. Often tractography algorithms do not have a way to show the potential error made during tracking; this aspect brings difficulty in the interpretation of the results. An algorithm that shows during tracking the percentage of how good is the tracking according to predefined rules, and perhaps, showing critical section where estimation start to be less confident, can be useful to understand better the where the bundle brake down or could have generated a potential error.
- *What are the alternatives of DW-MRI tractography?* Very little time is spent thinking if we have alternatives to DW-MRI to perform tractography for reconstructing the brain connections since up to date very few alternative exist in vivo in human.
- *Include complementary information.* As several works are proposing in the last years [139, 302], we may start to think to add more and more anatomical priors derived from literature or complementary information derived from physiology to achieve better algorithm reconstructions.
- *Reproducibility.* To have tractography in the routine of clinical applications, the reproducibility of results will need to be achieved.

## Chapter 6. Conclusion

---

**Validation with 3D histology.** To validate tractography and microstructure imaging, comparison with histology is necessary. More specifically, 3D histology technique should be refined and developed to overcome classical 2D histological techniques.

Another essential factor to consider is the costs of performing protocols and acquisition of histological data. Ideally, the post mortem imaging techniques must be accessible and easy to use to a broad community to researchers. However, often, this is not the case.

Despite the importance of having better protocols for the histological pipelines, one of the main limitations is the imaging. Only few microscope are able to image a large portion of tissue, e.g., few cm, at the level of  $\mu\text{m}$ , especially in a reasonable amount of time, e.g., less than one day, and without artifacts.

In Chapter 3, we proposed the first study of using CLARITY in a large portion of tissue, and we proposed a potential validation study. However, our study could be improved in several aspects:

- the CLARITY data were acquired on a different monkey, in future, we would like to have the analysis performed on the same sample.
- different variation of the CLARITY protocols were proposed; however, the one that showed best results is the variation that uses passive clearing, hence, without electrophoresis and with no acceleration the clearing process. The passive clearing for large samples can take up to several months. It will be desirable to accelerate the procedure.
- in the study that we proposed, six slabs of monkey tissue were cleared with CLARITY; however, only two of them showed contrast after the imaging in the microscope. The reason why the process did not work is not known, and it will be desirable to explore more this aspect.
- from the DW-MRI perspective it will be useful to acquire the same sample with several protocols with different resolution and study the agreement with histological validations.

The ultimate goal that will help to understand the structural brain will be to have in vivo, ex vivo and 3D histology of the same sample.

**$T_2$  mapping.** Generally, in the research topic of  $T_2$  estimation, researchers tend to find tools to disentangle myelin water, intra-axonal water, and extra-axonal water fractions. However, it is plausible to assume that within the different tissue compartments exist a variation. We tried to propose methods able to disentangle the difference of the intra-axonal  $T_2$ .

One fundamental work to be done will be the development of a  $T_2$  simulator for different tissue geometries and properties. Furthermore, the framework should be tested under a

possible assumption of  $T_2$  orientation dependence of bundles. Ultimately, we would like to extend the approach proposed, including also an extra-axonal signal.

**Axon diameter mapping.** Similarly to work presented in Chapter 3, also here the comparison of the axon diameter estimation done with DW-MRI and histology was performed in different brains. It will be desirable to perform the analysis on the same tissue sample.

It is essential to mention the limitations of histological material. Especially in human samples, but also in monkey samples, the preservation tissue is challenging due to deformation artifacts. Furthermore, the histological sampling of axon diameter is often performed manually by humans, mainly because of the difficulties in automatic segmentation; hence, it is limited to a few locations. Novel techniques are emerging to automatize the reconstruction, but often they do well in reconstructing the inner-diameter while myelin, extra-axonal space is more challenging to be segmented. Usually, because of the above mentioned reason that the human material is difficult to be preserved.

It is crucial to have a measurement of axon diameter for several reasons. Since it is strictly related to conduction delay, we would like to reconstruct fast conducting and slow conducting impulses. This will allow us to understand better neural communication and brain behaviour. Furthermore, axon diameter could help to understand the relation between structure and function, development, and give more insights about plasticity.

More precisely, in the approach proposed in Chapter 5, we assume invariance along a streamline. This constraint approach showed good results in several applications. This could be further extended to allow variance along the streamlines.

It is essential to highlight that axon diameter estimation is a highly degenerate problem, which is mainly dependent on the gradient strength and the SNR achievable. Different protocols have been proposed, e.g., oscillating gradients, diffusion spectroscopy. A possible future work could extend the COMMIT framework to take into account the advantages of these different protocols.

Similarly to work done in Chapter 4, an important aspect will be to use protocols with high b-value that suppress the extra-axonal signal.

In terms of modeling, we could use more complex atoms for the extra-axonal signal, i.e., derived from Monte Carlo simulations.

As the last step, we should investigate the relations between the similar trends found in the different bundles analyzed in the axon diameter estimates, in chapter 5, and  $T_2$  estimates, in chapter 4.

## Chapter 6. Conclusion

---

**Philosophical conclusion.** *Tractography will improve with new knowledge and technology.* Tractography will only benefit from new technologies and a new understanding of the physical mechanisms underlying the brain structure. At a certain point in time, we will have a non-invasive tool that accurately represents the underlying tissue; it can be a key factor necessary for the human species. However, to achieve such a goal, we do need more iterations and more research in the field from different perspectives.

# **A Appendix: Learning global brain axon diameter index maps using trainable sparse encoders**

Currently, one of the promising methods for microstructure imaging in DW-MRI is signal modeling using convex formulation, e.g., using the COMMIT framework. Recently, COMMIT has been extended to estimate axon diameters, see previous chapter. Despite the benefits introduced with the axon diameter formulation, a significant limitation is the long convergence time that can reach more than 24 hours for computation, making the method unappealing for large subject studies. In order to address this limitation, we propose to use a neural network to learn the sparse representation of the data and implement an end-to-end reconstruction of the microstructure estimates directly from the DW-MRI data. The results show that the neural network can accurately estimate the microstructure scalar maps, four orders of magnitude faster than the convex formulation.

## **A.1 Introduction**

DW-MRI has become the method of choice to probe the human brain's white matter in vivo [183]. DW-MRI has been used for the reconstruction of the WM pathways of the brain using tractography algorithms[177]. However, tractography has been shown to be not a truly quantitative method [165, 168, 221, 307]. To overcome such limitation, the COMMIT [76, 77] framework was introduced.

In previous studies, this framework was successfully used to recover ADI [5], see chapter 5, from whole-brain tractography on ex vivo monkey data[23] and on in vivo human data[24]. However, even if the convex optimization formulation brings fast estimations for simple biophysical forward models, with the increase in complexity of the forward models, the optimization procedure can reach several hours/days of computation time. For example, for 300K streamlines, 12 values of diameter for streamlines, 360 diffusion directions . In the following sections, we propose the use of a deep neural network to learn the sparse representation of the data and perform an end-to-end reconstruction of the axon diameter estimates directly from the DW-MRI data.

## Appendix A. Appendix: Learning global brain axon diameter index maps using trainable sparse encoders

---

Inspired by Ye et al. (2017) [366], we propose to learn the sparse representation of the voxel-wise mean ADI (mADI) computed with the aforementioned COMMIT framework.

### A.2 Methods

The COMMIT framework associates whole-brain tractography streamlines and microstructure imaging in a joint formulation. Briefly, COMMIT associate to each streamlines a coefficient depending on the microstructural model used. The estimated coefficients of  $x$  for each streamline can be then projected back to the voxel space. This procedure generates biophysical scalar maps allowing comparison to state-of-art voxel-based methods [5, 73].

#### A.2.1 Learned Sparse Encoding

The goal of sparse encoding is to reconstruct an input signal using a linear combination of basis functions with a sparse set of coefficients. In the work of Gregor and LeCun (2010) [145], a learned method that computes approximations of optimal sparse codes in a fixed amount of times was proposed. The method uses a time-unfolded neural network architecture where back-propagation through time can be applied. This method was coined Learned Iterative Shrinkage/Thresholding Algorithm ISTA (LISTA) since it unfolds the popular ISTA algorithm [81], which solves the most common form of sparse encoding. This is summarized in equation A.1,

$$E_{W_e}(X, Y) = \frac{1}{2} \|X - W_e Y\|_2^2 + \alpha \|Y\|_1, \quad (\text{A.1})$$

where  $W_e$  is a  $N_{signals} \times N_{atoms}$  dictionary matrix of which the columns are the basis vectors,  $\alpha$  is a coefficient controlling the sparsity penalty, and the vector  $Y$  is the signal data. ISTA finds the sparse coefficients  $X$  by iterating until convergence the following equation:

$$Y_{k+1} = h_\theta(W_e X + S Y_k), Y(0) = 0, \quad (\text{A.2})$$

where  $W_e = \theta W_d^T$  is the filter matrix,  $S = (I - \theta W_d^T W_d)$  is the mutual inhibition matrix  $\theta$ -weighted, and  $h_\theta(\cdot)$  is the shrinkage function [145]. The idea of LISTA is to unfold the iterative process in Equation A.2 and map it into a sequential neural network.

**Sparse Encoding for Microstructure Estimation.** In a previously proposed framework, Daducci et al. used sparse encoding to infer microstructure information using dictionaries of microstructure compartmentalized signals, coined as AMICO [73]. More recently, [366] used the LISTA architecture to learn microstructure properties by mimicking the computation of the NODDI estimates as proposed in AMICO.

Differently, from local microstructure frameworks like AMICO where the estimations are



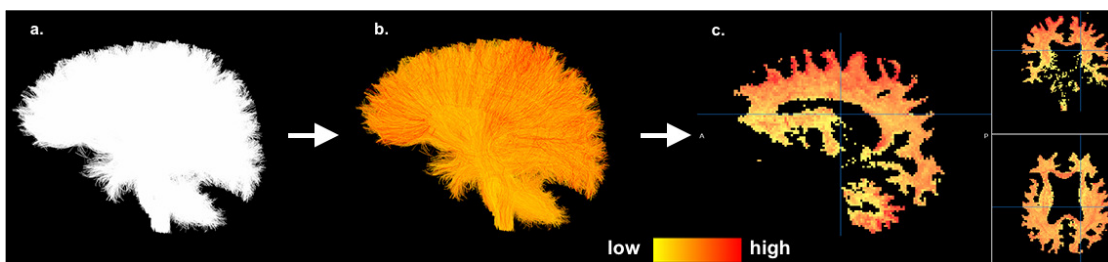


Figure A.1 – a) Whole-brain tractography of one of the subjects of the HCP dataset; the white colour of the streamlines means that no quantitative information is associated to the tractography; b) Whole-brain tractography with streamlines colored according to the Axon Diameter Index (ADI) estimated using the COMMIT framework; c) Voxel-wise map of the mean Axon Diameter Index (mADI); left: sagittal view, top right: coronal view; bottom right: axial view.

computed voxel-by-voxel independently, COMMIT computes the microstructure properties jointly for the whole-brain, using the geometry of the streamlines to create voxel connections. We use the LISTA Network architecture to map the voxel-wise DW-MRI signal to the estimated mADI by adding a fully connected layer that maps directly into the learned coefficients.

### A.2.2 Dataset

We used 34 subjects of the MGH-USC HCP Adult Diffusion Dataset [114, 314]. The DW-MRI acquisition scheme consists of 552 q-space samples over 4 shells with b-value =  $1000 \text{ s mm}^{-2}$ ,  $3000 \text{ s mm}^{-2}$ ,  $5000 \text{ s mm}^{-2}$  and  $10000 \text{ s mm}^{-2}$  and 40 b-value =  $0 \text{ s mm}^{-2}$  images. The DW-MRI images were acquired at 1.5 mm isotropic voxel size (Spin-echo EPI sequence, TR = 8800 ms, TE 57 ms  $\delta=12.9 \text{ ms}$ ,  $\Delta=21.8 \text{ ms}$ ).

DW-MRI images were corrected for motion and EDDY currents [114]. The FOD were computed using a single averaged fibre response (white matter voxels with fractional anisotropy above 0.7) as input for the CSD [57, 340] on single-shell DW-MRI images ( $3000 \text{ s mm}^{-2}$  and a maximum spherical harmonic order 8). Partial Volume Estimates (PVEs) for the white matter, gray matter, and cerebrospinal fluid were obtained from the provided T1-weighted using FSL/FAST [373]. We used the PVEs as input for the probabilistic Particle Filtering Tractography (PFT) algorithm [135, 139], with a total of 80K streamlines generated from seeds in the white matter volume, the resulting streamlines are shown in Figure A.1a.

We used the COMMIT framework to estimate the ADI coefficients [5] for each streamline, Figure A.1b, and the Extra Axonal Signal Fraction (EASF) for each voxel, as previously done in [23, 24]. We used the *Cylinder-Zeppelin-Ball* multi-compartment model [5, 268] with extra-axonal perpendicular diffusivity  $d_{\perp} = 0.51 \times 10^{-3} \text{ mm}^2 \text{ s}^{-1}$ ,  $0.68 \times 10^{-3} \text{ mm}^2 \text{ s}^{-1}$ ,  $0.85 \times 10^{-3} \text{ mm}^2 \text{ s}^{-1}$  and  $1.02 \times 10^{-3} \text{ mm}^2 \text{ s}^{-1}$ , isotropic diffusivity  $d_o = 3 \times 10^{-3} \text{ mm}^2 \text{ s}^{-1}$ , and intra-axonal longitudinal diffusivity  $d_{\parallel} = 1.7 \times 10^{-3} \text{ mm}^2 \text{ s}^{-1}$  with 9 cylinders with diameters

## Appendix A. Appendix: Learning global brain axon diameter index maps using trainable sparse encoders

---

ranging from  $2\ \mu\text{m}$  to  $10\ \mu\text{m}$  [23, 24]. The mADI, Figure A.1c, is reported voxel-wise as:

$$mADI = \frac{\sum_s^S w_s \cdot l_s \cdot ADI_s}{\sum_s^S w_s \cdot l_s}, \quad (\text{A.3})$$

where  $S$  is the set of all streamlines crossing the voxel,  $ADI_s$  is the ADI of the streamline  $s$ ,  $l_s$  is the length of the segment intersecting the voxel, and  $w_s$  is the intra-axonal contribution of the streamlines.

### A.2.3 Neural Network Parameters

**Training data.** We used a total of 20 subjects for training and 14 for testing. The input data consisted of all 552 q-space samples over the four shells for all the DW-MRI voxels inside a predefined white matter mask. The total number of input voxels counted in all training subjects was 3066226 voxels, and 2178620 voxels for the testing set.

**Network Hyperparameter Tuning.** We performed a selective tuning of the network parameters by discretely varying the following parameters and re-training the network: a) the number of hidden layers from 5 to 10 layers, which relates to the number of ISTA iterations to achieve convergence, b) The number of epochs from 200 to 500 epochs, c) The column-dimensionality of the matrix  $W_e$  from 200 to 500, which is related to the number of dictionary atoms to learn in the encoder, and the dimension of the last layer for microstructure estimation denoted as  $D$ . Each network was generated by varying one parameter at the time and fixing all others to the median value in the compared range. In the following results, we used the set of parameters which resulted in the lowest mean squared error over the training set, 8 layers, 300 columns, and 200 epochs.

## A.3 Results

Figure A.2 shows the mADI and the EASF maps obtained for a single volume in the test dataset from both the Neural Network (NN) and COMMIT. The bottom row shows the difference map between both estimations. The overall mean ( $\mu$ ) and standard deviation ( $\sigma$ ) of the mADI and EASF error, calculated as the difference between the estimations of COMMIT and the NN over 14 training subjects, were  $\mu = 0.627$  and  $\sigma = 0.083$ , and  $\mu = 0.028$  and  $\sigma = 0.003$ , respectively. In addition, a regular trend of high mADI estimations near the CC can be observed in both COMMIT and NN methods, as well as a decrease of the EASF in both maps in the same CC regions. The average computation time for COMMIT was approximately 15 hours per subject on a machine with 12 cores, while with NN, the computation time went down to a few seconds per subject using a NVIDIA Titan Xp GPU.

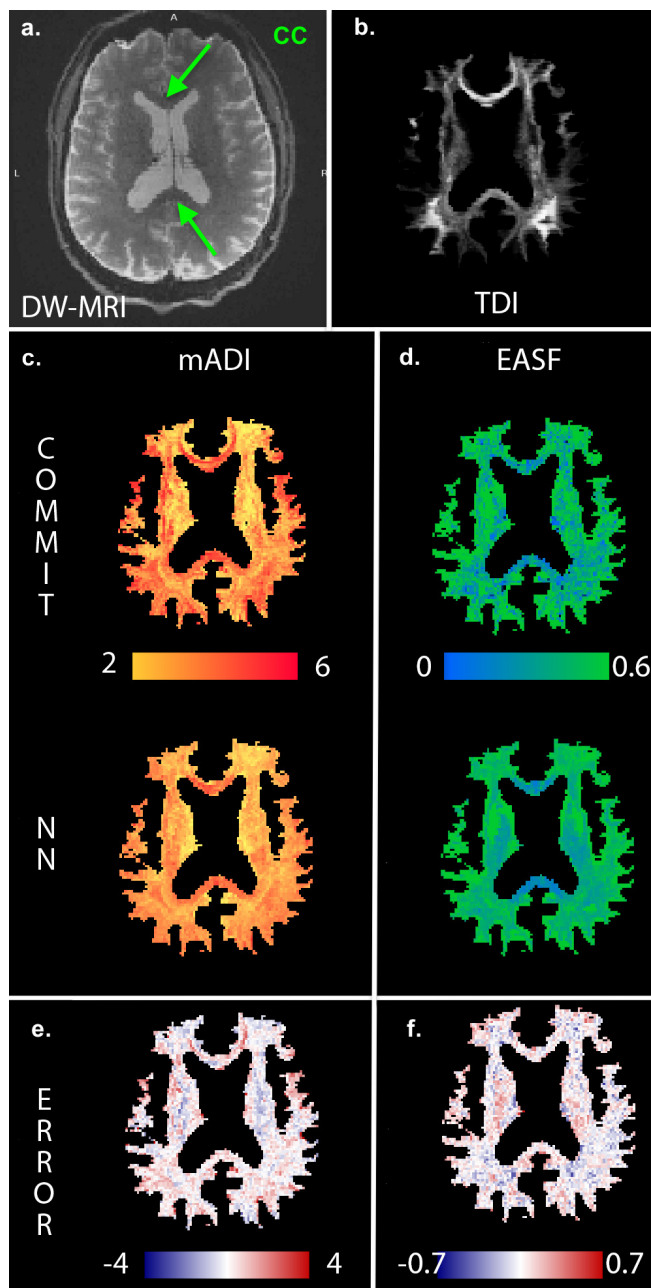


Figure A.2 – a) axial view of the  $b_0$  image. b) Track Density Imaging [51] (TDI) counting the number of tractography streamlines passing through each voxel. c) Top: mADI map estimated with COMMIT; bottom: mADI map estimated with the neural network (NN). d) Top: EASF map estimated with COMMIT; bottom: EASF estimated with the NN. e) Map of the difference between the mADI estimated with COMMIT and with the NN. f) Map of the difference between EASF estimated with COMMIT and with the NN.

## **A.4 Discussion**

**Limitation and future work:** The presented work is exploratory, and further experiments will be carried out in order to address some limitations, such as the quality of the microstructure maps.

The axon diameter maps estimated are limited by the diffusion data used. Better microstructural estimation could be achieved using data with higher diffusion gradients and more sensitivity sequences. The work is not intended to show improvements in axon diameter estimation, but, a way to speed up the COMMIT's fitting.

The main message of this preliminary work is to show that the global COMMIT estimates, which are global because they rely on the tractography regularization, could be achieved using a proper neural network and the input diffusion data, with no tractography involved.

Finally, a thorough comparison of the network's architecture and convergence, for instance, against more robust architectures as the one proposed in [272] will be considered in future work.

## **A.5 Conclusion**

In this work, we present a preliminary exploration of the use of learned sparse encoders in order to estimate tissue microstructure properties derived from a whole-brain tractography informed microstructure framework, i.e., COMMIT. The first advantage of the proposed method is the speed up in computation time of the microstructure maps from several hours for COMMIT to a few seconds. The second advantage is that the learned network can compute the microstructure maps directly from the raw DW-MRI data, and thus, it does not require the use of tractography methods.

Finally, the results presented in this work shows the feasibility of neural networks approach to estimate microstructure informed tractography derived scalar maps.

# Bibliography

- [1] (2014). Pearson Product Moment Correlation. In *Encyclopedia of Quality of Life and Well-Being Research*.
- [2] Aboitiz, F., Scheibel, A. B., Fisher, R. S., and Zaidel, E. (1992). Fiber composition of the human corpus callosum. *Brain Research*.
- [3] Alexander, A. L., Lee, J. E., Lazar, M., and Field, A. S. (2007). Diffusion Tensor Imaging of the Brain. *Neurotherapeutics*.
- [4] Alexander, D., Dyrby, T., Nilsson, M., and Zhang, H. (2017). Imaging brain microstructure with diffusion MRI: practicality and applications. *NMR Biomed*.
- [5] Alexander, D., Hubbard, P., Hall, M., Moore, E., Ptito, M., Parker, G., and Dyrby, T. (2010). Orientationally invariant indices of axon diameter and density from diffusion MRI. *NeuroImage*.
- [6] Alexander, D. and Jones, D. (2007). Limits on measuring axon diameters in vivo using diffusion MRI. In *Proceedings of the 15th Scientific Meeting of ISMRM*, p. 1541.
- [7] Alexander, D. C., Barker, G. J., and Arridge, S. R. (2002). Detection and modeling of non-Gaussian apparent diffusion coefficient profiles in human brain data. *Magnetic Resonance in Medicine*.
- [8] Anderson, A. W. (2005). Measurement of fiber orientation distributions using high angular resolution diffusion imaging. *Magnetic Resonance in Medicine*.
- [9] Ando, K., Laborde, Q., Lazar, A., Godefroy, D., Youssef, I., Amar, M., Pooler, A., Potier, M. C., Delatour, B., and Duyckaerts, C. (2014). Inside Alzheimer brain with CLARITY: Senile plaques, neurofibrillary tangles and axons in 3-D. In *Acta Neuropathologica*.
- [10] Annese, J. (2012). The importance of combining MRI and large-scale digital histology in neuroimaging studies of brain connectivity and disease. *Frontiers in Neuroinformatics*.
- [11] Archer, D. B., Vaillancourt, D. E., and Coombes, S. A. (2018). A Template and Probabilistic Atlas of the Human Sensorimotor Tracts using Diffusion MRI. *Cerebral cortex (New York, N.Y. : 1991)*.

## Bibliography

---

- [12] Arslan, S., Ktena, S. I., Makropoulos, A., Robinson, E. C., Rueckert, D., and Parisot, S. (2018). Human brain mapping: A systematic comparison of parcellation methods for the human cerebral cortex. *NeuroImage*.
- [13] Assaf, Y., Alexander, D., Jones, D., Bizzi, A., Behrens, T., Clark, C., Cohen, Y., Dyrby, T., Huppi, P., Knoesche, T., Lebihan, D., Parker, G., Poupon, C., Anaby, D., Anwander, A., Bar, L., Barazany, D., Blumenfeld-Katzir, T., Santis, S. D., Duclap, D., Figini, M., Fischi, E., Guevara, P., Hubbard, P., Hofstetter, S., Jbabdi, S., Kunz, N., Lazeyras, F., Lebois, A., Liptrot, M., Lundell, H., Mangin, J., Dominguez, D., Morozov, D., Schreiber, J., Seunarine, K., Nava, S., Poupon, C., Riffert, T., Sasson, E., Schmitt, B., Shemesh, N., Sotiropoulos, S., TavorI, I., Zhang, H., and Zhou, F. (2013). The CONNNECT project: Combining macro- and micro-structure. *Neuroimage*, 80:273–82.
- [14] Assaf, Y., Blumenfeld-Katzir, T., Yovel, Y., and Basser, P. J. (2008). AxCaliber: A method for measuring axon diameter distribution from diffusion MRI. *Magnetic Resonance in Medicine*.
- [15] Assaf, Y., Freidlin, R., and Basser, P. (2005). The measurement of the axon diameter distribution in white matter using diffusion MR methods. *In Proceedings of the 13th Scientific Meeting of ISMRM*.
- [16] Auria, A., Romascano, D., Canales-Rodriguez, E., Wiaux, Y., Dirby, T. B., Alexander, D., Thiran, J., and Daducci, A. (2015). Accelerated microstructure imaging via convex optimisation for regions with multiple fibres (AMICOx). *2015 IEEE International Conference on Image Processing (ICIP)*.
- [17] Auzias, G., Coulon, O., and Brovelli, A. (2016). MarsAtlas: A cortical parcellation atlas for functional mapping. *Human Brain Mapping*.
- [18] Axer, M., Strohmer, S., Gräßel, D., Bücker, O., Dohmen, M., Reckfort, J., Zilles, K., and Amunts, K. (2016). Estimating fiber orientation distribution functions in 3D-Polarized Light Imaging. *Frontiers in Neuroanatomy*.
- [19] Azadbakht, H., Parkes, L. M., Haroon, H. A., Augath, M., Logothetis, N. K., De Crespigny, A., D’Arceuil, H. E., and Parker, G. J. (2015). Validation of high-resolution tractography against in Vivo tracing in the macaque visual cortex. *Cerebral Cortex*.
- [20] Bachelier, L. (1900). Theorie de la speculation. *Annales scientifiques de l’Ecole Normale Supérieure*, 3e serie, 17:21–86.
- [21] Bammer, R., Acar, B., and Moseley, M. E. (2003). In vivo MR tractography using diffusion imaging. *European Journal of Radiology*.
- [22] Bansal, R., Gerber, A. J., and Peterson, B. S. (2008). Brain morphometry using anatomical magnetic resonance imaging. *Journal of the American Academy of Child and Adolescent Psychiatry*.

- [23] Barakovic, M., Romascano, D., Dyrby, T., Alexander, D., Descoteaux, M., Thiran, J.-P., and Daducci, A. (2016). Assessment of bundle-specific axon diameter distributions using diffusion mri tractography. In *Proc. 22nd Annual Meeting of the Organization for Human Brain Mapping (OHBM)*.
- [24] Barakovic, M., Romascano, D., Girard, G., Descoteaux, M., Thiran, J.-P., and Daducci, A. (2017). In-vivo bundle-specific axon diameter distributions estimation across the corpus callosum. In *Proc. 25nd Annual Meeting of the International Society for Magnetic Resonance in Medicine (ISMRM)*.
- [25] Barazany, D., Basser, P. J., and Assaf, Y. (2009). In vivo measurement of axon diameter distribution in the corpus callosum of rat brain. *Brain*.
- [26] Basser, P., Pajevic, S., Pierpaoli, C., Duda, J., and Aldroubi, A. (2000). In vivo fiber tractography using DT-MRI data. *Magnetic Resonance in Medicine*, 44(4):625–632.
- [27] Basser, P. J. (1998). Fiber-Tractography via Diffusion Tensor MRI (DT-MRI). *Proc. International Society for Magnetic Resonance in Medicine*.
- [28] Basser, P. J., Mattiello, J., and Lebihan, D. (1994). Estimation of the Effective Self-Diffusion Tensor from the NMR Spin Echo. *Journal of Magnetic Resonance, Series B*.
- [29] Basser, P. J. and Özarslan, E. (2013). Introduction to Diffusion MR. In *Diffusion MRI: From Quantitative Measurement to In vivo Neuroanatomy: Second Edition*.
- [30] Basser, P. J. and Pierpaoli, C. (1996). Microstructural and physiological features of tissues elucidated by quantitative-diffusion-tensor MRI. *Journal of Magnetic Resonance - Series B*.
- [31] Bastiani, M., Shah, N. J., Goebel, R., and Roebroeck, A. (2012). Human cortical connectome reconstruction from diffusion weighted MRI: The effect of tractography algorithm. *NeuroImage*.
- [32] Beaulieu, C., Fenrich, F. R., and Allen, P. S. (1998). Multicomponent water proton transverse relaxation and T2-discriminated water diffusion in myelinated and nonmyelinated nerve. *Magnetic Resonance Imaging*.
- [33] Behrens, T., Berg, H. J., Jbabdi, S., Rushworth, M., and Woolrich, M. (2007). Probabilistic diffusion tractography with multiple fibre orientations: What can we gain? *NeuroImage*, 34(1):144–155.
- [34] Behrens, T. E., Woolrich, M. W., Jenkinson, M., Johansen-Berg, H., Nunes, R. G., Clare, S., Matthews, P. M., Brady, J. M., and Smith, S. M. (2003). Characterization and Propagation of Uncertainty in Diffusion-Weighted MR Imaging. *Magnetic Resonance in Medicine*.
- [35] Benjamini, D. and Basser, P. J. (2016). Use of marginal distributions constrained optimization (MADCO) for accelerated 2D MRI relaxometry and diffusometry. *Journal of Magnetic Resonance*.

## Bibliography

---

- [36] Benjamini, D., Komlosh, M., Holtzclaw, L., Nevo, U., and Basser, P. (2016). White matter microstructure from nonparametric axon diameter distribution mapping. *NeuroImage*, 135:333–344.
- [37] Bennett, K. M., Schmainda, K. M., Bennett, R., Rowe, D. B., Lu, H., and Hyde, J. S. (2003). Characterization of continuously distributed cortical water diffusion rates with a stretched-exponential model. *Magnetic Resonance in Medicine*.
- [38] Berger, D. R., Seung, H. S., and Lichtman, J. W. (2018). VAST (Volume Annotation and Segmentation Tool): Efficient Manual and Semi-Automatic Labeling of Large 3D Image Stacks. *Frontiers in Neural Circuits*.
- [39] Bernal, B. and Altman, N. (2010). The connectivity of the superior longitudinal fasciculus: A tractography DTI study. *Magnetic Resonance Imaging*.
- [40] Bigun, J. and Granlund, G. H. (1987). Optimal orientation detection of linear symmetry. In *Proceedings of the IEEE First International Conference On Computer Vision*.
- [41] Bihan, D. L. (2003). Looking at the functional architecture of the brain with diffusion {MRI}. *Nature Reviews Neuroscience*.
- [Blender Online Community] Blender Online Community. *Blender - a 3D modelling and rendering package*. Blender Foundation, Blender Institute, Amsterdam.
- [43] Bloch, F., Hansen, W. W., and Packard, M. (1946). The nuclear induction experiment. *Physical Review*.
- [44] Brown, R. (1828). A brief account of microscopical observations made in the months of june, july and august 1827, on the particles contained in the pollen of plants; and on the general existence of active molecules in organic and inorganic bodies. *Philosophical Magazine*, 4(21):161–173.
- [45] Budde, M. D. and Frank, J. A. (2012). Examining brain microstructure using structure tensor analysis of histological sections. *NeuroImage*.
- [46] Burcaw, L., Fieremans, E., and Novikov, D. (2015). Mesoscopic structure of neuronal tracts from time-dependent diffusion. *NeuroImage*, 114:18–37.
- [47] Bürgel, U., Mädler, B., Honey, C. R., Thron, A., Gilsbach, J., and Coenen, V. A. (2009). Fiber tracking with distinct software tools results in a clear diversity in anatomical fiber tract portrayal. *Central European Neurosurgery*.
- [48] Buxton, R. B. (2009). *Introduction to Functional Magnetic Resonance Imaging: Principles and Techniques*. Cambridge University Press, 2 edition.
- [49] Calabrese, E. (2016). Diffusion Tractography in Deep Brain Stimulation Surgery: A Review. *Frontiers in Neuroanatomy*.



- [50] Calabrese, E., Badea, A., Coe, C. L., Lubach, G. R., Shi, Y., Styner, M. A., and Johnson, G. A. (2015). A diffusion tensor MRI atlas of the postmortem rhesus macaque brain. *NeuroImage*.
- [51] Calamante, F., Tournier, J.-D., Jackson, G. D., and Connelly, A. (2010). Track-density imaging (TDI): Super-resolution white matter imaging using whole-brain track-density mapping. *NeuroImage*, 53(4):1233–1243.
- [52] Callaghan, P. (1991). *Principles of Nuclear Magnetic Resonance Microscopy*. Oxford Science Publications.
- [53] Callaghan, P., Jolley, K., and Humphrey, R. (1983). Diffusion of fat and water in cheese as studied by pulsed field gradient nuclear magnetic resonance. *Journal of Colloid and Interface Science*, 93(2):521–529.
- [54] Caminiti, R., Carducci, F., Piervincenzi, C., Battaglia-Mayer, A., Confalone, G., Visco-Comandini, E., Pantano, P., and Innocenti, G. (2013). Diameter Length, Speed, and Conduction Delay of Callosal Axons in Macaque Monkeys and Humans: Comparing Data from Histology and Magnetic Resonance Imaging Diffusion Tractography. *Journal of Neuroscience*, 33(36):14501–14511.
- [55] Caminiti, R., Ghaziri, H., Galuske, R., Hof, P. R., and Innocenti, G. M. (2009). Evolution amplified processing with temporally dispersed slow neuronal connectivity in primates. *Proceedings of the National Academy of Sciences*.
- [56] Canales-Rodriguez, E., Pizzolato, M., Aleman-Gomez, Y., Kunz, N., Pot, C., Thiran, J. P., and Daducci, A. (2018). Unified multi-modal characterization of microstructural parameters of brain tissue using diffusion MRI and multi-echo T2 data. In *ISMRM 2018*.
- [57] Canales-Rodriguez, E. J., Legarreta, J. H., Pizzolato, M., Rensonnet, G., Girard, G., Patino, J. R., Barakovic, M., Romascano, D., Aleman-Gomez, Y., Radua, J., Pomarol-Clotet, E., Salvador, R., Thiran, J. P., and Daducci, A. (2019). Sparse wars: A survey and comparative study of spherical deconvolution algorithms for diffusion MRI. *NeuroImage*.
- [58] Carr, H. Y. and Purcell, E. M. (1954). Effects of diffusion on free precession in nuclear magnetic resonance experiments. *Physical Review*.
- [59] Carus, T. L. and Trevelyan, R. C. (2014). *De rerum natura*. Cambridge University Press.
- [60] Catani, M., Mesulam, M. M., Jakobsen, E., Malik, F., Martersteck, A., Wieneke, C., Thompson, C. K., Thiebaut De Schotten, M., Dell’Acqua, F., Weintraub, S., and Rogalski, E. (2013). A novel frontal pathway underlies verbal fluency in primary progressive aphasia. *Brain*.
- [61] Catani, M. and Thiebaut de Schotten, M. (2008). A diffusion tensor imaging tractography atlas for virtual in vivo dissections. *Cortex*.
- [62] Choe, A. S., Stepniewska, I., Colvin, D. C., Ding, Z., and Anderson, A. W. (2012). Validation of diffusion tensor MRI in the central nervous system using light microscopy: Quantitative comparison of fiber properties. *NMR in Biomedicine*.

## Bibliography

---

- [63] Christiaens, D., Reisert, M., Dhollander, T., Sunaert, S., Suetens, P., and Maes, F. (2015). Global tractography of multi-shell diffusion-weighted imaging data using a multi-tissue model. *NeuroImage*.
- [64] Chung, K., Wallace, J., Kim, S. Y., Kalyanasundaram, S., Andalman, A. S., Davidson, T. J., Mirzabekov, J. J., Zalocusky, K. A., Mattis, J., Denisin, A. K., Pak, S., Bernstein, H., Ramakrishnan, C., Grosenick, L., Gradinaru, V., and Deisseroth, K. (2013). Structural and molecular interrogation of intact biological systems. *Nature*.
- [65] Ciccarelli, O., Catani, M., Johansen-Berg, H., Clark, C., and Thompson, A. (2008). Diffusion-based tractography in neurological disorders: concepts, applications, and future developments. *The Lancet. Neurology*.
- [66] Conturo, T. E., Lori, N. F., Cull, T. S., Akbudak, E., Snyder, A. Z., Shimony, J. S., McKinstry, R. C., Burton, H., and Raichle, M. E. (1999). Tracking neuronal fiber pathways in the living human brain. *Proceedings of the National Academy of Sciences of the United States of America*.
- [67] Costantini, I., Ghobril, J. P., Di Giovanna, A. P., Allegra Mascaro, A. L., Silvestri, L., Müllenbroich, M. C., Onofri, L., Conti, V., Vanzi, F., Sacconi, L., Guerrini, R., Markram, H., Iannello, G., and Pavone, F. S. (2015). A versatile clearing agent for multi-modal brain imaging. *Scientific Reports*.
- [68] Cote, M.-A., Girard, G., Boré, A., Garyfallidis, E., Houde, J.-C., and Descoteaux, M. (2013). Tractometer: Towards validation of tractography pipelines. *Medical Image Analysis*, 17(7):844 – 857. Special Issue on the 2012 Conference on Medical Image Computing and Computer Assisted Intervention.
- [69] Craddock, R. C., James, G. A., Holtzheimer, P. E., Hu, X. P., and Mayberg, H. S. (2012). A whole brain fMRI atlas generated via spatially constrained spectral clustering. *Human brain mapping*.
- [70] Craddock, R. C., Jbabdi, S., Yan, C. G., Vogelstein, J. T., Castellanos, F. X., Di Martino, A., Kelly, C., Heberlein, K., Colcombe, S., and Milham, M. P. (2013). Imaging human connectomes at the macroscale. *Nature Methods*.
- [71] Crank, J. (1975). *The mathematics of diffusion, Second Edition*.
- [72] D. Barazany, D. Jones, Y. A. (2011). AxCaliber 3D. *In Proceedings of the 19th Scientific Meeting of ISMRM*.
- [73] Daducci, A., Canales-Rodriguez, E., Zhang, H., Dyrby, T., Alexander, D., and Thiran, J.-P. (2015a). Accelerated microstructure imaging via convex optimization (amico) from diffusion mri data. *NeuroImage*.
- [74] Daducci, A., Canales-Rodriguez, E. J., Descoteaux, M., Garyfallidis, E., Gur, Y., Lin, Y. C., Mani, M., Merlet, S., Paquette, M., Ramirez-Manzanares, A., Reisert, M., Rodrigues, P. R.,

- Sepehrband, F., Caruyer, E., Choupan, J., Deriche, R., Jacob, M., Menegaz, G., Prckovska, V., Rivera, M., Wiaux, Y., and Thiran, J. P. (2014a). Quantitative comparison of reconstruction methods for intra-voxel fiber recovery from diffusion MRI. *IEEE Transactions on Medical Imaging*.
- [75] Daducci, A., Palù, A. D., Descoteaux, M., and Thiran, J. P. (2016). Microstructure informed tractography: Pitfalls and open challenges. *Frontiers in Neuroscience*.
- [76] Daducci, A., Palù, A. D., Lemkaddem, A., and Thiran, J. (2013). A convex optimization framework for global tractography. In *IEEE 10th International Symposium on Biomedical Imaging (ISBI)*.
- [77] Daducci, A., Palù, A. D., Lemkaddem, A., and Thiran, J. (2015b). Commit: Convex optimization modeling for microstructure informed tractography. *IEEE Transactions on Medical Imaging*.
- [78] Daducci, A., Van De Ville, D., Thiran, J. P., and Wiaux, Y. (2014b). Sparse regularization for fiber ODF reconstruction: From the suboptimality of l2 and l1 priors to l0. *Medical Image Analysis*.
- [79] Dale, A. M., Fischl, B., and Sereno, M. I. (1999). Cortical surface-based analysis: I. Segmentation and surface reconstruction. *NeuroImage*.
- [80] Dammers, J., Breuer, L., Axer, M., Kleiner, M., Eiben, B., Gräel, D., Dickscheid, T., Zilles, K., Amunts, K., Shah, N. J., and Pietrzyk, U. (2012). Automatic identification of gray and white matter components in polarized light imaging. *NeuroImage*.
- [81] Daubechies, I., Defrise, M., and De Mol, C. (2004). An iterative thresholding algorithm for linear inverse problems with a sparsity constraint. *Communications on Pure and Applied Mathematics*.
- [82] De Almeida Martins, J. P. and Topgaard, D. (2018). Multidimensional correlation of nuclear relaxation rates and diffusion tensors for model-free investigations of heterogeneous anisotropic porous materials. *Scientific Reports*.
- [83] de Manzano, Ö. and Ullén, F. (2018). Same Genes, different brains: Neuroanatomical differences between monozygotic twins discordant for musical training. *Cerebral Cortex*.
- [84] de Moivre, A. (1738). *The doctrine of Chances*.
- [85] De Santis, S., Assaf, Y., Jeurissen, B., Jones, D. K., and Roebroeck, A. (2016). T1 relaxometry of crossing fibres in the human brain. *NeuroImage*.
- [86] De Schotten, M. T., Dell'Acqua, F., Forkel, S. J., Simmons, A., Vergani, F., Murphy, D. G., and Catani, M. (2011). A lateralized brain network for visuospatial attention. *Nature Neuroscience*.

## Bibliography

---

- [87] Dell'Acqua, F. and Catani, M. (2012). Structural human brain networks: Hot topics in diffusion tractography.
- [88] Dell'Acqua, F., Simmons, A., Williams, S., and Catani, M. (2012). Can spherical deconvolution provide more information than fiber orientations? Hindrance modulated orientational anisotropy a true-tract specific index to characterize white matter diffusion. *Human Brain Mapping*, 34(10):2464–2483.
- [89] Delmarcelle, T. and Hesselink, L. (1992). Visualization of second order tensor fields and matrix data. In *Proceedings Visualization '92*, pages 316–323.
- [90] DeLuca, G. C., Ebers, G. C., and Esiri, M. M. (2004). Axonal loss in multiple sclerosis: A pathological survey of the corticospinal and sensory tracts. *Brain*.
- [91] Denk, W., Strickler, J. H., and Webb, W. W. (1990). Two-photon laser scanning fluorescence microscopy. *Science*.
- [92] Descoteaux, M. and Deriche, R. (2015). From local q-ball estimation to fibre crossing tractography. In *Handbook of Biomedical Imaging: Methodologies and Clinical Research*.
- [93] Descoteaux, M., Deriche, R., Knösche, T. R., and Anwander, A. (2009). Deterministic and probabilistic tractography based on complex fibre orientation distributions. *IEEE Transactions on Medical Imaging*.
- [94] Desikan, R. S., Ségonne, F., Fischl, B., Quinn, B. T., Dickerson, B. C., Blacker, D., Buckner, R. L., Dale, A. M., Maguire, R. P., Hyman, B. T., Albert, M. S., and Killiany, R. J. (2006). An automated labeling system for subdividing the human cerebral cortex on MRI scans into gyral based regions of interest. *NeuroImage*.
- [95] Destrieux, C., Fischl, B., Dale, A., and Halgren, E. (2010). Automatic parcellation of human cortical gyri and sulci using standard anatomical nomenclature. *NeuroImage*.
- [96] Dhital, B., Reisert, M., Kellner, E., and Kiselev, V. G. (2019). Intra-axonal diffusivity in brain white matter. *NeuroImage*.
- [97] Dice, L. R. (1945). Measures of the Amount of Ecologic Association Between Species. *Ecology*.
- [98] Dodt, H. U., Leischner, U., Schierloh, A., Jährling, N., Mauch, C. P., Deininger, K., Deussing, J. M., Eder, M., Zieglgänsberger, W., and Becker, K. (2007). Ultramicroscopy: Three-dimensional visualization of neuronal networks in the whole mouse brain. *Nature Methods*.
- [99] Does, M. D. (2018). Inferring brain tissue composition and microstructure via MR relaxometry.
- [100] Donahue, C. J., Sotiropoulos, S. N., Jbabdi, S., Hernandez-Fernandez, M., Behrens, T. E., Dyrby, T. B., Coalson, T., Kennedy, H., Knoblauch, K., Van Essen, D. C., and Glasser, M. F. (2016). Using Diffusion Tractography to Predict Cortical Connection Strength and Distance: A Quantitative Comparison with Tracers in the Monkey. *The Journal of Neuroscience*.

- [101] Drobnyak, I., Zhang, H., Ianus, A., Kaden, E., and Alexander, D. (2015). PGSE OGSE and sensitivity to axon diameter in diffusion MRI: Insight from a simulation study. *Magnetic Resonance in Medicine*, 75(2):688–700.
- [102] Duval, T., McNab, J., Setsompop, K., Witzel, T., Schneider, T., Huang, S., Keil, B., Klawiter, E., Wald, L., and Cohen-Adad, J. (2015). In vivo mapping of human spinal cord microstructure at 300mT/m. *Neuroimage*, 118:494–507.
- [103] Duval, T., Smith, V., Stikov, N., Klawiter, E., and Cohen-Adad, J. (2017). Scan-rescan of axcaliber, macromolecular tissue volume, and g-ratio in the spinal cord. *Magn Reson Med*.
- [104] Dyrby, T., Sogaard, L., Hall, M., Ptito, M., and Alexander, D. (2013). Contrast and stability of the axon diameter index from microstructure imaging with diffusion MRI. *Magn Reson Med*, 70:711–21.
- [105] Dyrby, T. B., Innocenti, G. M., Bech, M., and Lundell, H. (2018). Validation strategies for the interpretation of microstructure imaging using diffusion MRI. *NeuroImage*.
- [106] Dyrby, T. B., Søgaard, L. V., Parker, G. J., Alexander, D. C., Lind, N. M., Baaré, W. F. C., Hay-Schmidt, A., Eriksen, N., Pakkenberg, B., Paulson, O. B., and Jelsing, J. (2007). Validation of in vitro probabilistic tractography. *NeuroImage*.
- [107] Eickhoff, S. B., Yeo, B. T., and Genon, S. (2018). Imaging-based parcellations of the human brain.
- [108] Einstein, A. (1905). Über die von der molekularkinetischen theorie der warme geforderte bewegung von in ruhenden flüssigkeiten suspendierten teilchen. *Annalen der Physik*, 322(8):549–560.
- [109] Einstein, A. (1906). Zur theorie der brownschen bewegung. *Annalen der Physik*, 324(2):371–381.
- [110] Einstein, A. (1907). Theoretische bemerkungen über die brownsche bewegung. *Zeitschrift für Elektrochemie und angewandte physikalische Chemie*, 13(6):41–42.
- [111] Einstein, A. (1908). Elementare theorie der brownschen) bewegung. *Zeitschrift für Elektrochemie und angewandte physikalische Chemie*, 14(17):235–239.
- [112] Ertürk, A., Becker, K., Jährling, N., Mauch, C. P., Hojer, C. D., Egen, J. G., Hellal, F., Bradke, F., Sheng, M., and Dodt, H. U. (2012). Three-dimensional imaging of solvent-cleared organs using 3DISCO. *Nature Protocols*.
- [113] Fan, L., Li, H., Zhuo, J., Zhang, Y., Wang, J., Chen, L., Yang, Z., Chu, C., Xie, S., Laird, A. R., Fox, P. T., Eickhoff, S. B., Yu, C., and Jiang, T. (2016a). The Human Brainnetome Atlas: A New Brain Atlas Based on Connectional Architecture. *Cerebral Cortex*.

## Bibliography

---

- [114] Fan, Q., Witzel, T., Nummenmaa, A., Van Dijk, K., Van Horn, J., Drews, M., Somerville, L., Sheridan, M., Santillana, R., Snyder, J., Hedden, T., Shaw, E., Hollinshead, M., Renvall, V., Zanzonico, R., Keil, B., Cauley, S., Polimeni, J., Tisdall, D., Buckner, R., Van Wedeen, J., Wald, L., Toga, A., and Rosen, B. (2016b). MGH?USC Human Connectome Project datasets with ultra-high b-value diffusion MRI. *NeuroImage*.
- [115] Farooq, H., Xu, J., Nam, J., Keefe, D., Yacoub, E., Georgiou, T., and Lenglet, C. (2016). Microstructure Imaging of Crossing (MIX) White Matter Fibers from diffusion MRI. *Scientific Reports*, 6(1).
- [116] Fedorov, A., Beichel, R., Kalpathy-Cramer, J., Finet, J., Fillion-Robin, J. C., Pujol, S., Bauer, C., Jennings, D., Fennessy, F., Sonka, M., Buatti, J., Aylward, S., Miller, J. V., Pieper, S., and Kikinis, R. (2012). 3D Slicer as an image computing platform for the Quantitative Imaging Network. *Magnetic Resonance Imaging*.
- [117] Feigl, G. C., Hiergeist, W., Fellner, C., Schebesch, K. M. M., Doenitz, C., Finkenzeller, T., Brawanski, A., and Schlaier, J. (2014). Magnetic resonance imaging diffusion tensor tractography: Evaluation of anatomic accuracy of different fiber tracking software packages.
- [118] Felleman, D. J. and Van Essen, D. C. (1991). Distributed hierarchical processing in the primate cerebral cortex. *Cerebral Cortex*.
- [119] Fick, A. (1855). Ueber diffusion. *Annalen der Physik*, 170(1):59–86.
- [120] Fick, R., Sepasian, N., Pizzolato, M., Ianus, A., and Deriche, R. (2017). Assessing the feasibility of estimating axon diameter using diffusion models and machine learning. *2017 IEEE 14th International Symposium on Biomedical Imaging (ISBI 2017)*.
- [121] Fick, R. H. J., Wassermann, D., Caruyer, E., and Deriche, R. (2016). MAPL: Tissue microstructure estimation using Laplacian-regularized MAP-MRI and its application to HCP data. *NeuroImage*, 134(1):365–385.
- [122] Fiebach, J., Schellinger, P., Heiland, S., and Sartor, K. (2003). Conventional MRI Diffusion-weighted MRI (DWI) and Apparent Diffusion Coefficient (ADC). In *Stroke MRI*, pages 13–21. Steinkopff.
- [123] Fieremans, E., Burcaw, L., Lee, H., Lemberskiy, G., Veraart, J., and Novikov, D. (2016). In vivo observation and biophysical interpretation of time-dependent diffusion in human white matter. *NeuroImage*, 129:414–427.
- [124] Fieremans, E., Jensen, J. H., and Helpert, J. A. (2011). White matter characterization with diffusional kurtosis imaging. *NeuroImage*.
- [125] Fillard, P., Descoteaux, M., Goh, A., Gouttard, S., Jeurissen, B., Malcolm, J., Ramirez-Manzanares, A., Reisert, M., Sakaie, K., Tensaouti, F., Yo, T., Mangin, J.-F., and Poupon, C. (2011). Quantitative evaluation of 10 tractography algorithms on a realistic diffusion mr phantom. *NeuroImage*, 56(1):220 – 234.

- [126] Fillard, P., Poupon, C., and Mangin, J. F. (2009). A novel global tractography algorithm based on an adaptive spin glass model. In *Lecture Notes in Computer Science (including subseries Lecture Notes in Artificial Intelligence and Lecture Notes in Bioinformatics)*.
- [127] Firmin, L., Field, P., Maier, M., Kraskov, A., Kirkwood, P., Nakajima, K., Lemon, R., and Glickstein, M. (2014). Axon diameters and conduction velocities in the macaque pyramidal tract. *Journal of Neurophysiology*, 112(6):1229–1240.
- [128] Fischl, B., Van Der Kouwe, A., Destrieux, C., Halgren, E., Ségonne, F., Salat, D. H., Busa, E., Seidman, L. J., Goldstein, J., Kennedy, D., Caviness, V., Makris, N., Rosen, B., and Dale, A. M. (2004). Automatically Parcellating the Human Cerebral Cortex. *Cerebral Cortex*.
- [129] Forkel, S. J., Thiebaut de Schotten, M., Kawadler, J. M., Dell’Acqua, F., Danek, A., and Catani, M. (2014). The anatomy of fronto-occipital connections from early blunt dissections to contemporary tractography. *Cortex*.
- [130] Fourier, J. (1822). *Théorie analytique de la chaleur*.
- [131] Frank, L. R. (2002). Characterization of anisotropy in high angular resolution diffusion-weighted MRI. *Magnetic Resonance in Medicine*.
- [132] Friman, O., Farnebäck, G., and Westin, C. F. (2006). A Bayesian approach for stochastic white matter tractography. *IEEE Transactions on Medical Imaging*.
- [133] Gangolli, M., Holleran, L., Hee Kim, J., Stein, T. D., Alvarez, V., McKee, A. C., and Brody, D. L. (2017). Quantitative validation of a nonlinear histology-MRI coregistration method using generalized Q-sampling imaging in complex human cortical white matter. *NeuroImage*.
- [134] Garcia-Larrea, L. and Mauguière, F. (2018). Pain syndromes and the parietal lobe. In *Handbook of Clinical Neurology*.
- [135] Garyfallidis, E., Brett, M., Amirbekian, B., Rokem, A., Van Der Walt, S., Descoteaux, M., and Nimmo-Smith, I. (2014). Dipy, a library for the analysis of diffusion MRI data. *Frontiers in Neuroinformatics*.
- [136] Gasser, H. (1964). Mammalian Nerve Fibers. Nobel Lecture, December 12, 1945. *Physiology or Medicine 1942-1962*.
- [137] Gillespie, M. and Stein, R. (1983). The relationship between axon diameter myelin thickness and conduction velocity during atrophy of mammalian peripheral nerves. *Brain Research*, 259(1):41–56.
- [138] Girard, G., Daducci, A., Petit, L., Thiran, J.-P., Whittingstall, K., Deriche, R., Wassermann, D., and Descoteaux, M. (2017). AxTract: Toward microstructure informed tractography. *Human Brain Mapping*, 38(11):5485–5500.
- [139] Girard, G., Whittingstall, K., Deriche, R., and Descoteaux, M. (2014). Towards quantitative connectivity analysis: reducing tractography biases. *NeuroImage*.

## Bibliography

---

- [140] Glasser, M. F., Smith, S. M., Marcus, D. S., Andersson, J. L. R., Auerbach, E. J., Behrens, T. E. J., Coalson, T. S., Harms, M. P., Jenkinson, M., Moeller, S., Robinson, E. C., Sotiropoulos, S. N., Xu, J., Yacoub, E., Ugurbil, K., and Van Essen, D. C. (2016). The Human Connectome Project's neuroimaging approach. *Nature Neuroscience*, 19(9):1175–1187.
- [141] Gong, G., He, Y., Concha, L., Lebel, C., Gross, D. W., Evans, A. C., and Beaulieu, C. (2009). Mapping anatomical connectivity patterns of human cerebral cortex using in vivo diffusion tensor imaging tractography. *Cerebral Cortex*.
- [142] Gordon, E. M., Laumann, T. O., Adeyemo, B., Huckins, J. F., Kelley, W. M., and Petersen, S. E. (2016). Generation and Evaluation of a Cortical Area Parcellation from Resting-State Correlations. *Cerebral Cortex*.
- [143] Gousias, I. S., Rueckert, D., Heckemann, R. A., Dyet, L. E., Boardman, J. P., Edwards, A. D., and Hammers, A. (2008). Automatic segmentation of brain MRIs of 2-year-olds into 83 regions of interest. *NeuroImage*.
- [144] Graham, T. (1833). On the law of the diffusion of gases. *The London, Edinburgh, and Dublin Philosophical Magazine and Journal of Science*, 2(9):175–190.
- [145] Gregor, K. and LeCun, Y. (2010). Learning fast approximations of sparse coding. In *Proc. of the 27th International Conference on Machine Learning (ICML)*.
- [146] Haggqvist, G. (1937). Faseranalytische studien über die pyramidenbahn. *Acta Psychiatrica Scandinavica*.
- [147] Hagiwara, A., Hori, M., Yokoyama, K., Nakazawa, M., Ueda, R., Horita, M., Andica, C., Abe, O., and Aoki, S. (2017). Analysis of White Matter Damage in Patients with Multiple Sclerosis via a Novel In Vivo MR Method for Measuring Myelin Axons, and G-Ratio. *American Journal of Neuroradiology*, 38(10):1934–1940.
- [148] Hahn, E. L. (1950). Spin echoes. *Physical Review*.
- [149] Hama, H., Kurokawa, H., Kawano, H., Ando, R., Shimogori, T., Noda, H., Fukami, K., Sakaue-Sawano, A., and Miyawaki, A. (2011). Scale: A chemical approach for fluorescence imaging and reconstruction of transparent mouse brain. *Nature Neuroscience*.
- [150] Henssen, D. J., Mollink, J., Kurt, E., van Dongen, R., Bartels, R. H., Gräβel, D., Kozicz, T., Axer, M., and Van Cappellen van Walsum, A. M. (2018). Ex vivo visualization of the trigeminal pathways in the human brainstem using 11.7T diffusion MRI combined with microscopy polarized light imaging.
- [151] Hofer, S. and Frahm, J. (2006). Topography of the human corpus callosum revisited- Comprehensive fiber tractography using diffusion tensor magnetic resonance imaging. *NeuroImage*.
- [152] Hofer, S., Wang, X., Roeloffs, V., and Frahm, J. (2015). Single-shot T1 mapping of the corpus callosum: a rapid characterization of fiber bundle anatomy. *Frontiers in Neuroanatomy*.



- [153] Hoffmeister, B., Janig, W., and Lisney, S. (1991). A proposed relationship between circumference and conduction velocity of unmyelinated axons from normal and regenerated cat hindlimb cutaneous nerves. *Neuroscience*, 42(2):603–611.
- [154] Honey, C. J., Thivierge, J. P., and Sporns, O. (2010). Can structure predict function in the human brain?
- [155] Horowitz, A., Barazany, D., Tavor, I., Bernstein, M., Yovel, G., and Assaf, Y. (2014). In vivo correlation between axon diameter and conduction velocity in the human brain. *Brain Structure and Function*, 220(3):1777–1788.
- [156] Huang, S., Nummenmaa, A., Witzel, T., Duval, T., Cohen-Adad, J., Wald, L., and McNab, J. (2015). The impact of gradient strength on in vivo diffusion MRI estimates of axon diameter. *Neuroimage*, 106:464–72.
- [157] Huang, S., Tobyne, S., Nummenmaa, A., Witzel, T., Wald, L., McNab, J., and Klawiter, E. (2016). Characterization of axonal disease in patients with multiple sclerosis using High-Gradient- Diffusion MR imaging. *Radiology*.
- [158] Hursh, J. B. (1937). Conduction velocity and diameter of nerve fibers. *American Journal of Physiology-Legacy Content*.
- [159] Huth, A. G., De Heer, W. A., Griffiths, T. L., Theunissen, F. E., and Gallant, J. L. (2016). Natural speech reveals the semantic maps that tile human cerebral cortex. *Nature*.
- [160] Hutter, J., Slator, P. J., Christiaens, D., Teixeira, R. P. A., Roberts, T., Jackson, L., Price, A. N., Malik, S., and Hajnal, J. V. (2018). Integrated and efficient diffusion-relaxometry using ZEBRA. *Scientific Reports*.
- [161] Ingenhousz, J., Pierre-Theophile, B., and Stoupe, J.-G.-A. (1785). *Nouvelles experiences et observations sur divers objets de physique*. Chez P. Theophile Barrois le jeune, libraire, quai des Augustins, no. 18.
- [162] Innocenti, G. M. and Caminiti, R. (2017). Axon diameter relates to synaptic bouton size: structural properties define computationally different types of cortical connections in primates. *Brain Structure and Function*.
- [163] Innocenti, G. M., Caminiti, R., Rouiller, E. M., Knott, G., Dyrby, T. B., Descoteaux, M., and Thiran, J.-P. (2018a). Diversity of Cortico-descending Projections: Histological and Diffusion MRI Characterization in the Monkey. *Cerebral Cortex*.
- [164] Innocenti, G. M., Dyrby, T. B., Andersen, K. W., Rouiller, E. M., and Caminiti, R. (2016). The Crossed Projection to the Striatum in Two Species of Monkey and in Humans: Behavioral and Evolutionary Significance. *Cerebral Cortex*.
- [165] Innocenti, G. M., Dyrby, T. B., Girard, G., St-Onge, E., Thiran, J.-P., Daducci, A., and Descoteaux, M. (2018b). Topological principles and developmental algorithms might refine diffusion tractography. *Brain Structure and Function*.

## Bibliography

---

- [166] Innocenti, G. M., Vercelli, A., and Caminiti, R. (2013). The diameter of cortical axons depends both on the area of origin and target. *Cerebral Cortex*.
- [167] Jansons, K. M. and Alexander, D. C. (2003). Persistent angular structure: New insights from diffusion magnetic resonance imaging data. *Inverse Problems*.
- [168] Jbabdi, S. and Johansen-Berg, H. (2011). Tractography: where do we go from here? *Brain connectivity*.
- [169] Jbabdi, S., Sotiropoulos, S. N., Haber, S. N., Van Essen, D. C., and Behrens, T. E. (2015). Measuring macroscopic brain connections in vivo. *Nature Neuroscience*.
- [170] Jbabdi, S., Woolrich, M., Andersson, J., and Behrens, T. (2007). A Bayesian framework for global tractography. *NeuroImage*, 37(1):116–129.
- [171] Jelescu, I. O., Veraart, J., Fieremans, E., and Novikov, D. S. (2016). Degeneracy in model parameter estimation for multi-compartmental diffusion in neuronal tissue. *NMR in Biomedicine*.
- [172] Jenkinson, M., Beckmann, C. F., Behrens, T. E. J., Woolrich, M. W., and Smith, S. M. (2012). FSL - Review. *NeuroImage*.
- [173] Jensen, J. H., Helpert, J. A., Ramani, A., Lu, H., and Kaczynski, K. (2005). Diffusional kurtosis imaging: The quantification of non-Gaussian water diffusion by means of magnetic resonance imaging. *Magnetic Resonance in Medicine*.
- [174] Jensen, J. H., Russell Glenn, G., and Helpert, J. A. (2016). Fiber ball imaging. *NeuroImage*.
- [175] Jespersen, S. N., Kroenke, C. D., Østergaard, L., Ackerman, J. J., and Yablonskiy, D. A. (2007). Modeling dendrite density from magnetic resonance diffusion measurements. *NeuroImage*.
- [176] Jespersen, S. N., Leigland, L. A., Cornea, A., and Kroenke, C. D. (2012). Determination of axonal and dendritic orientation distributions within the developing cerebral cortex by diffusion tensor imaging. *IEEE Transactions on Medical Imaging*.
- [177] Jeurissen, B., Descoteaux, M., Mori, S., and A., L. (2017). Diffusion MRI fiber tractography of the brain. *NMR in Biomedicine*.
- [178] Jeurissen, B., Descoteaux, M., Mori, S., and Leemans, A. (2019). Diffusion MRI fiber tractography of the brain. *NMR in biomedicine*.
- [179] Jeurissen, B., Leemans, A., Tournier, J. D., Jones, D. K., and Sijbers, J. (2013). Investigating the prevalence of complex fiber configurations in white matter tissue with diffusion magnetic resonance imaging. *Human Brain Mapping*.
- [180] Johansen-Berg, H. and Behrens, T. E. (2006). Just pretty pictures? What diffusion tractography can add in clinical neuroscience.

- [181] Johansen-Berg, H., Behrens, T. E., Sillery, E., Ciccarelli, O., Thompson, A. J., Smith, S. M., and Matthews, P. M. (2005). Functional-anatomical validation and individual variation of diffusion tractography-based segmentation of the human thalamus. *Cerebral Cortex*.
- [182] Johansen-Berg, H. and Behrens, T. E. J. (2013). *Diffusion MRI: From Quantitative Measurement to In vivo Neuroanatomy: Second Edition*.
- [183] Jones, D. K. (2010). Diffusion MRI : theory, methods, and application. *Ned Tijdschr Geneeskd*.
- [184] Jones, D. K. and Cercignani, M. (2010). Twenty-five pitfalls in the analysis of diffusion MRI data. *NMR in Biomedicine*.
- [185] Jones, D. K., Knösche, T. R., and Turner, R. (2013). White matter integrity, fiber count, and other fallacies: The do's and don'ts of diffusion MRI. *NeuroImage*.
- [186] Jones, D. K. and Pierpaoli, C. (2005). Contribution of cardiac pulsation to variability of tractography results. In *ISMRM 13th Annual Meeting and Exhibition*.
- [187] Jovicich, J., Czanner, S., Greve, D., Haley, E., Van Der Kouwe, A., Gollub, R., Kennedy, D., Schmitt, F., Brown, G., MacFall, J., Fischl, B., and Dale, A. (2006). Reliability in multi-site structural MRI studies: Effects of gradient non-linearity correction on phantom and human data. *NeuroImage*.
- [188] Ju, T., Warren, J., Carson, J., Bello, M., Kakadiaris, I., Chiu, W., Thaller, C., and Eichele, G. (2006). 3D volume reconstruction of a mouse brain from histological sections using warp filtering. *Journal of Neuroscience Methods*.
- [189] Kaden, E., Kelm, N. D., Carson, R. P., Does, M. D., and Alexander, D. C. (2016a). Multi-compartment microscopic diffusion imaging. *NeuroImage*.
- [190] Kaden, E., Kruggel, F., and Alexander, D. C. (2016b). Quantitative mapping of the per-axon diffusion coefficients in brain white matter. *Magnetic Resonance in Medicine*.
- [191] Kakkar, L., Atkinson, D., Chan, R., Siow, B., Ianus, A., and Drobnjak, I. (2017). Sensitivity of OGSE ActiveAx to Microstructural Dimensions on a Clinical Scanner. In *Computational Diffusion MRI*, pages 85–97. Springer International Publishing.
- [192] Kellner, E., Dhital, B., Kiselev, V. G., and Reiser, M. (2016). Gibbs-ringing artifact removal based on local subvoxel-shifts. *Magnetic Resonance in Medicine*.
- [193] Khan, A. R., Cornea, A., Leigland, L. A., Kohama, S. G., Jespersen, S. N., and Kroenke, C. D. (2015). 3D structure tensor analysis of light microscopy data for validating diffusion MRI. *NeuroImage*.
- [194] Kim, D., Doyle, E. K., Wisnowski, J. L., Kim, J. H., and Haldar, J. P. (2017). Diffusion-relaxation correlation spectroscopic imaging: A multidimensional approach for probing microstructure. *Magnetic Resonance in Medicine*.

## Bibliography

---

- [195] Klein, S., Staring, M., Murphy, K., Viergever, M. A., and Pluim, J. P. (2010). Elastix: A toolbox for intensity-based medical image registration. *IEEE Transactions on Medical Imaging*.
- [196] Knösche, T. R., Anwander, A., Liptrot, M., and Dyrby, T. B. (2015). Validation of tractography: Comparison with manganese tracing. *Human Brain Mapping*.
- [197] Kreher, B. W., Mader, I., and Kiselev, V. G. (2008). Gibbs tracking: A novel approach for the reconstruction of neuronal pathways. *Magnetic Resonance in Medicine*.
- [198] LaMantia, A. and Rakic, P. (1994). Axon overproduction and elimination in the anterior commissure of the developing rhesus monkey. *The Journal of Comparative Neurology*, 340(3):328–336.
- [199] Lampinen, B., Szczepankiewicz, F., Noven, M., van Westen, D., Hansson, O., Englund, E., Martensson, J., Westin, C. F., and Nilsson, M. (2019). Searching for the neurite density with diffusion MRI: Challenges for biophysical modeling. *Human Brain Mapping*.
- [200] Laplace, P.-S. (1812). *Theorie analytique des probabilités*.
- [201] Lawes, I. N. C., Barrick, T. R., Murugam, V., Spierings, N., Evans, D. R., Song, M., and Clark, C. A. (2008). Atlas-based segmentation of white matter tracts of the human brain using diffusion tensor tractography and comparison with classical dissection. *NeuroImage*.
- [202] Lazar, M. (2010). Mapping brain anatomical connectivity using white matter tractography.
- [203] Lazar, M., Weinstein, D. M., Tsuruda, J. S., Hasan, K. M., Arfanakis, K., Meyerand, M. E., Badie, B., Rowley, H. A., Haughton, V., Field, A., and Alexander, A. L. (2003). White matter tractography using diffusion tensor deflection. *Human Brain Mapping*.
- [204] Le Bihan, D. (2012). Diffusion, confusion and functional MRI.
- [205] Le Bihan, D., Breton, E., Lallemand, D., Aubin, M. L., Vignaud, J., and Laval-Jeantet, M. (1988). Separation of diffusion and perfusion in intravoxel incoherent motion MR imaging. *Radiology*.
- [206] Le Bihan, D. and Iima, M. (2015). Diffusion magnetic resonance imaging: What water tells us about biological tissues. *PLoS Biology*.
- [207] Leclercq, D., Delmaire, C., Menjot de Champfleury, N., Chiras, J., and Lehericy, S. (2011). Diffusion tractography: Methods, validation and applications in patients with neurosurgical lesions.
- [208] Leemans, A., Jeurissen, B., Sijbers, J., and Jones, D. K. (2009). ExploreDTI: a graphical toolbox for processing, analyzing, and visualizing diffusion MR data. In *17th Annual Meeting of Intl Soc Mag Reson Med, Hawaii, USA*.

- [209] Leergaard, T. B., White, N. S., De Crespigny, A., Bolstad, I., D'Arceuil, H., Bjaalie, J. G., and Dale, A. M. (2010). Quantitative histological validation of diffusion MRI fiber orientation distributions in the rat brain. *PLoS ONE*.
- [210] Lefebvre, J., Castonguay, A., Pouliot, P., Descoteaux, M., and Lesage, F. (2017). Whole mouse brain imaging using optical coherence tomography: reconstruction, normalization, segmentation, and comparison with diffusion MRI. *NeuroPhotonics*.
- [211] Lemberskiy, G., Fieremans, E., Veraart, J., Deng, F.-M., Rosenkrantz, A. B., and Novikov, D. S. (2018). Characterization of Prostate Microstructure Using Water Diffusion and NMR Relaxation. *Frontiers in Physics*.
- [212] Lemkaddem, A., Skiöldebrand, D., Palú, A. D., Thiran, J. P., and Daducci, A. (2014). Global tractography with embedded anatomical priors for quantitative connectivity analysis. *Frontiers in Neurology*.
- [213] Lenglet, C., Campbell, J. S., Descoteaux, M., Haro, G., Savadjiev, P., Wassermann, D., Anwender, A., Deriche, R., Pike, G. B., Sapiro, G., Siddiqi, K., and Thompson, P. M. (2009). Mathematical methods for diffusion MRI processing. *NeuroImage*.
- [214] Leuze, C., Aswendt, M., Ferenczi, E., Liu, C. W., Hsueh, B., Goubran, M., Tian, Q., Steinberg, G., Zeineh, M. M., Deisseroth, K., and McNab, J. A. (2017). The separate effects of lipids and proteins on brain MRI contrast revealed through tissue clearing. *NeuroImage*.
- [215] Leuze, C. W., Anwender, A., Bazin, P. L., Dhital, B., Stüber, C., Reimann, K., Geyer, S., and Turner, R. (2014). Layer-specific intracortical connectivity revealed with diffusion MRI. *Cerebral Cortex*.
- [216] Li, L., Rilling, J., Preuss, T., Glasser, M., Damen, E., and Hu, X. (2012). Quantitative assessment of a framework for creating anatomical brain networks via global tractography. *NeuroImage*, 61(4):1017–1030.
- [217] Liewald, D., Miller, R., Logothetis, N., Wagner, H.-J., and Schüz, A. (2014). Distribution of axon diameters in cortical white matter: an electron-microscopic study on three human brains and a macaque. *Biological Cybernetics*, 108(5):541–557.
- [218] Liu, A. K., Hurry, M. E., Ng, O. T., DeFelice, J., Lai, H. M., Pearce, R. K., Wong, G. T., Chang, R. C., and Gentleman, S. M. (2016). Bringing CLARITY to the human brain: visualization of Lewy pathology in three dimensions. *Neuropathology and Applied Neurobiology*.
- [219] Liu, C., Bammer, R., Acar, B., and Moseley, M. E. (2004). Characterizing Non-Gaussian Diffusion by Using Generalized Diffusion Tensors. *Magnetic Resonance in Medicine*.
- [220] Mackay, A., Whittall, K., Adler, J., Li, D., Paty, D., and Graeb, D. (1994). In vivo visualization of myelin water in brain by magnetic resonance. *Magnetic Resonance in Medicine*.

## Bibliography

---

- [221] Maier-Hein, K. H., Neher, P. F., Houde, J. C., Côté, M. A., Garyfallidis, E., Zhong, J., Chamberland, M., Yeh, F. C., Lin, Y. C., Ji, Q., Reddick, W. E., Glass, J. O., Chen, D. Q., Feng, Y., Gao, C., Wu, Y., Ma, J., Renjie, H., Li, Q., Westin, C. F., Deslauriers-Gauthier, S., González, J. O. O., Paquette, M., St-Jean, S., Girard, G., Rheault, F., Sidhu, J., Tax, C. M., Guo, F., Mesri, H. Y., Dávid, S., Froeling, M., Heemskerk, A. M., Leemans, A., Boré, A., Pinsard, B., Bedetti, C., Desrosiers, M., Brambati, S., Doyon, J., Sarica, A., Vasta, R., Cerasa, A., Quattrone, A., Yeatman, J., Khan, A. R., Hodges, W., Alexander, S., Romascano, D., Barakovic, M., Auria, A., Esteban, O., Lemkaddem, A., Thiran, J. P., Cetingul, H. E., Odry, B. L., Mailhe, B., Nadar, M. S., Pizzagalli, F., Prasad, G., Villalon-Reina, J. E., Galvis, J., Thompson, P. M., Requejo, F. D. S., Laguna, P. L., Lacerda, L. M., Barrett, R., Dell'Acqua, F., Catani, M., Petit, L., Caruyer, E., Daducci, A., Dyrby, T. B., Holland-Letz, T., Hilgetag, C. C., Stieltjes, B., and Descoteaux, M. (2017). The challenge of mapping the human connectome based on diffusion tractography. *Nature Communications*.
- [222] Makris, N., Preti, M. G., Asami, T., Pelavin, P., Campbell, B., Papadimitriou, G. M., Kaiser, J., Baselli, G., Westin, C. F., Shenton, M. E., and Kubicki, M. (2013). Human middle longitudinal fascicle: Variations in patterns of anatomical connections. *Brain Structure and Function*.
- [223] Malcolm, J. G., Shenton, M. E., and Rathi, Y. (2010). Filtered multitensor tractography. *IEEE Transactions on Medical Imaging*.
- [224] Mandonnet, E., Sarubbo, S., and Petit, L. (2018). The Nomenclature of Human White Matter Association Pathways: Proposal for a Systematic Taxonomic Anatomical Classification. *Frontiers in Neuroanatomy*.
- [225] Mangin, J. F., Fillard, P., Cointepas, Y., Le Bihan, D., Frouin, V., and Poupon, C. (2013). Toward global tractography. *NeuroImage*.
- [226] Matthews, M. (1968). An electron microscopic study of the relationship between axon diameter and the initiation of myelin production in the peripheral nervous system. *The Anatomical Record*, 161(3):337–351.
- [227] McKinnon, E. T. and Jensen, J. H. (2019). Measuring intra-axonal T<sub>2</sub> in white matter with direction-averaged diffusion MRI. *Magnetic Resonance in Medicine*.
- [228] McKinnon, E. T., Jensen, J. H., Glenn, G. R., and Helpert, J. A. (2017). Dependence on b-value of the direction-averaged diffusion-weighted imaging signal in brain. *Magnetic Resonance Imaging*.
- [229] McNab, J. A., Edlow, B. L., Witzel, T., Huang, S. Y., Bhat, H., Heberlein, K., Feiweier, T., Liu, K., Keil, B., Cohen-Adad, J., Tisdall, M. D., Folkerth, R. D., Kinney, H. C., and Wald, L. L. (2013a). The Human Connectome Project and beyond: Initial applications of 300mT/m gradients. *NeuroImage*.

- [230] McNab, J. A., Jbabdi, S., Deoni, S. C. L., Douaud, G., Behrens, T. E. J., and Miller, K. L. (2009). High resolution diffusion-weighted imaging in fixed human brain using diffusion-weighted steady state free precession. *NeuroImage*.
- [231] McNab, J. A., Polimeni, J. R., Wang, R., Augustinack, J. C., Fujimoto, K., Stevens, A., Janssens, T., Farivar, R., Folkerth, R. D., Vanduffel, W., and Wald, L. L. (2013b). Surface based analysis of diffusion orientation for identifying architectonic domains in the in vivo human cortex. *NeuroImage*.
- [232] Meola, A., Comert, A., Yeh, F. C., Stefanescu, L., and Fernandez-Miranda, J. C. (2015). The controversial existence of the human superior fronto-occipital fasciculus: Connectome-based tractographic study with microdissection validation. *Human Brain Mapping*.
- [233] Mercredi, M., Vincent, T., Bidinosti, C., and Martin, M. (2016). Assessing the accuracy of using oscillating gradient spin echo sequences with AxCaliber to infer micron-sized axon diameters. *Magnetic Resonance Materials in Physics Biology and Medicine*, 30(1):1–14.
- [234] Miller, K. L., Stagg, C. J., Douaud, G., Jbabdi, S., Smith, S. M., Behrens, T. E., Jenkinson, M., Chance, S. A., Esiri, M. M., Voets, N. L., Jenkinson, N., Aziz, T. Z., Turner, M. R., Johansen-Berg, H., and McNab, J. A. (2011). Diffusion imaging of whole, post-mortem human brains on a clinical MRI scanner. *NeuroImage*.
- [235] Mollink, J., Kleinnijenhuis, M., van Cappellen van Walsum, A. M., Sotiropoulos, S. N., Cottaar, M., Mirfin, C., Heinrich, M. P., Jenkinson, M., Pallebage-Gamarallage, M., Ansoorge, O., Jbabdi, S., and Miller, K. L. (2017). Evaluating fibre orientation dispersion in white matter: Comparison of diffusion MRI, histology and polarized light imaging. *NeuroImage*.
- [236] Morawski, M., Kirilina, E., Scherf, N., Jäger, C., Reimann, K., Trampel, R., Gavriilidis, E., Geyer, S., Biedermann, B., Arendt, T., and Weiskopf, N. (2018). Developing 3D microscopy with CLARITY on human brain tissue: Towards a tool for informing and validating MRI-based histology. *NeuroImage*.
- [237] Morecraft, R. J., Binneboese, A., Stilwell-Morecraft, K. S., and Ge, J. (2017). Localization of orofacial representation in the corona radiata, internal capsule and cerebral peduncle in *Macaca mulatta*. *Journal of Comparative Neurology*.
- [238] Mori, S., Crain, B., Chacko, V., and Zijl, P. V. (1999). Three-dimensional tracking of axonal projections in the brain by magnetic resonance imaging. *Annals of Neurology*, 45(2):265–269.
- [239] Mori, S. and Van Zijl, P. C. (2002). Fiber tracking: Principles and strategies - A technical review.
- [240] Mueller, L., Rudrapatna, U., Tax, C., Wise, R., and Jones, D. K. (2019). Diffusion MRI with  $b=1000$  s/mm<sup>2</sup> at TE < 22 ms using single-shot spiral readout and ultra-strong gradients: Implications for microstructure imaging. In *ISMRM 2019*.

## Bibliography

---

- [241] Mukherjee, P., Berman, J. I., Chung, S. W., Hess, C. P., and Henry, R. G. (2008a). Diffusion tensor MR imaging and fiber tractography: Theoretic underpinnings.
- [242] Mukherjee, P., Chung, S. W., Berman, J. I., Hess, C. P., and Henry, R. G. (2008b). Diffusion tensor MR imaging and fiber tractography: Technical considerations. In *American Journal of Neuroradiology*.
- [243] Mukherjee, P. and McKinstry, R. C. (2006). Diffusion tensor imaging and tractography of human brain development.
- [244] Murray, E., Cho, J. H., Goodwin, D., Ku, T., Swaney, J., Kim, S. Y., Choi, H., Park, Y. G., Park, J. Y., Hubbert, A., McCue, M., Vassallo, S., Bakh, N., Frosch, M. P., Wedeen, V. J., Seung, H. S., and Chung, K. (2015). Simple, Scalable Proteomic Imaging for High-Dimensional Profiling of Intact Systems. *Cell*.
- [245] Nakamura, H. and Kanaseki, T. (1989). Topography of the corpus callosum in the cat. *Brain Research*, 485(1):171 – 175.
- [246] Nath, V., Schilling, K. G., Hainline, A. E., Huo, Y., Parvathaneni, P., Blaber, J. A., Rowe, M., Rodrigues, P., Prchkovska, V., Aydogan, D. B., Sun, W., Shi, Y., Parker, W. A., Ismail, A. A. O., Verma, R., Cabeen, R. P., Toga, A. W., Newton, A. T., Wasserthal, J., Neher, P., Maier-Hein, K., Savini, G., Palesi, F., Kaden, E., Wu, Y., He, J., Fen, Y., Barakovic, M., Romascano, D., Rafael-Patino, J., Frigo, M., Girard, G., Daducci, A., Thiran, J.-P., Paquette, M., Rheault, F., Sidhu, J., Lebel, C., Leemans, A., Descoteaux, M., Dyrby, T. B., Kang, H., and A. Landman, B. (2019). Tractography Reproducibility Challenge with Empirical Data (TraCED): The 2017 ISMRM Diffusion Study Group Challenge. *Journal of Magnetic Resonance Imaging*.
- [247] Nedjati-Gilani, G., Schneider, T., Hall, M., Cawley, N., Hill, I., Ciccarelli, O., Drobnyak, I., Wheeler-Kingshott, C. G., and Alexander, D. (2017). Machine learning based compartment models with permeability for white matter microstructure imaging. *NeuroImage*, 150:119–135.
- [248] Neuman, C. (1974). Spin echo of spins diffusing in a bounded medium. *The Journal of Chemical Physics*, 60(11):4508–4511.
- [249] Nilsson, M., Lasič, S., Drobnyak, I., Topgaard, D., and Westin, C. F. (2017). Resolution limit of cylinder diameter estimation by diffusion MRI: The impact of gradient waveform and orientation dispersion. *NMR in Biomedicine*.
- [250] Nilsson, M., Latt, J., Stahlberg, F., Westin, D., and Haglslatt, H. (2011). The importance of axonal undulation in diffusion MR measurements: a Monte Carlo simulation study. *NMR in Biomedicine*, 25(5):795–805.
- [251] Nimsy, C., Bauer, M., and Carl, B. (2016). Merits and Limits of Tractography Techniques for the Uninitiated.



- [252] Ning, L., Gagoski, B., Szczepankiewicz, F., Westin, C.-F., and Rathi, Y. (2019). Joint RELaxation-Diffusion Imaging Moments (REDIM) to probe neurite microstructure. *bioRxiv*.
- [253] Novikov, D. S., Kiselev, V. G., and Jespersen, S. N. (2018). On modeling.
- [254] Nucifora, P. G. P., Verma, R., Lee, S.-K., and Melhem, E. R. (2007). Diffusion-Tensor MR Imaging and Tractography: Exploring Brain Microstructure and Connectivity. *Radiology*.
- [255] Nunes, D., Cruz, T., Jespersen, S., and Shemesh, N. (2017). Mapping axonal density and average diameter using non-monotonic time-dependent gradient-echo MRI. *Journal of Magnetic Resonance*, 277:117–130.
- [256] O'Donnell, L. J., Suter, Y., Rigolo, L., Kahali, P., Zhang, F., Norton, I., Albi, A., Olubiyi, O., Meola, A., Essayed, W. I., Unadkat, P., Ciris, P. A., Wells, W. M., Rathi, Y., Westin, C. F., and Golby, A. J. (2017). Automated white matter fiber tract identification in patients with brain tumors. *NeuroImage: Clinical*.
- [257] O'Donnell, L. J. and Westin, C. F. (2011). An introduction to diffusion tensor image analysis.
- [258] Okada, T., Miki, Y., Fushimi, Y., Hanakawa, T., Kanagaki, M., Yamamoto, A., Urayama, S.-i., Fukuyama, H., Hiraoka, M., and Togashi, K. (2006). Diffusion-Tensor Fiber Tractography: Intraindividual Comparison of 3.0-T and 1.5-T MR Imaging. *Radiology*.
- [259] Ong, H. and Wehrli, F. (2010). Quantifying axon diameter and intra-cellular volume fraction in excised mouse spinal cord with q-space imaging. *NeuroImage*, 51(4):1360–1366.
- [260] Ong, H., Wright, A., Wehrli, S., Souza, A., Schwartz, E., Hwang, S., and Wehrli, F. (2008). Indirect measurement of regional axon diameter in excised mouse spinal cord with q-space imaging: Simulation and experimental studies. *NeuroImage*, 40(4):1619–1632.
- [261] Orlick, T. and Partington, J. (1988). Mental Links to Excellence. *The Sport Psychologist*.
- [262] Özarlan, E., Basser, P. J., Shepherd, T. M., Thelwall, P. E., Vemuri, B. C., and Blackband, S. J. (2006). Observation of anomalous diffusion in excised tissue by characterizing the diffusion-time dependence of the MR signal. *Journal of Magnetic Resonance*.
- [263] Özarlan, E., Koay, C., and Basser, P. (2008). Simple harmonic oscillator based estimation and reconstruction for one-dimensional q-space mr. In *Proc. ISMRM*.
- [264] Özarlan, E., Koay, C. G., Shepherd, T. M., Komlosh, M. E., İrfanoğlu, M. O., Pierpaoli, C., and Basser, P. J. (2013). Mean apparent propagator (MAP) MRI: A novel diffusion imaging method for mapping tissue microstructure. *NeuroImage*, 78:16–32.
- [265] Özarlan, E. and Mareci, T. H. (2003). Generalized Diffusion Tensor Imaging and Analytical Relationships Between Diffusion Tensor Imaging and High Angular Resolution Diffusion Imaging. *Magnetic Resonance in Medicine*.

## Bibliography

---

- [266] Packer, K. and Rees, C. (1972). Pulsed NMR studies of restricted diffusion. I. Droplet size distributions in emulsions. *Journal of Colloid and Interface Science*, 40(2):206–218.
- [267] Pajevic, S. and Basser, P. (2013). An Optimum Principle Predicts the Distribution of Axon Diameters in Normal White Matter. *PLoS ONE*, 8(1):e54095.
- [268] Panagiotaki, E., Schneider, T., Siow, B., Hall, M. G., Lythgoe, M. F., and Alexander, D. C. (2012). Compartment models of the diffusion MR signal in brain white matter: A taxonomy and comparison. *NeuroImage*.
- [269] Pasternak, O., Sochen, N., Gur, Y., Intrator, N., and Assaf, Y. (2009). Free water elimination and mapping from diffusion MRI. *Magnetic resonance in medicine*.
- [270] Paxinos G, Huang XF, Petrides M, T. A. (2009). The Rhesus Monkey Brain in Stereotaxic Coordinates.
- [271] Pearson, K. (1905). The problem of the random walk. *Nature*, 72:294.
- [272] Perdios, D., Besson, A., Rossinelli, P., and Thiran, J. (2017). Learning the weight matrix for sparsity averaging in compressive imaging. In *2017 IEEE International Conference on Image Processing (ICIP)*.
- [273] Perge, J. A., Niven, J. E., Mugnaini, E., Balasubramanian, V., and Sterling, P. (2012). Why Do Axons Differ in Caliber? *Journal of Neuroscience*.
- [274] Permeability, V.-d. M. and Permeability, V.-d. M. (2015). Increased Conduction Velocity as a Result of Myelination. *Neuroscience*.
- [275] Perrin, J. (1909). Mouvement brownien et réalité moléculaire. *Annales de Chimie et de Physique*.
- [276] Pestilli, F., Yeatman, J. D., Rokem, A., Kay, K. N., and Wandell, B. A. (2014). Evaluation and statistical inference for human connectomes. *Nature Methods*.
- [277] Peters, A., Palay, S., and Webster, H. (1991). *The fine structure of the nervous system: neurons and their supporting cells*. Oxford University Press.
- [278] Phillips, J., Laude, A., Lightowers, R., Morris, C. M., Turnbull, D. M., and Lax, N. Z. (2016). Development of passive CLARITY and immunofluorescent labelling of multiple proteins in human cerebellum: Understanding mechanisms of neurodegeneration in mitochondrial disease. *Scientific Reports*.
- [279] Pierpaoli, C. and Basser, P. J. (1996). Toward a quantitative assessment of diffusion anisotropy. *Magnetic Resonance in Medicine*.
- [280] Pierpaoli, C., Walker, L., Irfanoglu, M. O., Barnett, A., Basser, P. J., Chang, L.-C., Koay, C. G., Pajevic, S., Rohde, G., Sarlls, J. E., and Wu, M. (2010). TORTOISE: An Integrated Software Package for Processing of Diffusion MRI Data. In *ISMRM (2010) 18th Annual Meeting*.

- [281] Pizzolato, M., Canales-Rodriguez, E., Daducci, A., and Thiran, J. P. (2018). Multimodal microstructure imaging: joint T2-relaxometry and diffusometry to estimate myelin, intracellular, extracellular, and cerebrospinal fluid properties. In *ISMRM 2018*.
- [282] Polya, G. (1920). Uber den zentralen grenzwertsatz der wahrscheinlichkeitsrechnung und das momentenproblem. *Mathematische Zeitschrift*, 8:171–181.
- [283] Pujol, S., Wells, W., Pierpaoli, C., Brun, C., Gee, J., Cheng, G., Vemuri, B., Commowick, O., Prima, S., Stamm, A., Goubran, M., Khan, A., Peters, T., Neher, P., Maier-Hein, K. H., Shi, Y., Tristan-Vega, A., Veni, G., Whitaker, R., Styner, M., Westin, C. F., Gouttard, S., Norton, I., Chauvin, L., Mamata, H., Gerig, G., Nabavi, A., Golby, A., and Kikinis, R. (2015). The DTI Challenge: Toward Standardized Evaluation of Diffusion Tensor Imaging Tractography for Neurosurgery. *Journal of Neuroimaging*.
- [284] Qiu, T. M., Zhang, Y., and Wu, J. S. (2008). Preliminary application of pyramidal tractography in evaluating prognosis of patients with hypertensive intracerebral hemorrhage. *Acta Neurochirurgica, Supplementum*.
- [285] Rafael-Patino, J., Girard, G., Romascano, D., Barakovic, M., Rensonnet, G., Thiran, J. P., and Daducci, A. (2018). Realistic 3D Fiber Crossing Phantom Models for Monte Carlo Diffusion Simulations. In *ISMRM 2018*.
- [286] Raffelt, D., Tournier, J.-D., Rose, S., Ridgway, G. R., Henderson, R., Crozier, S., Salvado, O., and Connelly, A. (2012). Apparent Fibre Density: A novel measure for the analysis of diffusion-weighted magnetic resonance images. *NeuroImage*, 59(4):3976–94.
- [287] Reisert, M., Kiselev, V. G., Dihtal, B., Kellner, E., and Novikov, D. S. (2014). MesoFT: Unifying Diffusion Modelling and Fiber Tracking. In *International Conference on Medical Image Computing and Computer-Assisted Intervention*, pages 201–208, Boston, United-States.
- [288] Reisert, M., Mader, I., Anastasopoulos, C., Weigel, M., Schnell, S., and Kiselev, V. (2011). Global fiber reconstruction becomes practical. *NeuroImage*.
- [289] Renier, N., Wu, Z., Simon, D. J., Yang, J., Ariel, P., and Tessier-Lavigne, M. (2014). IDISCO: A simple, rapid method to immunolabel large tissue samples for volume imaging. *Cell*.
- [290] Rensonnet, G., Scherrer, B., Warfield, S. K., Macq, B., and Taquet, M. (2018). Assessing the validity of the approximation of diffusion-weighted-MRI signals from crossing fascicles by sums of signals from single fascicles. *Magnetic Resonance in Medicine*.
- [291] Reveley, C., Seth, A. K., Ye, F. Q., Yu, D., Leopold, D. A., Pierpaoli, C., Silva, A. C., and Saunders, R. C. (2015). Superficial white matter fiber systems impede detection of long-range cortical connections in diffusion MR tractography. *Proceedings of the National Academy of Sciences*.

## Bibliography

---

- [292] Rheault, F., St-Onge, E., Sidhu, J., Maier-Hein, K., Tzourio-Mazoyer, N., Petit, L., and Descoteaux, M. (2019). Bundle-specific tractography with incorporated anatomical and orientational priors. *NeuroImage*.
- [293] Richardson, D. S. and Lichtman, J. W. (2015). Clarifying Tissue Clearing. *Cell*.
- [294] Ritchie, J. (1982). On the Relation between Fibre Diameter and Conduction Velocity in Myelinated Nerve Fibres. *Proceedings of the Royal Society B: Biological Sciences*, 217(1206):29–35.
- [295] Roland, J., Snyder, A., Hacker, C., Mitra, A., Shimony, J., Limbrick, D., Raichle, M., Smyth, M., and Leuthardt, E. (2017). On the role of the corpus callosum in interhemispheric functional connectivity in humans. *Proc Natl Acad Sci U S A*, 114:13278–13283.
- [296] Romascano, D. (2018). *An examination of keystroke dynamics for continuous user authentication*. PhD thesis, EPFL.
- [297] Rowe, M., Zhang, H. G., Oxtoby, N., and Alexander, D. C. (2013). Beyond crossing fibers: Tractography exploiting sub-voxel fibre dispersion and neighbourhood structure. In *Lecture Notes in Computer Science (including subseries Lecture Notes in Artificial Intelligence and Lecture Notes in Bioinformatics)*.
- [298] Saleem, K. and Logothetis, N. (2006). *A Combined MRI and Histology Atlas of the Rhesus Monkey Brain in Stereotaxic Coordinates*. Elsevier Science.
- [299] Santis, S. D., Jones, D., and Roebroek, A. (2016). Including diffusion time dependence in the extra-axonal space improves in vivo estimates of axonal diameter and density in human white matter. *Neuroimage*, 130:91–103.
- [300] Schaefer, A., Kong, R., Gordon, E. M., Laumann, T. O., Zuo, X.-N., Holmes, A. J., Eickhoff, S. B., and Yeo, B. T. T. (2018). Local-Global Parcellation of the Human Cerebral Cortex from Intrinsic Functional Connectivity MRI. *Cerebral Cortex*.
- [301] Scherrer, B., Schwartzman, A., Taquet, M., Sahin, M., Prabhu, S. P., and Warfield, S. K. (2015). Characterizing brain tissue by assessment of the distribution of anisotropic microstructural environments in diffusion-compartment imaging (DIAMOND). *Magnetic Resonance in Medicine*, 76(3):963–977.
- [302] Schiavi, S., Barakovic, M., Pineda, M. O., Descoteaux, M., Thiran, J.-P., and Daducci, A. (2019a). Reducing false positives in tractography with microstructural and anatomical priors. *bioRxiv*.
- [303] Schiavi, S., Pizzolato, M., Ocampo-Pineda, M., Canales-Rodriguez, E., Jean-Philippe, T., and Alessandro, D. (2019b). Is it feasible to directly access the bundle’s specific myelin content, instead of averaging? A study with Microstructure Informed Tractography. *ISMRM 2019*.

- [304] Schilling, K., Gao, Y., Janve, V., Stepniewska, I., Landman, B. A., and Anderson, A. W. (2017). Can increased spatial resolution solve the crossing fiber problem for diffusion MRI? *NMR in Biomedicine*.
- [305] Schilling, K. G., Gao, Y., Stepniewska, I., Janve, V., Landman, B. A., and Anderson, A. W. (2019a). Anatomical accuracy of standard-practice tractography algorithms in the motor system - A histological validation in the squirrel monkey brain. *Magnetic Resonance Imaging*.
- [306] Schilling, K. G., Janve, V., Gao, Y., Stepniewska, I., Landman, B. A., and Anderson, A. W. (2018). Histological validation of diffusion MRI fiber orientation distributions and dispersion. *NeuroImage*.
- [307] Schilling, K. G., Nath, V., Hansen, C., Parvathaneni, P., Blaber, J., Gao, Y., Neher, P., Aydogan, D. B., Shi, Y., Ocampo-Pineda, M., Schiavi, S., Daducci, A., Girard, G., Barakovic, M., Rafael-Patino, J., Romascano, D., Rensonnet, G., Pizzolato, M., Bates, A., Fischl, E., Thiran, J. P., Canales-Rodriguez, E. J., Huang, C., Zhu, H., Zhong, L., Cabeen, R., Toga, A. W., Rheault, F., Theaud, G., Houde, J. C., Sidhu, J., Chamberland, M., Westin, C. F., Dyrby, T. B., Verma, R., Rathi, Y., Irfanoglu, M. O., Thomas, C., Pierpaoli, C., Descoteaux, M., Anderson, A. W., and Landman, B. A. (2019b). Limits to anatomical accuracy of diffusion tractography using modern approaches. *NeuroImage*.
- [308] Schindelin, J., Arganda-Carreras, I., Frise, E., Kaynig, V., Longair, M., Pietzsch, T., Preibisch, S., Rueden, C., Saalfeld, S., Schmid, B., Tinevez, J. Y., White, D. J., Hartenstein, V., Eliceiri, K., Tomancak, P., and Cardona, A. (2012). Fiji: An open-source platform for biological-image analysis.
- [309] Schmahmann, J. D. and Pandya, D. N. (2009). *Fiber Pathways of the Brain*. Oxford University Press.
- [310] Schonberg, T., Pianka, P., Hendler, T., Pasternak, O., and Assaf, Y. (2006). Characterization of displaced white matter by brain tumors using combined DTI and fMRI. *NeuroImage*.
- [311] Schroder, J. (1972). Altered ratio between axon diameter and myelin sheath thickness in regenerated nerve fibers. *Brain Research*, 45(1):49–65.
- [312] Seehaus, A., Roebroek, A., Bastiani, M., Fonseca, L., Bratzke, H., Lori, N., Vilanova, A., Goebel, R., and Galuske, R. (2015). Histological validation of high-resolution DTI in human post mortem tissue. *Frontiers in Neuroanatomy*.
- [313] Sepehrband, F., Alexander, D., Clark, K., Kurniawan, N., Yang, Z., and Reutens, D. (2016). Parametric Probability Distribution Functions for Axon Diameters of Corpus Callosum. *Frontiers in Neuroanatomy*, 10.
- [314] Setsompop, K., Kimmlingen, R., Eberlein, E., Witzel, T., Cohen-Adad, J., McNab, J., Keil, B., Tisdall, M., Hoecht, P., Dietz, P., Cauley, S., Tountcheva, V., Matschl, V., Lenz, V., Heberlein,

## Bibliography

---

- K., Potthast, A., Thein, H., Horn, J. V., Toga, A., Schmitt, F., Lehne, D., Rosen, B., Wedeen, V., and Wald, L. (2013). Pushing the limits of in vivo diffusion mri for the human connectome project. *NeuroImage*.
- [315] Seunarine, K. K. and Alexander, D. C. (2013). Multiple Fibers. Beyond the Diffusion Tensor. In *Diffusion MRI: From Quantitative Measurement to In vivo Neuroanatomy: Second Edition*.
- [316] Sherbondy, A. J., Dougherty, R. F., Ananthanarayanan, R., Modha, D. S., and Wandell, B. A. (2009). Think global, act local; projectome estimation with BlueMatter. In *Lecture Notes in Computer Science (including subseries Lecture Notes in Artificial Intelligence and Lecture Notes in Bioinformatics)*.
- [317] Sherbondy, A. J., Rowe, M. C., and Alexander, D. C. (2010). MicroTrack: An algorithm for concurrent projectome and microstructure estimation. In *Lecture Notes in Computer Science (including subseries Lecture Notes in Artificial Intelligence and Lecture Notes in Bioinformatics)*.
- [318] Sira, C. S. and Mateer, C. A. (2014). Frontal Lobes. In *Encyclopedia of the Neurological Sciences*.
- [319] Smith, R. E., Tournier, J. D., Calamante, F., and Connelly, A. (2012). Anatomically-constrained tractography: Improved diffusion MRI streamlines tractography through effective use of anatomical information. *NeuroImage*.
- [320] Smith, R. E., Tournier, J. D., Calamante, F., and Connelly, A. (2013). SIFT: Spherical-deconvolution informed filtering of tractograms. *NeuroImage*.
- [321] Smith, R. E., Tournier, J. D., Calamante, F., and Connelly, A. (2015). SIFT2: Enabling dense quantitative assessment of brain white matter connectivity using streamlines tractography. *NeuroImage*.
- [322] Sosnovik, D. E., Wang, R., Dai, G., Reese, T. G., and Wedeen, V. J. (2009). Diffusion MR tractography of the heart.
- [323] Sotiropoulos, S. N., Behrens, T. E., and Jbabdi, S. (2012). Ball and rackets: Inferring fiber fanning from diffusion-weighted MRI. *NeuroImage*.
- [324] Sotiropoulos, S. N. and Zalesky, A. (2017). Building connectomes using diffusion MRI: Why, how and but.
- [325] Spalteholz, W. (1914). *Über das Durchsichtigmachen von menschlichen und tierischen Präparaten. Leipzig: S. Hierzel.*
- [326] Sperry, R. (1982). Some effects of disconnecting the cerebral hemispheres - Nobel lecture, 8 December 1981. *Bioscience Reports*.
- [327] Squire, L. R. and Zola-Morgan, S. (1991). The medial temporal lobe memory system.

- [328] Stanisz, G. J., Odrobina, E. E., Pun, J., Escaravage, M., Graham, S. J., Bronskill, M. J., and Henkelman, R. M. (2005). T1, T2 relaxation and magnetization transfer in tissue at 3T. *Magnetic Resonance in Medicine*.
- [329] Stanisz, G. J., Szafer, A., Wright, G. A., and Henkelman, R. M. (1997). An analytical model of restricted diffusion in bovine optic nerve. *Magnetic Resonance in Medicine*.
- [330] Stejskal, E. O. and Tanner, J. E. (1965). Spin diffusion measurements: Spin echoes in the presence of a time-dependent field gradient. *The Journal of Chemical Physics*.
- [331] Stokes, G. (1951). On the effect of the internal friction of fluids on the motion of pendulums. *Transactions of the Cambridge Philosophical Society*, 9:8.
- [332] Szafer, A., Zhong, J., Anderson, A. W., and Gore, J. C. (1995). Diffusion weighted imaging in tissues: Theoretical models. *NMR in Biomedicine*.
- [333] Talos, I.-F., O'Donnell, L., Westin, C.-F., Warfield, S. K., Wells, W., Yoo, S.-S., Panych, L. P., Golby, A., Mamata, H., Maier, S. S., Ratiu, P., Guttman, C. R. G., Black, P. M., Jolesz, F. A., and Kikinis, R. (2003). Diffusion Tensor and Functional MRI Fusion with Anatomical MRI for Image-Guided Neurosurgery.
- [334] Tax, C., Rudrapatna, U., Witzel, T., and Jones, D. (2017). Disentangling in two dimensions in the living human brain: Feasibility of relaxometry-diffusometry using ultra-strong gradients. In *Proc. ISMRM*.
- [335] Thomas, C., Ye, F. Q., Irfanoglu, M. O., Modi, P., Saleem, K. S., Leopold, D. A., and Pierpaoli, C. (2014). Anatomical accuracy of brain connections derived from diffusion MRI tractography is inherently limited. *Proceedings of the National Academy of Sciences*.
- [336] Tomasi, S., Caminiti, R., and Innocenti, G. M. (2012). Areal differences in diameter and length of corticofugal projections. *Cerebral Cortex*.
- [337] Tomassini, V., Matthews, P. M., Thompson, A. J., Fuglo, D., Geurts, J. J., Johansen-Berg, H., Jones, D. K., Rocca, M. A., Wise, R. G., Barkhof, F., and Palace, J. (2012). Neuroplasticity and functional recovery in multiple sclerosis.
- [338] Tomer, R., Ye, L., Hsueh, B., and Deisseroth, K. (2014). Advanced CLARITY for rapid and high-resolution imaging of intact tissues. *Nature Protocols*.
- [339] Torrey, H. C. (1956). Bloch equations with diffusion terms. *Physical Review*.
- [340] Tournier, J. D., Calamante, F., and Connelly, A. (2007). Robust determination of the fibre orientation distribution in diffusion MRI: Non-negativity constrained super-resolved spherical deconvolution. *NeuroImage*.
- [341] Tournier, J. D., Calamante, F., and Connelly, A. (2012). MRtrix: Diffusion tractography in crossing fiber regions. *International Journal of Imaging Systems and Technology*.

## Bibliography

---

- [342] Tournier, J. D., Calamante, F., and Connelly, A. (2013). Determination of the appropriate b value and number of gradient directions for high-angular-resolution diffusion-weighted imaging. *NMR in Biomedicine*.
- [343] Tournier, J. D., Calamante, F., Gadian, D. G., and Connelly, A. (2004). Direct estimation of the fiber orientation density function from diffusion-weighted MRI data using spherical deconvolution. *NeuroImage*.
- [344] Tournier, J.-D., Smith, R. E., Raffelt, D., Tabbara, R., Dhollander, T., Pietsch, M., Christiaens, D., Jeurissen, B., Yeh, C.-H., and Connelly, A. (2019). MRtrix3: A fast, flexible and open software framework for medical image processing and visualisation. *bioRxiv*.
- [345] Tuch, D. S. (2004). Q-ball imaging. *Magnetic Resonance in Medicine*.
- [346] Tuch, D. S., Reese, T. G., Wiegell, M. R., Makris, N., Belliveau, J. W., and Van Wedeen, J. (2002). High angular resolution diffusion imaging reveals intravoxel white matter fiber heterogeneity. *Magnetic Resonance in Medicine*.
- [347] Tzourio-Mazoyer, N., Landeau, B., Papathanassiou, D., Crivello, F., Etard, O., Delcroix, N., Mazoyer, B., and Joliot, M. (2002). Automated anatomical labeling of activations in SPM using a macroscopic anatomical parcellation of the MNI MRI single-subject brain. *NeuroImage*.
- [348] Van Essen, D. C., Anderson, C. H., and Felleman, D. J. (1992). Information processing in the primate visual system: An integrated systems perspective.
- [349] Van Essen, D. C., Smith, S. M., Barch, D. M., Behrens, T. E., Yacoub, E., and Ugurbil, K. (2013). The WU-Minn Human Connectome Project: An overview. *NeuroImage*.
- [350] Vangelder, P., Despres, D., Vanzijl, P., and Moonen, C. (1994). Evaluation of Restricted Diffusion in Cylinders. Phosphocreatine in Rabbit Leg Muscle. *Journal of Magnetic Resonance Series B*, 103(3):255–260.
- [351] Veraart, J., Fieremans, E., and Novikov, D. S. (2019). On the scaling behavior of water diffusion in human brain white matter. *NeuroImage*.
- [352] Veraart, J., Novikov, D. S., Christiaens, D., Ades-Aron, B., Sijbers, J., and Fieremans, E. (2016). Denoising of diffusion MRI using random matrix theory. *NeuroImage*.
- [353] Veraart, J., Novikov, D. S., and Fieremans, E. (2018). TE dependent Diffusion Imaging (TEdDI) distinguishes between compartmental T2 relaxation times. *NeuroImage*.
- [354] von Smoluchowski, M. (1906). Zur kinetischen theorie der brownischen molekularbewegung und der suspensionen. *Annalen der Physik*, 326(14):756–780.
- [355] von Smoluchowski, M. (1916). Drei vortrage uber diffusion, brownische bewegung und koagulation von kolloidteilchen. *Zeitschrift fur Physik*, 17:55–58.



- [356] Wakana, S., Caprihan, A., Panzenboeck, M. M., Fallon, J. H., Perry, M., Gollub, R. L., Hua, K., Zhang, J., Jiang, H., Dubey, P., Blitz, A., van Zijl, P., and Mori, S. (2007). Reproducibility of quantitative tractography methods applied to cerebral white matter. *NeuroImage*.
- [357] Wandell, B. A., Dumoulin, S. O., and Brewer, A. A. (2007). Visual field maps in human cortex.
- [358] Wang, H., Lenglet, C., and Akkin, T. (2015). Structure tensor analysis of serial optical coherence scanner images for mapping fiber orientations and tractography in the brain. *Journal of Biomedical Optics*.
- [359] Wassermann, D., Makris, N., Rathi, Y., Shenton, M., Kikinis, R., Kubicki, M., and Westin, C. F. (2016). The white matter query language: a novel approach for describing human white matter anatomy. *Brain Structure and Function*.
- [360] Wedeen, V. J., Wang, R. P., Schmahmann, J. D., Benner, T., Tseng, W. Y., Dai, G., Pandya, D. N., Hagmann, P., D'Arceuil, H., and de Crespigny, A. J. (2008). Diffusion spectrum magnetic resonance imaging (DSI) tractography of crossing fibers. *NeuroImage*.
- [361] Weeden, V., Reese, T., Tuch, D., Wiegell, M., Dou, J.-G., Weisskoff, R. M., and D., D. C. (1999). Mapping fiber orientation spectra in cerebral white matter with fourier-transform diffusion mri. In *Proc. ISMRM*.
- [362] Weinstein, D., Kindlmann, G., and Lundberg, E. (1999). Tensorlines: advection-diffusion based propagation through diffusion tensor fields. pages 249–253.
- [363] Westin, C. F., Maier, S. E., Khidhir, B., Everett, P., Jolesz, F. A., and Kikinis, R. (1999). Image Processing for Diffusion Tensor Magnetic Resonance Imaging. pages 441–452.
- [364] Whittall, K. P., MacKay, A. L., Graeb, D. A., Nugent, R. A., Li, D. K. B., and Paty, D. W. (1997). In vivo measurement of T2 distributions and water contents in normal human brain. *Magnetic Resonance in Medicine*.
- [365] Yamada, K., Sakai, K., Akazawa, K., Yuen, S., and Nishimura, T. (2009). MR tractography: a review of its clinical applications. *Magnetic resonance in medical sciences : MRMS : an official journal of Japan Society of Magnetic Resonance in Medicine*.
- [366] Ye, C. (2017). Tissue microstructure estimation using a deep network inspired by a dictionary-based framework. *Medical Image Analysis*.
- [367] Yoldemir, B., Acar, B., and Firat, Z. (2012). Smt: A reliability based interactive dti tractography algorithm. *IEEE Transactions on Medical Imaging IEEE Trans. Med. Imaging*, 31(10):1929–1940.
- [368] Yuste, R. and Church, G. (2014). The New Century of the Brain. *Scientific American*, 310(3):38–45.

## Bibliography

---

- [369] Zhang, H., Dyrby, T., and Alexander, D. (2011a). Axon Diameter Mapping in Crossing Fibers with Diffusion MRI. In *Lecture Notes in Computer Science*, pages 82–89. Springer Berlin Heidelberg.
- [370] Zhang, H., Hubbard, P. L., Parker, G. J., and Alexander, D. C. (2011b). Axon diameter mapping in the presence of orientation dispersion with diffusion MRI. *NeuroImage*.
- [371] Zhang, H., Schneider, T., Wheeler-Kingshott, C. A., and Alexander, D. C. (2012). NODDI: Practical in vivo neurite orientation dispersion and density imaging of the human brain. *NeuroImage*.
- [372] Zhang, J., Ji, H., Kang, N., and Cao, N. (2005). Fiber tractography in diffusion tensor magnetic resonance imaging: A survey and beyond. ... *Symposium on Medical Imaging* ...
- [373] Zhang, Y., Brady, M., and Smith, S. (2001). Segmentation of brain MR images through a hidden Markov random field model and the expectation-maximization algorithm. *IEEE Transactions on Medical Imaging*.
- [374] Zikopoulos, B. and Barbas, H. (2013). Altered neural connectivity in excitatory and inhibitory cortical circuits in autism. *Frontiers in Human Neuroscience*.
- [375] Zilles, K. and Amunts, K. (2010). Centenary of Brodmann's map conception and fate.

# Muhamed BARAKOVIC

## PERSONAL DATA

---

PLACE AND DATE OF BIRTH  Dobož, Bosnia and Herzegovina | 16 July 1990  
CITIZENSHIP  italian, bosnian  
ADDRESS  chemin de Veilloud 10, Ecublens, 1024,  
Lausanne, Switzerland  
PHONE  +41 79 890 84 81  
E-MAIL  [muhamed.barakovic@epfl.ch](mailto:muhamed.barakovic@epfl.ch)  
LINKEDIN  barakovicm

## EDUCATION

---

SEPTEMBER 2015 Ph.D. student in ELECTRICAL ENGINEERING  
SEPTEMBER 2019 **École polytechnique fédérale de Lausanne**,  
Lausanne, Switzerland  
Signal Processing Lab LTS5  
Topic : "Convex Optimization Modeling for Micro-structure Informed  
Tractography"  
Advisor: Prof. Jean-Philippe THIRAN, Dr. Alessandro DADUCCI

SEPTEMBER 2012 Master of Science in BIOINFORMATICS and MEDICAL BIOTECHNOLOGY  
OCTOBER 2014 **University of Verona**, Verona, Italy  
Thesis: "Cervix cancer spatial modelling for brachytherapy applicator  
analysis"  
Advisor: Prof. Andrea GIACHETTI  
Final Grade: 110/110 *summa cum laude*

SEPTEMBER 2009 Undergraduate Degree in BIOINFORMATICS  
JULY 2012 **University of Verona**, Verona, Italy  
Thesis: "Structural analysis of receptors coupled to G proteins"  
Advisor: Dr. Alejandro GIORGETTI  
Final Grade: 103/110

## EXPERIENCE

---

JULY 2018 visiting Ph.D. student in the DEPARTMENT OF RADIOLOGY  
SEPTEMBER 2018 **Stanford University**, Stanford, USA  
Richard M. Lucas Center for Imaging  
Topic : "Using CLARITY 3D Histology to Improve  
Microstructure Informed Diffusion MRI Tractography"  
Advisor: Prof. Jennifer McNAB

MARCH 2017 visiting Ph.D. student in the DEPARTMENT OF PSYCHOLOGY  
SEPTEMBER 2017 **Cardiff University's Brain Research Imaging Centre**, Cardiff, Wales  
Topic : "Towards in-vivo estimation of axon diameter mapping at 300mT/m"  
Advisor: Prof. Derek JONES

JANUARY 2014 visiting Student in DEPARTMENT OF INFORMATION SCIENCES AND TECHNOLOGIES  
JUNE 2014 **University of Primorska**, Koper, Slovenia  
Topic: "Cervix cancer structural analysis on MR images"  
Advisor: Prof. Peter ROGELJ

## ORGANIZATION SKILLS

---

Chief organizer of ISMRM 2018 Symposium "Non-invasive axon diameter mapping" (300+ attendees)  
Chief organizer of "Axon diameter mapping workshop 2018". (100 attendees)  
Organizer of several exchange days between labs in Diffusion MRI domain.

## PROGRAMMING SKILLS

---

Operating systems and main software packages: Macintosh, Linux, Windows, LaTeX  
Programming languages and software development tools:  
Good Knowledge: Python, C, C++, MATLAB, Java, Cuda, Javascript, JQuery, PostgreSQL, mysql, XML, HTML, JSP, Google API

## LANGUAGES

---

BOSNIAN: Mothertongue  
ITALIAN: Mothertongue  
ENGLISH: Fluent  
GERMAN: Basic Knowledge  
FRENCH: Basic Knowledge

## SCHOLARSHIPS AND CERTIFICATES

---

FEB. 2018 Firmenich EPFL-Stanford exchange program (CHF 11000)  
FEB. 2017 Swiss National Science Fundation Mobility grant for a period at Cardiff University (CHF 8000)  
FEB. 2013 Scholarship from Erasmus Program (EUR 1750)  
SEPT. 2009 Scholarship for graduate students with an outstanding curriculum (€400)  
JUN. 2009 Certification of Volkswagen Group Italia as car technician (3 years)  
Final Grade: 10/10  
JUN. 2009 Certification of Italian Rail Network as railway technology and operating elements (3 years)  
Final Grade: 83/110

## RESEARCH ACTIVITY

---

- **Convex Optimization Modeling for Micro-structure Informed Tractography**  
The project is focus on a novel linear formulation that combine tractography and tissue micro-structure estimation; the Convex Optimization Modeling for Micro-structure Informed Tractography framework. The introduction of convex optimization as a way to express tractography and tissue micro-structure has opened the door for quantitative and biologically-oriented connectivity analyses to become practical. The goal of the project is to develop the unifying framework to access more informative micro-structural properties of the fascicles. The applicability of this methodology will be tested for use on standard clinical systems and pathological conditions.  
Advisor: Prof. Jean-Philippe THIRAN, Prof. Alessandro DADUCCI, Prof. Derek JONES, Prof. Giorgio INNOCENTI.
- **Learning global brain microstructure using trainable sparse encoders**  
Diffusion Weighted-MRI is a non-invasive technique used to infer the brain's tissue microstructure. In this study, we used a global tractography informed microstructure framework named COMMIT to compute the axon diameter indexes in human brain

data. Thereupon, we used a neuronal network to learn the sparse encode representation of the data and performed an end-to-end reconstruction of the aforementioned axon diameter indexes directly from the DW-MRI data. Our results show the feasibility of this approach to learn the dictionary basis as well as the microstructure indexes. Advisors: Prof. Jean-Philippe THIRAN.

- **Comparing fiber orientation estimates from CLARITY and Diffusion MRI in macaque**  
In this work we cleared slabs of monkey visual cortex using CLARITY, a novel technique capable to highlight neurofilaments while keeping intact the neural structure using an hydrogel. Furthermore, the only non-invasive technique able to recover fiber orientation, diffusion MRI, was used to acquire images on the same samples. We compared the estimated fiber orientations between the two techniques.  
Advisor: Prof. Jennifer McNAB.

## INTERESTS AND ACTIVITIES

---

Medical Imaging, Quantitative MRI  
Mixed Reality, Artificial intelligence, Machine Learning  
Computational biology, Bioinformatics, Data Science  
Technology, Programming, Databases  
Neuroscience, Genomics, Human genome  
Psychology, Human interaction, Leadership, Team Working

## REFERENCES

---

- Prof. Jean-Philippe Thiran, Associate Professor. School of Electrical Engineering, Ecole Polytechnique Fédérale de Lausanne (EPFL)  
address: EPFL-STI-IEL-LTS5 Station 11; CH-1015 Lausanne, Switzerland. | email: jean-philippe.thiran@epfl.ch
- Prof. Alessandro Daducci, Assistant Professor. Department of Computer Science, University of Verona  
address: University of Verona, Department of Computer Science. Strada le Grazie, 15; I-37134 Verona, Italy. | email: alessandro.daducci@univr.it
- Prof. Derek Jones, Director. Cardiff University's Brain Research Imaging Centre, School of Psychology  
address: Cardiff University, Cardiff, CF10 3AT, Wales | email: jonesd27@cardiff.ac.uk
- Prof. Jennifer McNab, Assistant Professor. Stanford University, Department of Radiology  
address: Richard M. Lucas Center for Imaging, 1201 Welch Road, Stanford, California 94305, USA | email: mcnabj@stanford.edu
- Prof. Giorgio Innocenti, Professor. Karolinska Institutet, Department of Neuroscience  
address: EPFL-STI-IEL-LTS5 Station 11; CH-1015 Lausanne, Switzerland. | email: giorgio.innocenti@ki.se